Band gaps by design:
Tailoring ZnO based semiconductor alloy films

A Dissertation

Presented in Partial Fulfillment of the

Requirements for the

Degree of Doctor of Philosophy

with a

Major in Physics

in the

College of Graduate Studies

University of Idaho

by

Hui Che

April 2014

Major Professor: Leah Bergman, Ph.D.

Authorization to Submit Dissertation

This thesis of Hui Che, submitted for the degree of Doctor of Philosophy with a Major in Physics and titled "Band gaps by design: Tailoring ZnO based semiconductor alloy films" has been reviewed in final form. Permission, as indicated by the signatures and dates below, is now granted to submit final copies to the College of Graduate Studies for approval.

Major Professor _____ Date: _____
Leah Bergman

Committee Members _____ Date: _____
Matthew D. McCluskey

_____ Date: _____
Thomas Williams

_____ Date: _____
Ruprecht Machleidt

Department Administrator _____ Date: _____
David McIlroy

Discipline's College Dean _____ Date: _____
Paul Joyce

Final Approval and Acceptance

Dean of the College of Graduate Studies _____ Date: _____
Jie Chen

Abstract

This dissertation presents the research on the synthesis of ZnO based ternary semiconductor alloy films with tailored band gaps and the studies in their structural and optical properties. $Mg_xZn_{1-x}O$ alloys expanded the band gaps from 3.20 eV to deeper UV region of 5.67 eV. While ZnS_xO_{1-x} reduced the band gaps into the visible region of 2.9 eV. The alloy films were grown via reactive sputtering deposition, which is a cost effective and environment-friendly technique. An analytical method was developed for accurately determining the band gaps of alloys via transmission spectroscopy. The structural inhomogeneity issues in the $Mg_xZn_{1-x}O$ alloys were studied via Selective Resonant Raman Scattering. Urbach energy analysis and Raman spectral line width analysis indicated that structural defects and alloy compositional fluctuations in the $Mg_xZn_{1-x}O$ alloy films are the dominant origins of the localized electronic tail states and the Raman line broadening. While the Raman line broadening due to the anharmonicity of the alloys is not significant. The achievement of ZnS_xO_{1-x} alloy films with reduced band gaps paved the way for further research on band gap engineering of ZnO in the visible region.

Acknowledgment

I would like to express the deepest appreciation to my advisor Dr. Leah Bergman for giving me the opportunity to conduct research work on optical materials. She has been a tremendous mentor for me throughout my graduate studies. Her patient guidance and constant encouragement enabled me to grow as a research scientist and helped me to recover when my steps faltered.

I am grateful to my committee members Dr. Thomas Williams, Dr. Matthew McCluskey, and Dr. Ruprecht Machleidt for their insight and suggestions during my research work, and for their valuable comment on this dissertation.

My heartfelt appreciation also goes to my colleagues Dr. Jesse Huso, Dr. John Morrison, and Dinesh Thapa. It has been a great pleasure working with all of you. Thank you for introducing me to the wonders and frustrations of scientific research. Your passion and professionalism have always inspired me. I have learned a lot from each of you. Those geeky humor in and out of the lab were highly appreciated, as well.

Thanks also goes to Mr. John Failla for his continuous help with equipment design and manufacturing. Without his mastery of craft this research work would not have been possible.

All of my friends in Moscow and back in China also deserve recognition for all their help and support.

A special thanks goes to Ruisong, thank you for coming into my life.

Last but not least, thanks my parents Huiqun and Guanghong for their unflagging support. Without whom I would never have enjoyed so many opportunities in my life.

To my parents Huiqun Zhu and Guanghong Che,
for their endless love and belief.

Table of Contents

List of Figures

List of Tables

Chapter 1 Introduction: Band gap engineering in ZnO based semiconductor alloys

This dissertation presents the research work on the synthesis of zinc oxide (ZnO) based ternary semiconductor alloy thin films and the studies of their structural and optical properties. In this first chapter the following aspects will be discussed:

- The motivation to study ZnO based semiconductor alloys.
- An overview of the lattice matched MgO-ZnO alloy system and the lattice mismatched ZnS-ZnO alloy system studied in this work.

1.1 Zinc Oxide (ZnO): an environmentally friendly candidate for UV applications

Zinc oxide (ZnO) is a semiconductor material with a wide band gap of approximately 3.2 electron volts (eV). With a deep excitonic level around 60 meV, ZnO makes efficient exciton recombination based lasing action possible even above room temperature[1]. The band gap energy of ZnO falls in the range of ultraviolet (UV) and it makes ZnO a candidate for novel optical sources active in that range.

UV light is electromagnetic radiation with a wavelength in the range between 400 nm and 100 nm, corresponding to photon energies from 3.1 eV to 12.4 eV. Although such an energy range is out of the lower limit that humans can identify, UV light has a wide application in various fields such as sun tanning, fire detection, UV imaging in astronomy[2], optical storage in computing[3,4], bodily fluids identification in forensics[5], and air purification[6]. The advantages of UV applications call for efficient, safe and cost-effective UV sources. Conventional UV sources and detectors nowadays are either utilizing bulky, fragile mercury vapor filled glass tubes, or take a lower frequency light emitting diode and double or

quadruple the frequency to get UV emission. Such an approach is intrinsically less efficient than a source that directly emits UV light. Furthermore, the frequency doubling crystals are very vulnerable in an uncontrolled environment and thus its use is severely limited. Therefore the search for solid state materials with direct UV emitting or absorption abilities has become a popular research area.

ZnO, as a promising candidate for UV applications, has its advantages. It is an environment-friendly material, commonly found as the mineral zincite, and has been widely used in medicine, paint, protective coatings, and even foods. The production of ZnO is cost-effective both in industry and in laboratory. A level of 10^5 tons of ZnO is produced per year for industrial use[7]. ZnO in different crystal forms including bulk single crystals, polycrystalline thin films and nanostructures, etc. can be synthesized via various specialized methods for scientific studies.

1.2 Band gap engineering

1.2.1 The objective and approaches of band gap engineering

Various applications call for devices that are sensitive to, or operate at, different energies, which requires semiconductor materials with a much larger selection of band gap energies than the few that nature has provided. Therefore it is essential to create materials with designed band gap energies in order to achieve desired light absorption or emission for particular applications.

One of the practical approaches of engineering the band gap of a certain material is utilizing the quantum confinement effect. When a material's dimension decreases and reaches the order of the wavelength of the electron wave function, their electronic and optical properties deviate substantially from those of bulk materials. In terms of quantum mechanics,

the edges of the material act like potential barriers and a particle of mass *m* and dimension *L* can be approximated as a "particle in the box" model in a three-dimensional frame. Then its energy levels corresponding to each of the permitted wavenumbers are[8]

$$E_{n_x,n_y,n_z}=\frac{h^2}{8m}\left[\left(\frac{n_x}{L_x}\right)^2+\left(\frac{n_y}{L_y}\right)^2+\left(\frac{n_z}{L_z}\right)^2\right] \qquad (n_x, n_y, \text{or } n_z=1,2,3,...) \qquad (1.1)$$

where *h* is the Planck constant. As the particle's dimension *L* decreases, the energy difference between states increases and thus the energy gap between the conduction states and the valence states is raised.

Current development in quantum dots, which confine a particle in three dimensions, has shown great potential for bio-sensing and bio-imaging[9,10], high efficiency solar cells[11], and revolutionary light emitting displays[12]. However, this technique has some practical limitations. First of all, in order to achieve band gap engineering, the size of quantum dots should be as small as a few nanometers. Such a small size leads to difficulties in utilizing these quantum dots for devices. Furthermore, quantum confinement can only **increase** the band gap of a material. When there is a need of band gap reduction, this technique becomes inapplicable.

Another approach of band gap engineering is alloying, which is the creation of a hybrid material from two or more pure materials via solid solutions. By substituting some of the sites in the crystal lattice of certain material with atoms of different kinds, the properties of the material will be altered and thus the band gap could be tuned. The details of this technique will be discussed in the following sections with examples of ZnO based alloys.

1.2.2 Band gap Engineering in ZnO via alloying

The electronic energy band structure of ZnO can be modified by the substitution of isoelectronic anions or cations. It has been demonstrated by the achievement of the band gap increasing in $Mg_xZn_{1-x}O$[13,14], $Be_xZn_{1-x}O$[15], and, $Ca_xZn_{1-x}O$[16] alloys and the band gap reduction in $Cd_xZn_{1-x}O$[17,18] and ZnS_xO_{1-x}[19,20] alloys.

The band gap energy $E_g(x)$ of a ternary semiconductor $A_xZn_{1-x}O$ alloy (where A could be Mg, Be, or S, etc.) is determined by the band gap energies of both the binary end members, E_{ZnO} and $E_{AO\ (or\ ZnA)}$, as the following equation:[21]

$$E_g(x) = (1-x)E_{ZnO} + xE_{AO(\text{or } ZnA)} - bx(1-x) \tag{1.2}$$

In this equation the constant b is known as the bowing parameter which depends on the mismatch in electronegativities and atomic sizes between the substituting atomic species[22,23]. The bowing parameter b describes the deviation from a linear behavior of the alloy's band gap with respect to the alloy composition. Figure 1.1 illustrates how ideally the band gap of an alloy behaves as a function of the alloy composition for different bowing parameters. When $b=0$, the band gap of the alloy changes linearly with respect to the relative composition of the two binary compounds. For $b>0$, the behavior of the resultant band gap exhibits a bowing effect which makes it possible to create an alloy with a band gap lower than that of either the binary end members.

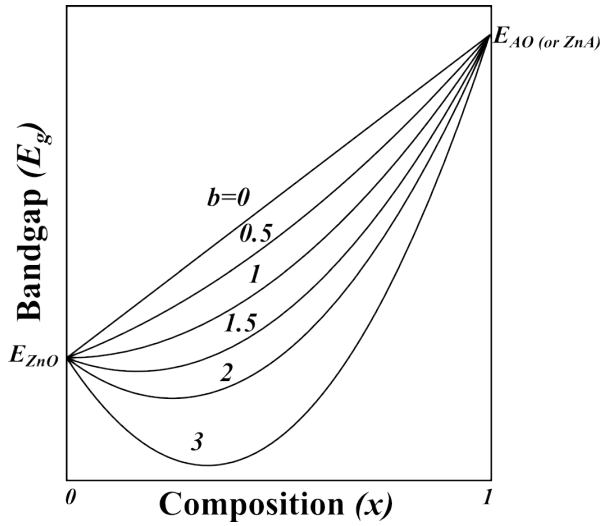

Figure 1.1 ： The band gap (E_g) of an ideal $A_xZn_{1-x}O$ alloy (A could be Mg, Be, or S, etc.), as a function of composition (x) for different values of bowing parameter b. For large values of b, the bandgap of the alloy can be lower than that of either of the end members.

1.3 Focus of this work: $Mg_xZn_{1-x}O$ and ZnS_xO_{1-x} alloys

In this work, two types of ZnO based ternary alloy were investigated: $Mg_xZn_{1-x}O$ and ZnS_xO_{1-x}. They will be discussed in sequence.

ZnO naturally occurs in a wurtzite hexagonal structure with a band gap of approximately 3.2 eV while MgO has a rocksalt cubic structure with a band gap of approximately 7.8 eV. The different lattice structures of ZnO and MgO are illustrated in Figure 1.2 (a) and (b). By alloying these two end members into a solid solution of $Mg_xZn_{1-x}O$, Mg atoms substitute some of the Zn sites in the ZnO lattice as shown in Figure 1.2 (c). The bowing parameter *b* of the $Mg_xZn_{1-x}O$ system is small and thus an increase in the band gap can be achieved[24,25].

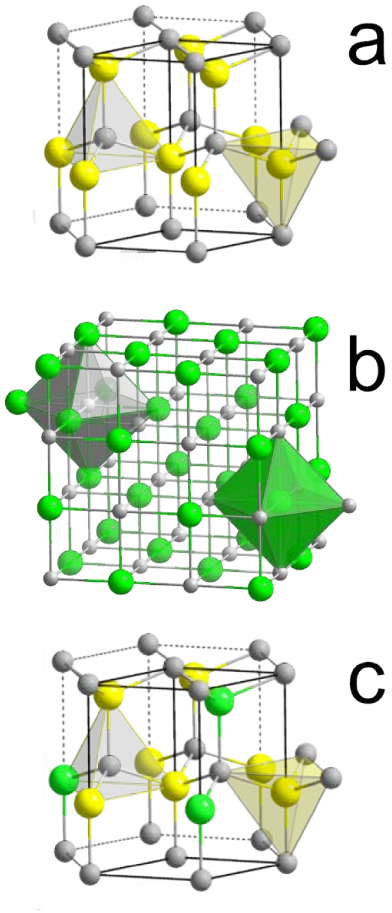

Figure 1.2 : a) The wurtzite hexagonal crystal structure of ZnO and b) the rock salt cubic structure of MgO. c) By alloying these materials a solid solution of $Mg_xZn_{1-x}O$ is created, where some Zn atoms (yellow) have been replaced by Mg atoms (green).

The difference in crystal structures between ZnO and MgO will affect the structure of $Mg_xZn_{1-x}O$. With low Mg contents, the alloy retains the hexagonal wurtzite structure of the ZnO. When the Mg content exceeds a certain threshold, the alloy turns to the cubic structure of MgO. In between the two scenarios there is a mixed phase region where coexist both the wurtzite and the cubic structures and numerous effects can occur. The achievement of band gap engineered $Mg_xZn_{1-x}O$ films and the studies of their alloy inhomogeneities will be

discussed in detail later in Chapter 4.

Aside from substituting the cations of ZnO to create a system like $Mg_xZn_{1-x}O$, anion substitution of ZnO could also be accomplished. Zinc sulfide (ZnS) is also a chemically benign material which is mainly found in nature as the mineral sphalerite with a zinc blende cubic structure[26] as illustrated in Figure 1.3. Its band gap is approximately 3.54 eV. When alloying ZnS with ZnO, the large mismatch in the electronegativity and in the size between O and S atoms result in a significant band gap bowing effect in the ZnS_xO_{1-x} system. Therefore it is possible to achieve a band gap reduction with a low S composition[27].

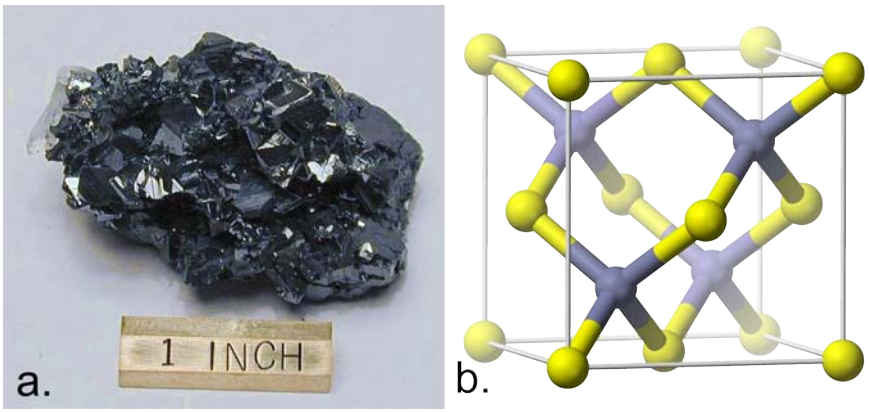

*Figure 1.3 : **a)** ZnS as the mineral sphalerite. Photo courtesy of Alan Guisewite. And **b)** its zinc blende cubic crystal structure.*

In summary, the focus of this work is to achieve band gap engineering of ZnO in a wide range via alloying. As can be seen in Figure 1.4, a continuously tunable band gap was achieved from the deep UV region via $Mg_xZn_{1-x}O$ alloy films, and, down into the visible region via ZnS_xO_{1-x} alloy films. Optical studies were carried out to understand the structural inhomogeneities in the $Mg_xZn_{1-x}O$ system and their effect on materials properties. The success in synthesizing ZnS_xO_{1-x} alloy films with expected band gap reduction paved the road

for future research toward the realization of viable devices functional in the visible region.

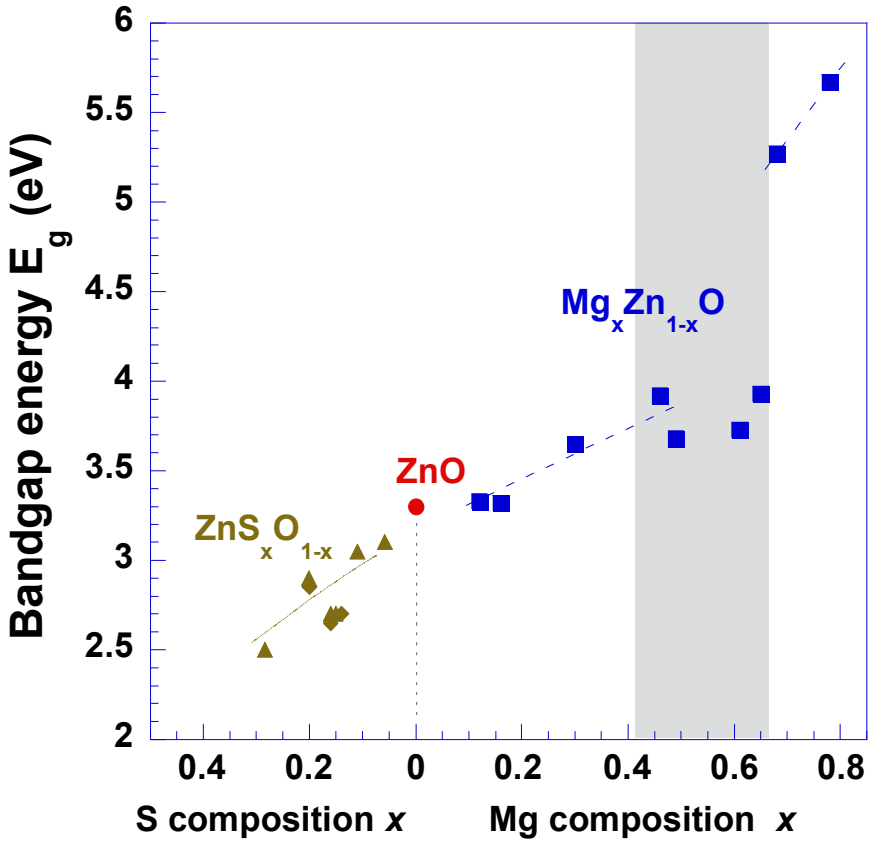

Figure 1.4: Via alloying with MgO and ZnS, band gap engineering of ZnO can achieve a wide range from UV well into visible. Data presented are the experimental results of the ZnO based alloy films grown via sputtering for this work. Squares represent the band gap energy of $Mg_xZn_{1-x}O$ films grown on quartz and calcium fluoride substrates; triangles and diamonds represent that of ZnS_xO_{1-x} films grown on quartz and flexible Fluorinated Ethylene Propylene (FEP) substrates, respectively; circles represent that of pure ZnO film grown on quartz substrate for comparison. The shadowed area indicates the phase segregation region which will be discussed in Chapter 4.

1.4 Conclusion

Light emission and absorption solid state materials with operational energies from the UV to visible range have potential applications in numerous areas from air purification to solar cells. Via alloying ZnO with MgO and ZnS, respectively, $Mg_xZn_{1-x}O$ and ZnS_xO_{1-x} alloys can be created with tunable band gap energies within a wide UV-visible range. Detailed experimental procedures and results including material synthesis and characterization will be discussed in later chapters.

1.5 References

1. Morkoç, H. & Özgür, Ü. *Zinc oxide: fundamentals, materials and device technology.* (Wiley-VCH, 2009).

2. Cox, A. N. *Allen's Astrophysical Quantities*. (Springer, 2000).

3. Breakthrough Nanotechnology Will Bring 100 Terabyte 3.5-inch Digital Data Storage Disks. at <http://phys.org/news785.html>

4. Ultraviolet light to squeeze in the data - physicsworld.com. at <http://physicsworld.com/cws/article/news/2001/jun/07/ultraviolet-light-to-squeeze-in-the-data>

5. Springer, E. *et al.* Detection of dry body fluids by inherent short wavelength UV luminescence: preliminary results. *Forensic Sci. Int.* **66,** 89–94 (1994).

6. Scott, K. J. & Wills, R. B. Atmospheric pollutants destroyed in an ultra violet scrubber. *Lab. Pract.* **22,** 103–106 (1973).

7. Klingshirn, C. ZnO: Material, Physics and Applications. *ChemPhysChem* **8,** 782–803 (2007).

8. Davies, J. H. *The Physics of Low-dimensional Semiconductors: An Introduction*. (Cambridge University Press, 1998).

9. Li, J. & Zhu, J.-J. Quantum dots for fluorescent biosensing and bio-imaging applications. *Analyst* **138,** 2506–2515 (2013).

10. Pathak, S., Cao, E., Davidson, M. C., Jin, S. & Silva, G. A. Quantum Dot Applications to Neuroscience: New Tools for Probing Neurons and Glia. *J. Neurosci.* **26,** 1893–1895 (2006).

11. H. Sargent, E. Infrared Quantum Dots. *Adv. Mater.* **17,** 515–522 (2005).

12. Sun, Q. *et al.* Bright, multicoloured light-emitting diodes based on quantum dots. *Nat. Photonics* **1,** 717–722 (2007).

13. Morrison, J. L. *et al.* Optical properties of ZnO and MgZnO nanocrystals below and at the phase separation range. *J. Appl. Phys.* **104,** 123519 (2008).

14. Ohtomo, A. *et al.* $Mg_xZn_{1-x}O$ as a II–VI widegap semiconductor alloy. *Appl. Phys. Lett.* **72,** 2466–2468 (1998).

15. Ryu, Y. R. *et al.* Wide-band gap oxide alloy: BeZnO. *Appl. Phys. Lett.* **88,** 052103 (2006).

16. Joseph, D. P. & Venkateswaran, C. Bandgap Engineering in ZnO By Doping with 3d Transition Metal Ions. *J. At. Mol. Phys.* **2011,** (2011).

17. Ishihara, J., Nakamura, A., Shigemori, S., Aoki, T. & Temmyo, J. $Zn_{1-x}Cd_xO$ systems with visible band gaps. *Appl. Phys. Lett.* **89,** 091914 (2006).

18. Ma, D. W., Ye, Z. Z. & Chen, L. L. Dependence of structural and optical properties of $Zn_{1-x}Cd_xO$ films on the Cd composition. *Phys. Status Solidi A* **201,** 2929–2933 (2004).

19. Locmelis, S. *et al.* Optical band gap in the system $ZnO_{1-x}S_x$. An experimental and quantum chemical study. *J. Mater. Sci.* **42,** 1965–1971 (2007).

20. Che, H. *et al.* Optical Properties of ZnO-Alloyed Nanocrystalline Films. *J. Nanomater.* **2012,** (2012).

21. Van Vechten, J. A. & Bergstresser, T. K. Electronic Structures of Semiconductor Alloys. *Phys. Rev. B* **1,** 3351–3358 (1970).

22. Ferhat, M. Computational optical band gap bowing of III–V semiconductors alloys. *Phys. Status Solidi B* **241,** R38–R41 (2004).

23. Tit, N., Obaidat, I. M. & Alawadhi, H. Origins of bandgap bowing in compound-semiconductor common-cation ternary alloys. *J. Phys. Condens. Matter* **21,** 075802 (2009).

24. Zeuner, A. *et al.* Structural and optical properties of epitaxial and bulk ZnO. *Appl. Phys. Lett.* **80,** 2078–2080 (2002).

25. Roessler, D. M. & Walker, W. C. Spin-Orbit Splitting of the Γ Exciton in MgO. *Phys. Rev. Lett.* **17,** 319–320 (1966).

26. Wells, A. F. *Structural inorganic chemistry*. (Clarendon Press, 1965).

27. Moon, C.-Y., Wei, S.-H., Zhu, Y. Z. & Chen, G. D. Band-gap bowing coefficients in large size-mismatched II-VI alloys: first-principles calculations. *Phys. Rev. B* **74,** 233202 (2006).

Chapter 2 Methodology: Synthesis of ZnO based alloy films and material characterization techniques

In this work, $Mg_xZn_{1-x}O$ and ZnS_xO_{1-x} alloy films were synthesized via reactive magnetron sputtering deposition. The structural and optical properties of the films were then investigated. This chapter is dedicated to introduce

- The working principle of sputtering deposition;
- Equipment used and constructed for film growth in this work;
- Fundamental knowledge on material characterization techniques utilized in this work, including scanning electron microscopy, X-ray microanalysis, optical transmission spectroscopy, and, Raman spectroscopy.

2.1 Introduction to sputtering

Cathodic sputtering is the phenomenon of a cathode electrode disintegration under the bombardment of ionized gas molecules as an electrical discharge passes between electrodes at a low gas pressure[1]. This phenomenon was first reported in 1852 by the English physicist W. R. Grove, who reported that during electrical discharging in gases the wall of a glow discharge tube became coated with a metal film deposit in the anode region[2]. Upon its discovery, sputtering was considered as an undesired phenomenon since the cathode material was destroyed during the process. However, after years of extensive basic physical investigations of this phenomenon in the last century, sputtering became an independent branch of thin film technology. At present sputtering is a widely used method for surface cleaning and etching, thin-film deposition, surface and surface layer analysis, and sputter ion sources[3]. Furthermore, due to the simplicity of the equipment, the ability to deposit a wide

range of materials and a high scalability, sputtering deposition technology has found its application in various operational areas include the optical coating of architectural glass and lenses[4]; the manufacturing of solar cells, photo-diodes and microchips[5–7]; and the surface protection of tools, machine parts and space crafts[8,9]. The terms sputtering, sputtered films, sputter PVD or sputter coating are usual synonyms for this technology.

2.1.1 Sputtering Mechanism

Different types of sputtering system are used in practice, including direct current (DC) diode, radio frequency (RF) diode, magnetron diode, and ion beam sputtering. DC diode sputtering is the most simple type among the ones listed above and will be used as a model to illustrate the fundamental mechanisms of sputtering deposition.

A DC sputtering system is composed of a pair of electrodes: one cathode and one anode, which are positioned opposite each other. The desired coating material is mounted in front of the cathode as a sputtering target. Substrates awaiting to be coated are placed on the anode. The sputtering system is then placed under vacuum and ready to be filled with a working gas. An inert gas, such as argon, is most often used as the working gas. However, in order to achieve the most efficient momentum transfer, in some cases neon or krypton is used as the working gas to match a lower or higher atomic mass of the target material. Upon the setup of the electrodes, an electric field is applied between them. With the presence of a few stray electrons, the applied electric field causes a cascade of ionization of the working gas and generates a plasma. The positively charged ions in the plasma are then accelerated by the electric field toward the cathode and eventually bombard the target material. A small portion of material is ejected from the target by the impact of the accelerated ions landing on it. The

ejected portions of material are usually electrically neutral thus they can travel across the applied electric field and the plasma region and finally deposit on the substrate. As this process continues, a uniform thin film is coated on the substrate. A schematic illustrating such a sputtering process is shown as Figure 2.1.

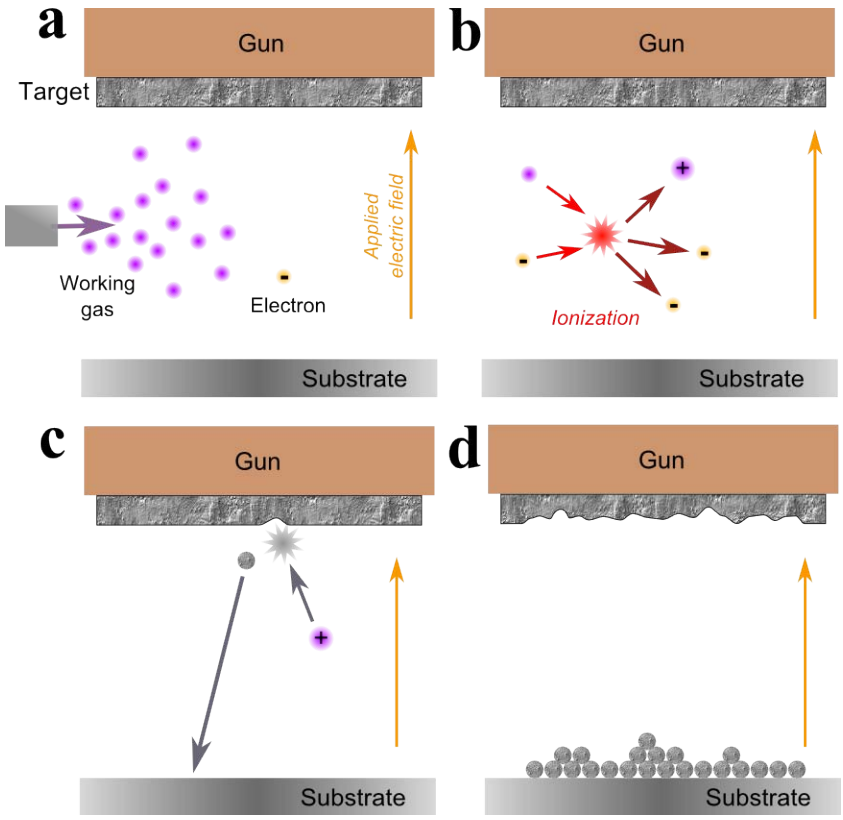

Figure 2.1: A schematic illustrating the process of DC sputtering. ***a)*** *Initially the chamber is filled with the working gas (purple) and stray electrons (orange) are accelerated by the applied electric field.* ***b)*** *The electron collides with a working gas atom, an ion (purple +) and more electrons were generated.* ***c)*** *The ion is accelerated toward the target and bombard the target, ejecting a small portion of the target. The ejected material travels and deposits on the substrate. d) The previous processes repeat and over time the substrate is coated with a thin layer of the target material.*

2.1.2 Direct current sputtering and radio frequency sputtering

For a conductive sputtering target, a direct current (DC) power source is the best choice since it maximizes the sputtering rate by continuously vaporizing the target material and coating the substrate. However, the formation of arcs is more common in DC sputtering. Once a DC power is applied, charges accumulate at surface defects of the sputtering target to a point of breakdown. As intense, localized concentrations of plasma supported by collective emission of electrons from the sputtering surface[10], arcs can cause severe damages to the sputtering target and the chamber due to the explosive ejection of macro-particles at arcing sites. Although modern DC supplies, including the one used in this work, have enabled fast detection and suppression to arcs, these events cannot be completely eliminated.

Another limitation of DC sputtering is its inapplicability to non-conductive sputtering targets. When sputtering with an insulating target, positive charges tend to build up on the target end (cathode) due to the inability of the target to dissipate the incoming charge. Over time it will come to a point where incoming ions are repelled away from the target and thus sputtering stops completely, as shown in Figure 2.2.

One of the most common and reliable approaches to maintain the discharge and to avoid charge build-up on the target is using a radio frequency (RF) generator as the power source. In RF sputtering, the polarity of the applied electric field is alternating at a high rate. During the first half cycle the positively charged ions are accelerated toward the target, bombarding the target and building up a positive charge on it. Then during the second half cycle the polarity of the field reverses. The negatively charged ions are guided toward the target and thus the positive charges accumulated earlier on the target now get neutralized. However, it should be noticed that during the second half cycle the sputtering is not occurring at the

target end but the substrate end. Therefore the RF arrangement solves the built-up charges issue at the expense of the sputtering rate. Additionally, in the configuration of RF sputtering the presence of a matching network between the RF power generator and the target is necessary in order to optimize the power dissipation in the discharge.

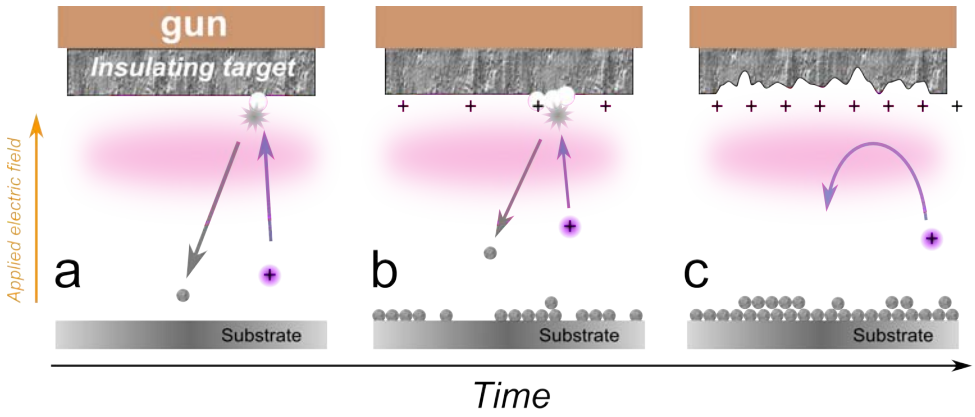

Figure 2.2: ***a)*** *A target made of insulating material is being sputtered.* ***b)*** *Positive charges build up on the surface of the target due to a lack of route for electrons to dissipate.* ***c)*** *Over time with enough positive charges accumulated, incoming ions are repelled away from the target and the sputtering stops completely.*

2.1.3 Magnetron Sputtering

In modern sputtering deposition system, a magnetron configuration is often applied to the sputtering gun in order to increase the sputtering rate by confining the secondary electrons, and therefore the plasma, closer to the cathode (target). In such a configuration, strong magnets are placed beneath the target material. On top of the applied electric field $\vec{E}$, a particle with a charge q moving in this magnetic field $\vec{B}$ experiences the Lorentz force

$$\vec{F} = q \cdot (\vec{E} + \vec{v} \times \vec{B}) \tag{2.1}$$

Where q is the charge and $\vec{v}$ is the velocity of the charged particle. Here the effect of Lorentz force leads to a circular motion with a rotational radius

$$r = \frac{m v}{q B} \tag{2.2}$$

Where m is the mass of the charged particle. For an electrons this radius is in the order of millimeters due to the small value of its mass, thus the movement of an electron is in a helical path around the magnetic field lines. While for the a positively charged ion of the working gas with larger mass, such radius is much larger than the system dimensions thus the ion is essentially unaffected by the magnetic field. Additionally, electrically neutral particles, such as those sputtered off from the target, also remains unaffected. As a result, the electrons are trapped in the vicinity of the magnetic field lines, highly increasing the probability of ionizing the atoms of the working gas in a localized area. While ions of the working gas keep bombarding the target and the sputtered material keep depositing on the substrate as usual.

Many different magnetron geometries can be constructed as long as the resultant path of electrons forms a closed loop so that the electrons are effectively constrained. The magnetron configuration utilized in this work is in a concentric ring pattern and Figure 2.3 (a) shows its cross sectional side view. Such a distribution of magnetic field confines the electrons in a donut shaped area near the surface of the target and thus in this area ions of the working gas are more likely to be created. As a result the sputtering rate is significantly increased. Figure 2.3 (b) is a photograph of a post-sputtering metal target. The discolored ring shape suggests a more severely sputtered area due to the applied magnetron configuration.

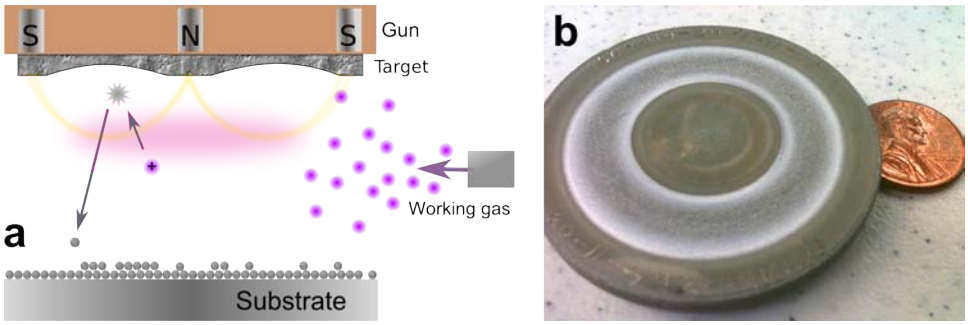

Figure 2.3: ***a)*** *The cross section side view of the magnetron configure utilized in this work.* ***b)*** *A sputtered metal target. The ring shaped pattern on the target suggests an area with enhanced sputtering rate by confining electrons within a certain region via a magnetic field.*

2.1.4 Reactive sputtering

Another common modification being applied to a sputtering process is reactive sputtering, where a target of one chemical composition is sputtered in the presence of a gas or a mixture of several types of gas that will react with the target material to form a different chemical compound. Reactive sputtering allows a higher deposition rate to be achieved with DC power, comparing to sputtering ceramic compound targets directly with a RF power. Commonly used reactive gases include oxygen, nitrogen, carbon dioxide, acetylene and methane. Reactive sputtering processes could provide significant cost and energy savings as well as production rate and quality advantages[1112].

2.1.5 The sputtering system used in this work

The thin films discussed in this work were synthesized using a custom built sputtering chamber as shown in Figure 2.4.

Figure 2.4: A photograph of the sputtering system utilized in this work. On the right is the growth chamber and underneath is the turbo molecular vacuum pump backed up by the mechanical roughing pump. On the left is the equipment rack with all the accompanying control electronics and power sources.

The chamber is evacuated using a Varian V200 turbo molecular pump backed by a Welch model 1402 DuoSeal belt drive mechanical roughing pump, and is sealed using a combination of Viton elastomer flanges and copper conflat style flanges. The pressure is measured using a Duniway convection gauge (measuring range: 1000-10^{-4} Torr), a capacitive gauge (measuring range: 100-10^{-4} Torr), and a Bayard-Alpart style hot cathode ion gauge (measuring range: 10^{-3}-10^{-10} Torr). This configuration allows the chamber to reach a base pressure of 2.6×10^{-6} Torr. During growth the chamber pressure is measured via the capacitive gauge since its readings are independent of gas composition thus a precise reading of chamber pressure can be achieved in spite of a mixture of two or more types of gas during reactive sputtering.

The chamber is equipped with two sputtering guns and is capable for dual target sputtering. However the materials studied in this work were grown using single target sputtering with a water cooled ST20 magnetron sputtering gun from AJA International, which takes 2-inch disk targets.

The working gas for sputtering in this work is argon (Ar) and the reactive gas is oxygen (O_2). The flow of individual gas entering the sputtering chamber is regulated by MKS Type P4B digital Mass Flow Controllers (MFCs) which are positioned upstream of the chamber, as shown in Figure 2.5. The flow measurement is based on differential heat transfer between temperature sensing heater elements attached to the exterior of the sensing tube. The thermal mass movement is sensed and then converted to mass flow via the specific heat and other thermodynamic properties of the gas. Advanced digital algorithms enables real-time control of gas flows with a high accuracy. The MFCs are configured individually for each gas line in order to optimize their performance. In this work the controlling of the gas flow rate can be

achieved with a resolution of 0.07 standard cubic centimeters per minute (sccm) and an accuracy of approximately ±1% of reading.

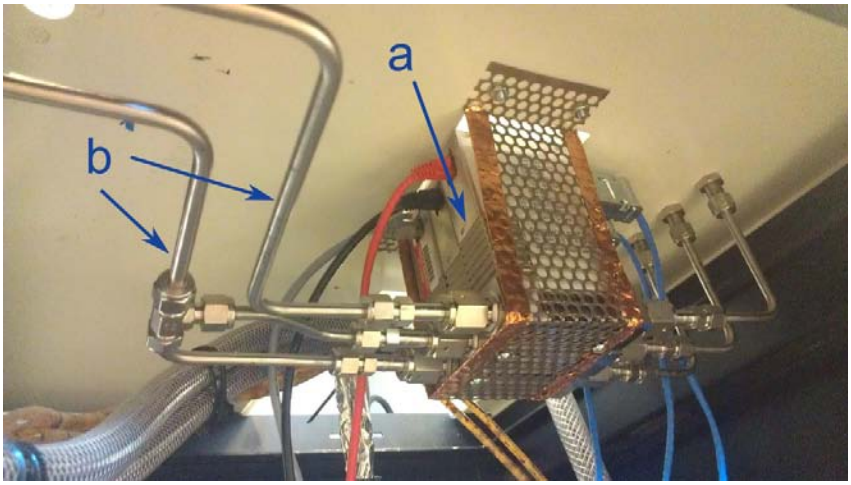

Figure 2.5: ***a)*** *A mass flow controller is installed in the gas line upstream of the sputtering chamber.* ***b)*** *The working gas (Ar) and the reactive gas (O_2) was introduced into the chamber in separated lines.*

Dalton's law states that the total pressure exerted by the mixture of non-reactive gases is equal to the sum of the partial pressure of individual gases. Accordingly, the total pressure in the sputtering chamber P_{total} during the sputtering process for this work can be described by the sum of the base pressure P_{base}, the partial pressure of Ar P_{Ar}, and, the partial pressure of O_2 P_{O_2}, as the following equation:

$$P_{total} = P_{base} + P_{Ar} + P_{O_2} \tag{2.3}$$

By introducing Ar gas and O_2 gas successively and monitoring the pressure in the chamber, the partial pressure of each type of gas can be recorded. Such technique allows a precise

control of the gas environment during sputtering and thus enhances the repeatability of material growth.

The targets used in this work were custom made Mg-Zn metal targets and a commercial ZnS (99.99%) ceramic target by American Elements. The Mg-Zn targets were made by mixing Mg and Zn metal powders in desired ratios and then pressing them in a 2 inch die using a Carver hydraulic press, at 50,000 lbs ram force for over 24 hours. The Mg and Zn metal powders were purchased from Alfa Aesar, of 99.8% and 99.9% purities respectively. The most significant advantage of pressed metal targets lies in the freedom of controlling the Mg-Zn ratio, as compared to the limited choices of commercially available ones. However, pressed metal targets cannot endure high input power due to its relatively lower density and higher probability of internal flaws[13].

Figure 2.6: The MDX 500 DC generator used in this work for the creation of ZnO and $Mg_xZn_{1-x}O$ thin films. It has a capability of delivering 500W of power to the sputtering target and has a built-in arc suppression circuitry.

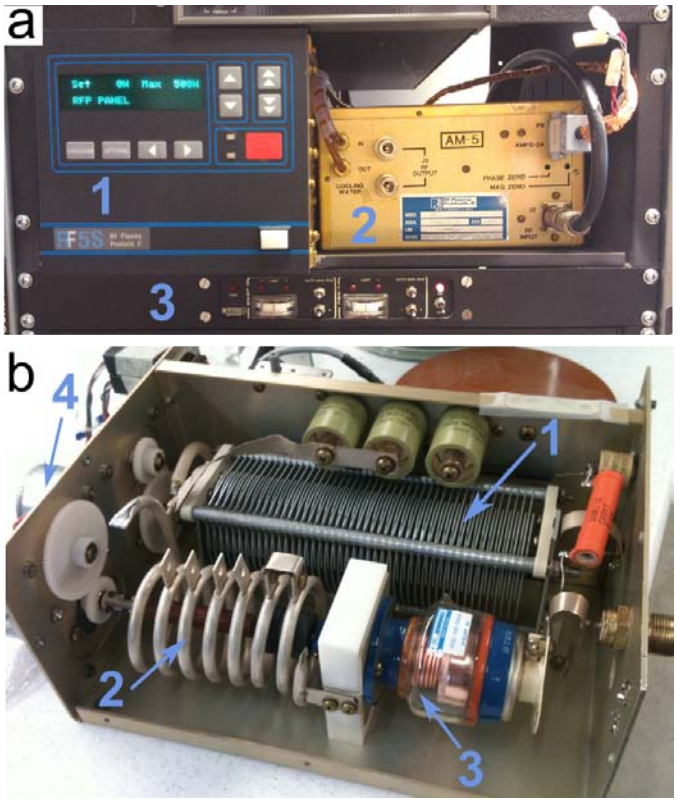

Figure 2.7: ***a)*** *The RF generator (1) used in this work, capable of delivering 500W at 13.56MHz, the RF matching network (2) and its controlling unit (3).* ***b)*** *The interior of the matching network shows the variable air capacitor (1), the inductor (2), the variable vacuum capacitor (3), and the stepper motors (4) which provide the mechanical adjustments.*

For the growth of $Mg_xZn_{1-x}O$ films, conductive Zn-Mg targets were sputtered and thus a DC power source was utilized. The DC source used in this work is an MDX 500 from Advanced Energy with a maximum power of 500W and a built in arc suppression circuitry, as shown in Figure 2.6. The ZnS_xO_{1-x} films, on the other hand, were grown via sputtering an insulating ZnS ceramic target and therefore a RF power source was necessary to guarantee continuous depositing. The RF source used here is a RF5S generator with an AM-2 matching network by RF Plasma Products Inc. (now a division of Advanced Energy) as shown in

Figure 2.7 (a). The RF generator has a capability of 500W output at a fixed frequency of 13.56MHz. When sputtering with a RF power source, a matching network is essential to minimize the power reflected back into the RF source and maximize the power delivered to the target. Figure 2.7 (b) shows the interior of the AM-2 matching network. Being composed by an inductor, a variable vacuum capacitor, and, a variable air capacitor, the matching network is capable to tune the output impedance in a wide range and consequently minimize the back reflecting power.

Figure 2.8: ***a)*** *The Watlow stainless steel strip heaters used for substrate heating and* ***b)*** *the custom built temperature controller based around a Yokogawa UT-150 PID controller. Such a system is capable for controlling the temperature of substrates tightly from room temperature to 780 °C.*

During the deposition of $Mg_xZn_{1-x}O$ films and ZnS_xO_{1-x} films in this work, the temperature of substrates was regulated by a custom substrate heating system which is

consisted by Watlow stainless steel strip heaters and a custom constructed temperature controller, as shown in Figure 2.8 (a) and (b), respectively. The temperature controller is based around a Yokogawa UT-150 PID controller. This heating system is capable of elevating the substrate temperature from room temperature up to 780 °C with a tight control, which allows for the growth of material with high crystalline qualities with a high repeatability of growth conditions.

An additional concern is the substrate protection during sputtering. As discussed in section 2.1.1, when sputtering is occurring energetic particles are bombarding not only the target but also the substrate. The considerable amount of kinetic energy delivered at the surface of the substrate could cause flaws in the deposited film and even damage the substrate. Thus magnetic shielding for substrate protection was adapted in this work[13]. Figure 2.9 shows geometry of the magnetic field created in this work for substrate protection. Similar to the effect of magnetron configuration as discussed in section2.1.3, this magnetic field captures charged particles, especially electrons. Thus a magnetic shield was created, preventing energetic particles from impacting the substrate, just like how Earth's magnetic shield protects us against the solar wind.

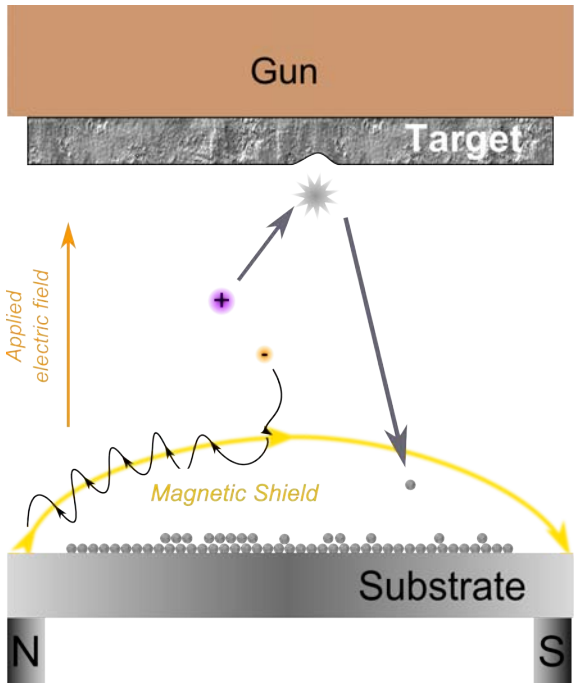

Figure 2.9: The magnetic shielding for substrate during sputtering. A magnetic field (yellow) is created directly beneath the substrate and the resulting field captures charged particles, particularly electrons, preventing them from impacting the substrate.

2.2 Material characterization methods: The electron microscope and X-Ray analysis

Upon achieving thin film materials via sputtering deposition, their structural and optical properties need to be characterized. In this work a Scanning Electron Microscope was utilized to form high resolution images of sample surfaces. The elemental analysis was performed by an Energy-Dispersive X-Ray Spectrometer in order to determine the relative compositions in ternary alloy systems. The crystalline quality and structure of the films were studied by the X-Ray diffraction.

2.2.1 Scanning Electron Microscopy

The scanning electron microscope (SEM) is a non-destructive surface analyzing technique with unique capabilities. It is analogous to a conventional optical microscope, but with a different source of radiation for illumination[14]. While an optical microscope forms images from visible light reflected from a sample's surface, an SEM uses a beam of electrons to scan across a specimen's surface in a television-like raster. These electrons interact with atoms in the specimen, going through inelastic scattering where they lose some of their energy and produce various signals such as secondary electrons, X-rays, and Auger electrons. Secondary electrons contain information about the specimen's surface morphology and the detection of them is the most common imaging mode. With an appropriate detector, emitted secondary electrons can be captured and analyzed, producing readily interpretable images of the specimen. Compared to visible light photons, electrons have much shorter wavelengths which are capable of conveying information with much higher resolution and thus higher magnification can be obtained without loss of details. The practical maximum resolution of an SEM can reach to 750,000×,[14] which is about 375 times of the resolution limit of the best optical microscope.

Secondary electrons are generated by scattering of the primary electron beam by the loosely bound conduction-band electrons of the specimen[15]. Due to the small energy associated with this electronic transition, secondary electrons have a low exit energy of only a few electronvolts and that constrains their traveling paths. Although secondary electrons are generated along the entire trajectory of the beam electron within the specimen, only the ones generated within a few nanometers beneath the specimen's surface are likely to escape and

thus be detected. Such shallow escaping depth of secondary electrons makes SEM suitable for imaging the surface of a specimen.

Another aspect where SEM is superior to optical microscopes is that the narrow electron probe aperture leads to a large depth of field, which means the ability of maintaining focus across a larger range of distance. As a result, the three-dimensional details on a specimen's surface will appear sharp, regardless of surface roughness. Figure 2.10 gives an example SEM image of the back of a bean plant's leaf, the texture from raised wall of cells in the vein can been observed clearly under a 350× magnification. The combination of a large magnification, small signaling depth, and, a large depth of field makes SEM a favorable technique for studying surface topographic features of the thin film materials grown for this work.

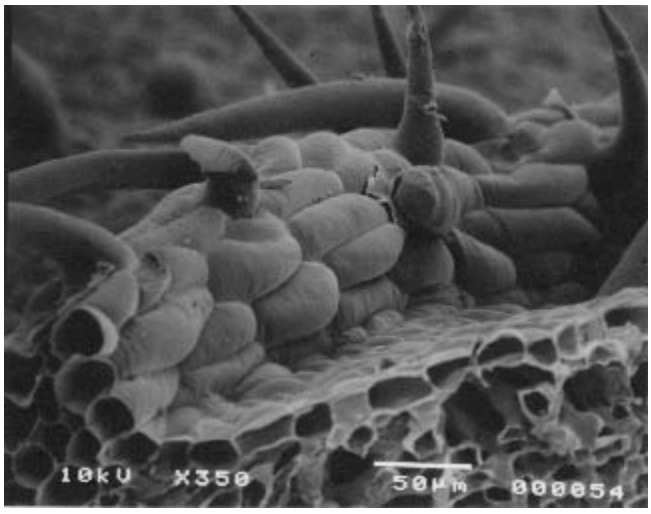

Figure 2.10: A SEM image taken on the back of a leaf showing the raised wall of cells is the vein. Image courtesy of Museum of Science, Boston.

However, trying to obtain images of less conductive specimens, like the $Mg_xZn_{1-x}O$ and ZnS_xO_{1-x} alloy films in this work, faces the challenge of charging. The imaging process of SEM is based upon scanning a specimen with charged particles. A specimen with poor conductivity tends to have electrostatic charges accumulated on its surface. As enough charges build up, the specimen's surface turns into a retarding field for the primary electron beam. Specimen charging could cause strong image distortions. An extreme case is that the primary electrons are directly deflected away from a charging specimen, without interacting with the surface of the specimen. The deflected primary electrons then land on the inner walls of the SEM chamber where they can excite secondary electrons and generate an image of the interior of the chamber, as shown in Figure 2.11.

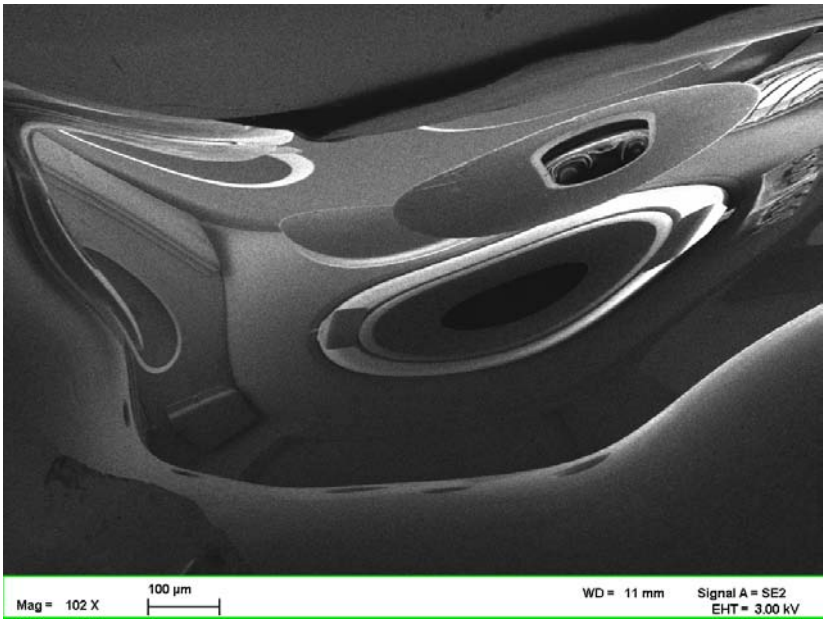

Figure 2.11: An insulating specimen under SEM tends to have electrostatic charges accumulated on its surface. The charges can be built up to form a field which deflects the primary electrons away before they impact the surface of the specimen. The primary electrons then land on the inner walls of the SEM chamber, generating an image of the interior of the chamber instead.

Lowering the energy of the primary electron beam could reduce the charging artifacts. However, the most efficient way of preventing charging is to create a contour in order to dissipate the electrons, by coating an insulating specimen with a thin layer of a conductive material. The thickness of the coated layer needs to be controlled with caution, as the layer being too thin will not eliminate the charging in the specimen and the layer being too thick will reduce the strength of the signal for imaging. The coating materials used in this work include graphite and gold.

2.2.2 Energy-Dispersive X-Ray Spectroscopy

When the electrons in the primary beam are striking the specimen with sufficient energy, atoms in the specimen may be ionized and shell transitions may occur. Such transitions are accompanied by a release of the excess energy as an emission of an X-ray. The emitted X-ray has an energy characteristic of the parent element and therefore can be utilized for elemental analysis of the specimen.

The characteristic X-ray emission process can be better understood with an example using a Bohr model[16] which depicts an atom as a small nucleus surrounded by electrons which are confined to circular shells, as illustrated in Figure 2.12. When the energy of an electron in the primary beam is slightly greater than the binding energy of the K-shell electron, the bound K-shell electron can be ejected. In order to return the atom to its lowest energy state, an electron from an outer shell (M or L) of a higher energy will relax to the K-shell, filling the vacancy. Consequently, the energy difference corresponding to the transition can be released in the form of X-rays, and the remaining energy is released in other forms such as heat. If it is an L-shell electron that transited and filled the K-shell vacancy, a Kα X-

ray will be emitted. If an M-shell electron fills the K-shell vacancy, a Kβ X-ray will be emitted, instead.

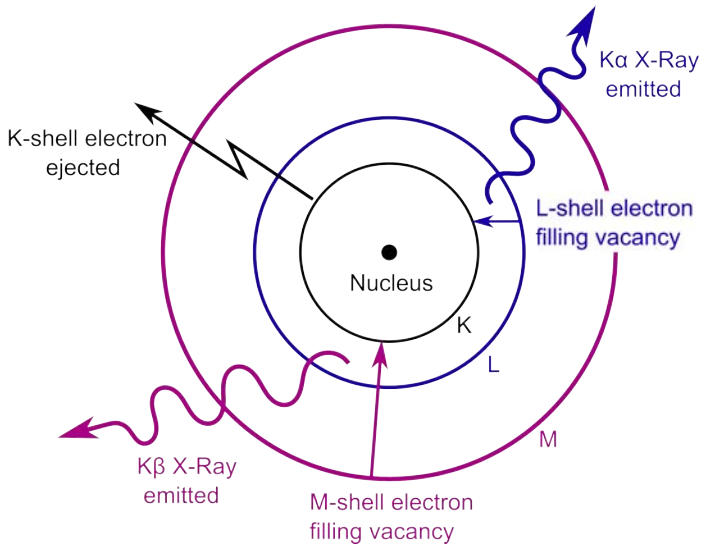

Figure 2.12: An example of characteristic X-ray emitting process illustrate using Bohr model of an atom. When the energy of a primary electron is sufficient to eject a K-shell electron, outer shell (L, or M) electrons will fill the K-shell vacancy and the amount of energy equal to such transition will be released in the form of X-rays.

With a proper detector equipped, such characteristic X-ray signal can be collected and displayed as a spectrum of intensity versus energy. The energies of characteristic X-rays identify the elements composed the sample, while the intensities of the characteristic X-ray peaks quantify the relative concentrations of the identified elements. This process is know as Energy Dispersive X-ray Spectroscopy (EDS) and many SEM system are equipped with accessories to perform this measurement.

Figure 2.13 is an example EDS spectrum. Peaks corresponding to different elements have been labeled and a standard program (i.e. NSS) can be used to determine the relative

concentration in atomic percentage and weight percentage of these elements by comparing with standard reference materials.

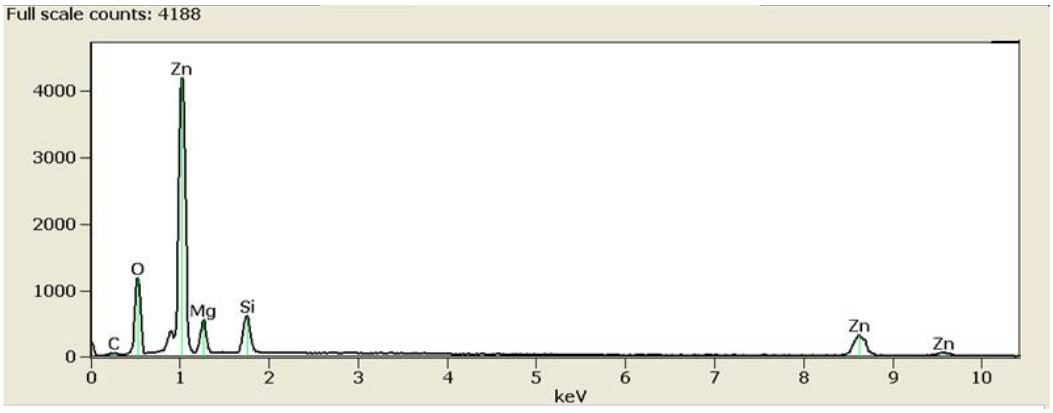

Figure 2.13: An example EDS spectrum of a $Mg_{0.3}Zn_{0.7}O$ film. Peaks of Silicon (Si) are from the quartz (SiO_2) substrate.

At the same time, in EDS the electron beam can be rastered over a selected area of the specimen to produce maps or line profiles showing the elemental distribution over this area in the specimen.

Comparing to secondary electrons, X-Rays can derive from deeper in the specimen as shown in Figure 2.14. The spatial resolution of EDS is practically estimated by the equation[17]

$$R = \frac{0.064 \cdot \left(E_0^{1.68} - E_c^{1.68}\right)}{\rho} \tag{2.4}$$

Where R is the spatial resolution in μm; E_0 is the energy of the primary electron beam in keV; E_c is the critical excitation energy in keV; ρ is the mean specimen density in g/cm^3. Clearly, the sampling volume depends on the voltage of the primary electron beam and the nature of

the specimen. For example, if K-lines of Zinc (Zn) excited at E_0=15 keV in $Mg_xZn_{1-x}O$ alloys were to be analyzed, assuming that the density of the alloy falls between that of the two end members, an X-ray spatial resolution of 0.65 to 1.0 μm could be achieved. For the thin films grown via sputtering for this work, the sampling volume could be slightly greater than the theoretical values given above, due to slightly lower densities of the alloys than that of pure bulk materials. Such a resolution is sufficient of penetrating through the entire film and yielding reliable reading of the elemental composition of the films.

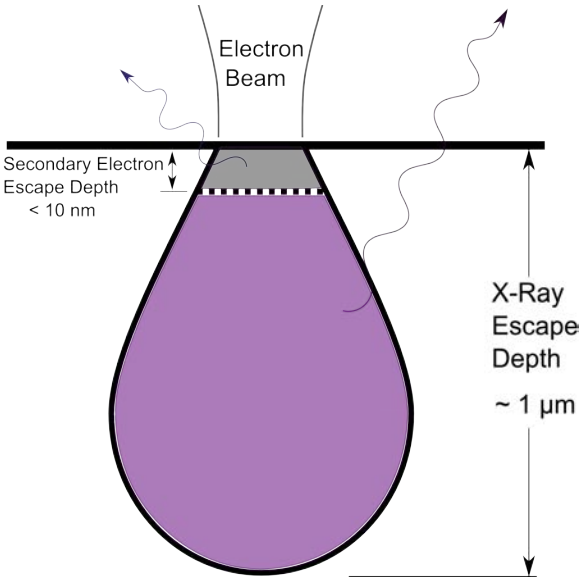

Figure 2.14: A schematic showing the difference in sampling volume between SEM and EDS. Although secondary electrons and X-rays are both generated along the entire trajectory of the primary beam electron within the specimen, secondary electrons can escape from only a few nanometers beneath the specimen's surface due to their low energy, while X-rays generated throughout the entire volume of trajectory can escape and be detected.

It is worth noting that the sampling volume becomes crucial when analyzing the relative composition of sulfur (S) and oxygen (O) in the ZnS_xO_{1-x} films grown on quartz (SiO_2) substrate. If the X-rays penetrate into the substrate, signals of O originated from SiO_2 will be

detected and are indistinguishable from those originated from the ZnS_xO_{1-x} films and cause ambiguity in determining the actual O composition in the films. According to Equation 2.4, in cases like this, reducing the energy of the primary electron beam (E_0) will result in a smaller penetration depth of the X-rays and thus signals originated from the substrate could be avoided. However, the primary beam needs enough amount of energy in order to to excite shell transitions in the atoms. Therefore the choice of the E_0 value should be made with a balance between the spatial resolution and the energy needed for a certain type of ionization.

EDS can provide a rapid survey of the elements present in the specimen and a quantitative analysis of their relative composition. It serves as a useful technique in the study of alloyed materials.

2.2.3 X-Ray Diffraction

X-ray diffraction (XRD) is a nondestructive analytical technique for the study of crystal structures and atomic spacing in crystalline materials.

A crystal consists of a periodic arrangement of atoms into a lattice and such arrangement can be viewed as sets of evenly spaced atomic planes. When irradiated by a monochromatic beam of X-ray, an atomic plane can act as a partially transparent mirror. Part of the X-ray beam will be reflected and part will be transmitted and may be reflected by another plane of atoms deeper into the material. Figure 2.15 shows a set of atomic planes with spacing d being irradiated by a beam of X-ray of wavelength λ, at an angle θ. Since the wavelength of X-rays are comparable to the spacing between atomic planes, constructive interference between two reflected beams can occur when the path difference between the two beams equals a multiple of the incident wavelength. This condition is know as Bragg's law and can be summarized by equation[18]

$$n \cdot \lambda = 2 \cdot d \cdot \sin\theta \tag{2.5}$$

where n is an integer.

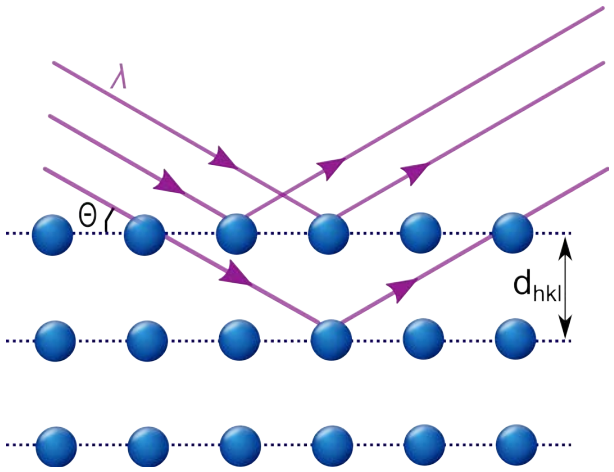

Figure 2.15: A schematic illustrating Bragg's law. A beam of X-ray of wavelength λ is incident on a set of atomic planes with spacing d, at an angle θ. If the path difference between the two reflected beams equal to a multiple of the incident, constructive interference will occur and cause an enhancement in the intensity.

Typically, the intensity of the scattered X-ray beam is detected as a function of 2θ and the measurement is based on the first-order reflected beam so that $n = 1$ in Equation 2.5.[19] For a given wavelength of incident X-ray beam, narrow and intense peaks can be observed at angles where constructive interference occurs. Each crystalline material usually has its unique set of d-spacings which gives rise to diffraction peaks at specific angles. By comparing the detected pattern of peaks with standard references, the crystal structure of the examined specimen can be identified. The peak position, relative intensity of peaks, and, line shapes also contain information such as strain in the lattice planes and the lattice constants.

However these information are beyond the scope of this work and will not be discussed in detail.

In this work the XRD measurement was performed by an X-ray powder diffractometer where a specimen is treated as a randomly oriented collection of particles which can produce diffraction spectra from all lattice planes for each given type of crystal[20].

2.3 Material characterization methods: Optical spectroscopy techniques

Sir Isaac Newton discovered that the sunlight is made up of a continuous series of wavelengths and introduced the word *spectrum* to describe this phenomenon in 1666, and then presented the principles required for spectroscopic investigations[21]. This set the cornerstone of the science of optical spectroscopy and made it one of the oldest field in material characterization.

When light is incident on a material, interactions between the incident light and the molecules in the material can yield three different phenomena: absorption, emission and scattering. Each of them leads to a different array of spectroscopy techniques, which make optical spectroscopy a diverse field. In this work transmission spectroscopy and Raman spectroscopy were utilized and thus will be discussed in detail in the following sections.

2.3.1 An introduction to the transmission spectroscopy

When the energy of incident light corresponds to the difference between two stationary energy levels of the molecules, absorption of radiation will take place. Absorption spectra can be utilized for a wide range of applications from classifying the strains of bacteria[22], determining the safety of drugs[23], to analyzing the chemical elements present in stars[24].

Transmission measurements represent equivalent information as absorption measurements and one can be calculated from the other via a mathematical transformation. A transmittance spectrum has the maximum intensities at wavelengths where the absorbance spectrum yields the weakest intensities since more light is transmitted through the specimen.

One common approach to conduct transmission measurements of a material is using a spectrophotometer. A spectrophotometer is an instrument that measures the amount of photons, in other words, the intensity of light, being transmitted through a specimen as a function of the incident wavelength.

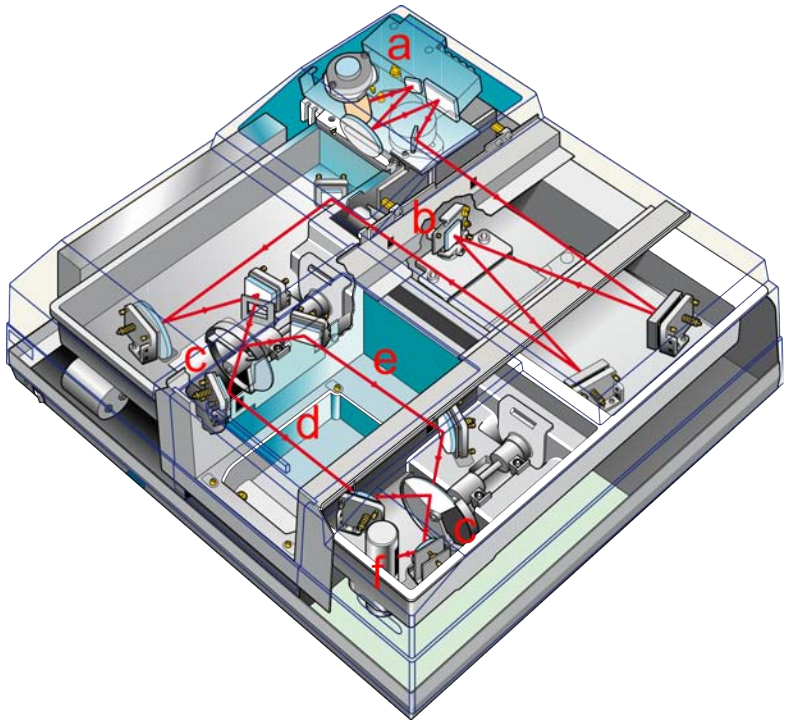

*Figure 2.16: A schematic of the interior of the Cary 300 spectrophotometer, showing **a)** the UV and visible light sources, **b)** the diffraction grating for wavelength selection, **c)** a pair of synchronized beam choppers which alternate the beam between **d)** the sample path and **e)** the reference path, and **f)** a photomultiplier tube for the light detection. Schematic courtesy of Agilent.*

The equipment used in this work is a Cary 300 UV-Vis spectrophotometer, with an operating range from 190 nm to 800 nm (6.53 to 1.55 eV) and a resolution of 0.2 nm. This system is capable of operating in double-beam mode and all measurements discussed in this work were performed in such mode in order to eliminate virtually all the background effects of the scan, leaving signal only from the specimen of interest. Figure 2.16 shows a schematic of the internal of the equipment: Light from the tungsten lamp (Figure 2.16 (a)) passing through the monochromator (Figure 2.16 (b)) is reflected at different angles for different wavelengths by a grating inside the monochromator. By rotating the grating a monochromatic light beam passes through a slit, goes through two synchronized beam choppers (Figure 2.16 (c)) and gets switched between two different paths alternately. One path (Figure 2.16 (d)) travels and impinges orthogonally on the surface of the specimen to be analyzed. While the other path (Figure 2.16 (e)) is used as a reference for 100% transmittance. For the transmission measurement of a thin film sputtered on a substrate, a blank substrate is placed into the reference beam path so that signals from the substrate can be subtracted. The beam path ultimately reaches a photomultiplier tube (Figure 2.16 (f)) where its intensity is measured.

When applied to a semiconductor material, an optical transmittance spectrum can convey valuable information of the material's properties with proper analytical methods applied. More details will be discussed in Chapter 3.

2.3.2 Raman Spectroscopy: Working principles

When a molecular system is irradiated by light whose energy does not correspond to the difference between any two stationary energy levels of the molecules, scattering of radiation

will occur[25]. Most scattering of radiation proceed without change of energy. However, Indian physicist Dr. Chandrasekhara Venkata Raman and his collaborators discovered the process of light scattering in molecules with change of energy and its physical essence in 1928[26]. Such inelastic light scattering process is thus named Raman Scattering. After decades of developing Raman scattering became a widely used non-destructive method for investigating inherent crystal properties including crystal structure and bond energies[27–29].

Figure 2.17 illustrates possible light scattering processes that can take place when a monochromatic radiation is incident on a molecular system which is approximated as a model of an array of differing masses m_1 and m_2 connected by springs. The energy of light *E,* in unit of (eV), is related to its frequency ν, in unit of (1/s), via the Plank formula

$$E = h\nu \tag{2.6}$$

Where *h* is the Plank constant (4.1357×10^{-15} eV·s).

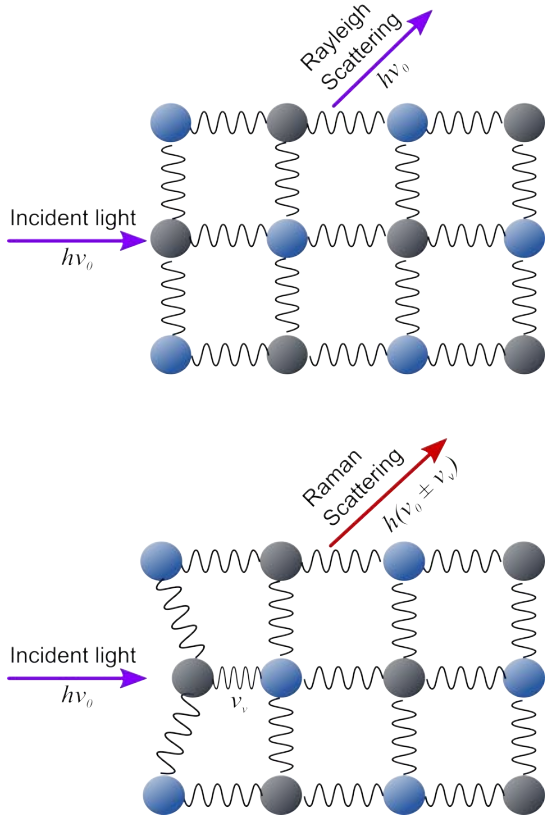

Figure 2.17: Light scattering processes in a molecular system. The majority of the incident light is scattered off elastically from the molecules without any change in energy. Such process is called Rayleigh scattering. A small portion of the incident light goes through Raman scattering process and has its energy altered by interacting with the vibrations in the molecules.

The majority of the light beam is scattered off elastically from the molecules which are much smaller than the wavelength of the incident radiation. This process is known as Rayleigh scattering, after Lord Rayleigh, who explained this phenomenon in terms of classical radiation theory in 1871[30]. While a small percentage of the intensity in the beam go through Raman scattering process and its energy is altered by interacting with the vibrational energy levels in the molecules. A simple way of understanding the mechanism of different scattering processes is via an energy level diagram as shown in Figure 2.18.

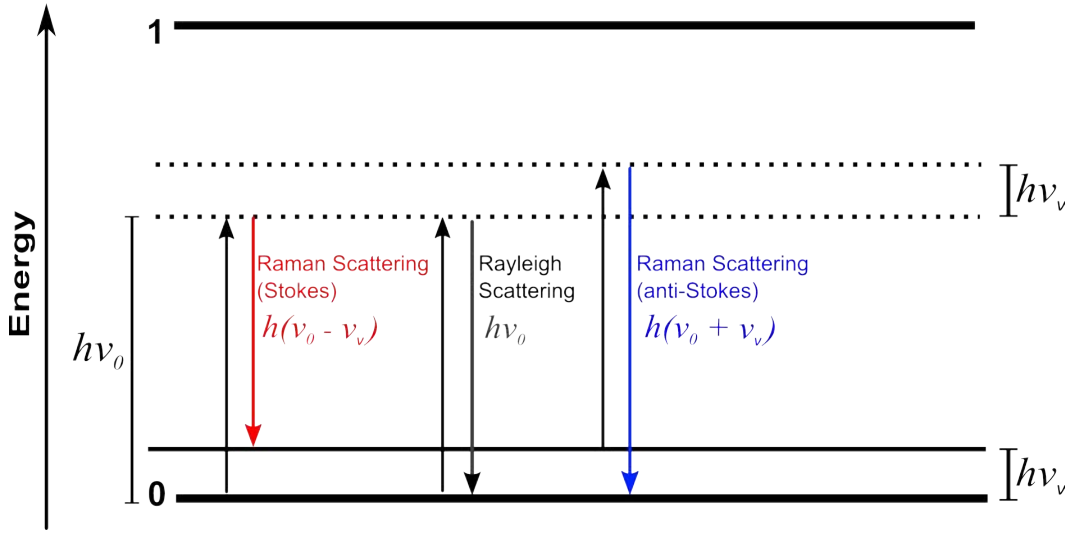

Figure 2.18: Different scattering mechanisms illustrated in the term of energy level diagram. The bold solid lines 0 and 1 represent the ground electronic energy level and the first excited energy level, respectively. The dashed lines represent two virtual levels of the molecule, separated by the energy of a vibration in the lattice hv_v. When light with energy hv_0 is incident on a molecular system, in some cases it loses some of its energy to the molecular system, being scattered off with energy $h(v_0-v_v)$; In other cases it gains some energy, getting scattered off with energy $h(v_0+v_v)$. These two scattering processes are known as Stokes and anti-Stokes Raman scattering, respectively .

The solid lines denoted as 0 and 1 represent the ground electronic energy level and the first excited energy level, respectively. The dashed lines denote two virtual levels of the molecule, separated by the energy of a vibration in the lattice hv_v. Such vibration is called a phonon. When light with energy hv_0 is incident on a molecular system, in some cases it leaves part of its energy behind as a phonon and is then scattered off with energy $h(v_0-v_v)$; While in other cases molecules in the excited states interact with the incident light and return to the ground state. In this process the incident light gains energy of a phonon and then get

scattered off with energy $h(\nu_0+\nu_v)$. The changes to lower and higher energy are known as Stokes and anti-Stokes Raman scattering, respectively[31].

According to Boltzmann's Law[32], at room temperature, most of the molecules will be found in the ground state and only a small population of them occupy the excited level. Thus there is a much lower probability that a photon will be Anti-Stokes scattered. As a result, most Raman measurements are performed considering only the Stokes scattered light.

In Raman spectroscopy, a monochromatic light source (usually a laser) with known energy is serving as the incident light. Upon identifying the energy of Stokes Raman scattering light, the phonon energy of the molecules can be obtained by the conservation of energy.

$$E_{phonon} = h\nu_v = h\nu_0 - h\nu_{Raman(Stokes)} \tag{2.7}$$

The phonon energy $h\nu_v$ is characteristic to certain molecular system and independent to the energy of incident light. Consider the mass-spring model in Figure 2.15 again. The lattice vibration of such a system can be approximated as a harmonic oscillator and thus can be expressed in terms of Hooke's Law[33]

$$E_{phonon} = h\nu_v = \frac{1}{2\pi c}\sqrt{\frac{k}{\mu}} \tag{2.8}$$

where k is the spring constant and μ is the effective mass which is defined as

$$\mu \equiv \frac{m_1 + m_2}{m_1 \cdot m_2} \tag{2.9}$$

Naturally, phonon energy E_{phonon} is sensitive to changes in values of the masses of molecules and of spring constant k. This nature of phonon energy makes Raman spectroscopy a very useful technique of probing an alloy system, such as $Mg_xZn_{1-x}O$. Upon successfully

substituting Mg atoms into a ZnO lattice, both the effective mass μ of the system and the spring constant k will change due to a smaller atomic weight of Mg and a stronger bond of Mg-O. These changes can be detected by Raman spectroscopy and give valuable information about the alloy system. More details will be discussed in Chapter 4.

The conventional unit of choice for Raman measurements is the wavenumber $\tilde{\nu}$ in unit of (cm^{-1}). It is related to the frequency ν via the relation:

$$\tilde{\nu}=\frac{\nu}{c} \tag{2.10}$$

with c being the speed of light (2.9979×10^{10} cm/s).

2.3.3 Resonance Raman Spectroscopy

When the energy of the incident radiation is close to an electronic transition in the material, resonance Raman scattering occurs. In the resonance regime the acquired signal is significantly enhanced, often by a factor of 10^4 or more[33]. This makes resonance Raman spectroscopy a more sensitive technique for analyzing colored compounds since the enhanced signal intensity is able to overcome strong fluorescence. Also, such enhancement gives it advantages in obtaining signal from materials with low concentrations.

It is worth noting that under resonance condition, higher order overtones of one fundamental vibration mode can be observed in the spectrum. The behavior of the energy separation between adjacent overtones from lower to higher order can be investigated in order to understand the harmonic or non-harmonic nature of the specimen[34].

Another important aspect of resonance Raman spectroscopy is that it can selectively pick out and positively identify small domains of molecules embedded in a matrix, since only the

signal given by molecules involved in the resonance process will get enhanced. When different energies of excitation are utilized, selective resonant enhancement occurs for each excitation accordingly with its energetically compatible composition in a specimen. This technique is often referred as selective resonance Raman scattering (SRRS). It serves as an efficient tool and is wildly used in analyzing the domains of the segregated minority phase in a material, which can be in a size regime too small to be detected by other experimental methods. In this work, the phase segregation issue in $Mg_xZn_{1-x}O$ alloy films will be investigated via SRRS and the details will be discussed in Chapter 4.

The Raman spectroscopy used in this work is a JobinYvon/Horiba T64000 Photoluminescence/Raman system which is capable of a spot size of less than 1 μm. It consists of a high-resolution triple monochromator, a UV confocal microscope, and a charge coupled device (CCD) for photon detection. A monitor screen is also equipped for viewing the area being sampled and the laser spot. With the high-resolution triple monochromator, the wave number accuracy is ±1 cm^{-1}. The gratings are 2400 lines/mm for the spectrometer and 1800 lines/mm for the premonochromator, this combination provides a reasonable compromise between resolution and range. The confocal microscope increases the spatial, lateral and depth resolutions to the diffraction limits. The CCD detector is optimized for the UV and has a spectral resolution better than two pixels.

Figure 2.19: The equipment configuration in this work. ***a)*** *The JobinYvon/Horiba T64000 Photoluminescence/Raman system and* ***b)*** *the Kimmon He-Cd laser of 325 nm (at right) and the Lexel SHG frequency doubled argon ion laser operating at 244 nm (at left).*

Along with the Raman system two lasers were utilized in this work: a Kimmon He-Cd laser of 325 nm (3.81 eV) and a Lexel SHG frequency doubled argon ion laser operating at 244 nm (5.08 eV). The He-Cd 325 nm laser has a beam diameter of 1.2 mm and an output power of 50 mW. The LEXEL SHG 244 nm deep UV laser has a beam diameter of 0.8-0.9 mm and a tunable output power up to 100 mW. both lasers are in continuous wave mode.

A photograph of the Raman system and the lasers is shown in Figure 2.19.

2.3.4 Raman Spectroscopy at low temperatures

Investigating Raman scattering of materials under temperatures well below room temperature lead to information on phonon dynamics which can be useful in understanding the mircro strcuctral properties of the materials. With the help of an Instec HCS621V microscopy temperature cell the temperature dependent Raman spectroscopy experiments can be conducted. This temperature cell is capable of operating in the range from 77 K to 873 K. The window glass equipped on this cell in highly transparent in the UV range.

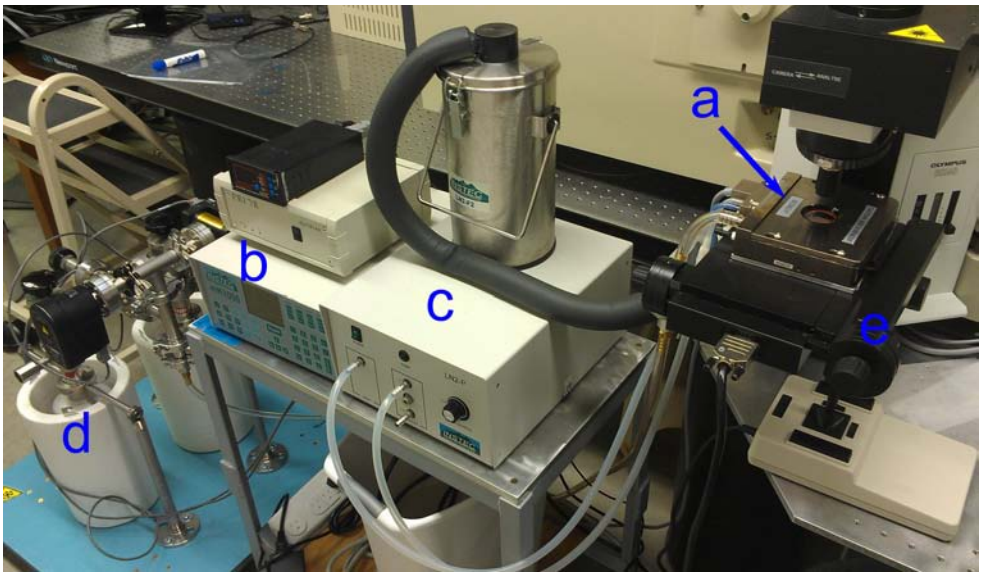

Figure 2.20: The equipment setup for temperature dependent Raman spectroscopy. ***a)*** *the Instec temperature cell whose operating temperature ranges from 873 K to 77 K with the* ***b)*** *temperature controller and the* ***c)*** *cooling system.* ***d)*** *An adsorption pump creates vacuum environment inside the cell for a better thermal isolation of the hot/cold stage. And* ***e)*** *a motorized stage guarantees the same area being probed in spite of the thermal expansion or contraction in the specimen.*

Figure 2.20 shows the setup for temperature dependent Raman scattering data acquisition below room temperature. An Instec's MK1000 controller and an Instec's

LN2-SYS cooling system allows for fast and accurate cooling for the stage, using liquid nitrogen as the cooling agent. Such combination of equipments has a temperature resolution of 0.01 K. A vacuum environment (10^{-2} Torr) inside the stage is created by a Duniway sorption pump which absorbs most gas molecules on the vast surface area of the cooled molecular sieve. Such arrangement provides excellent thermal isolation of the cold stage without the risk of oil contamination. A motorized stage guarantees the consistency of the sampling area in spite of the thermal expansion and contraction in the specimen during the temperature changing.

In this work temperature dependent Raman spectroscopy was performed on representative $Mg_xZn_{1-x}O$ films to understand the correlation between the mechanism of the broadening of Raman peak and the disorder in electronic states. The results and discussion will be presented in Chapter 4.

2.4 Conclusion

In this chapter the reactive sputtering deposition method utilized to fabricate $Mg_xZn_{1-x}O$ and ZnS_xO_{1-x} thin films for this work was introduced and the technical specifications of the equipment were discussed. As a cost effective method with a straightforward mechanism, reactive sputtering has been widely used from research laboratories to industrial volume production lines. In order to achieve high quality materials with desired compositions, many detailed aspects of growth condition should be taken into consideration. Material synthesis, in some respects, is an art in itself.

This chapter also gave a brief introduction to the working principles and advantages of various material characterization methods utilized in this work. SEM provides high resolution images of a specimen's surface with a high depth of field. The elemental

compositions of the films were obtained using EDS. With a typical sampling volume in the scale of micrometer, EDS is capable of acquiring signal throughout the entire thickness of a film. XRD spectra of the films gave information about the crystal structures and qualities of the alloyed materials. Two types of optical spectroscopy techniques: transmission spectroscopy and Raman spectroscopy were employed in this work. Both techniques are information-dense and serve as useful tools for analyzing semiconductor alloy materials.

2.5 References

1. Holland, L. *Vacuum deposition of thin films*. (Wiley, 1966).

2. Grove, W. R. On the Electro-Chemical Polarity of Gases. *Philos. Trans. R. Soc. Lond.* **142,** 87–101 (1852).

3. Wasa, K., Kitabatake, M. & Adachi, H. *Thin Film Materials Technology: Sputtering of Compound Materials*. (William Andrew, 2004).

4. Gibson, D. R., Brinkley, I., Hall, G. W., Waddell, E. M. & Walls, J. M. Deposition of multilayer optical coatings using closed-field magnetron sputtering. in (Ellison, M. J.) 628601–628601–13 (2006).

5. Gupta, A. & Compaan, A. D. All-sputtered 14%CdS/CdTe thin-film solar cell with ZnO:Al transparent conducting oxide. *Appl. Phys. Lett.* **85,** 684–686 (2004).

6. Cohen-Solal, G., Zozime, A., Motte, C. & Riant, Y. Sputtered mercury cadmium telluride photodiode. *Infrared Phys.* **16,** 555–559 (1976).

7. Zhang, H. W., Liu, Y. L. & Zhong, Z. Y. An improved microchip thin film transformer formed by vacuum evaporation and sputtering. *Vacuum* **62,** 1–6 (2001).

8. Edwards, J. L. & Roedel, R. J. Use of a sputtered SiO_2 coating for surface protection during ‘leaky tube’ diffusion of Zn into GaAs. *Electron. Lett.* **19,** 962–963 (1983).

9. Banks, B. A., Mirtich, M. J., Rutledge, S. K. & Swec, D. M. Sputtered coatings for protection of spacecraft polymers. *Thin Solid Films* **127,** 107–114 (1985).

10. Anders, A. Physics of arcing, and implications to sputter deposition. *Thin Solid Films* **502,** 22–28 (2006).

11. Hollands, E. & Campbell, D. S. The mechanism of reactive sputtering. *J. Mater. Sci.* **3,** 544–552 (1968).

12. Howson, R. P. The reactive sputtering of oxides and nitrides. *Pure Appl. Chem.* **66,** 1311–1311 (1994).

13. Huso, J. Advanced optical alloys: thin films and phonon properties. (2012).

14. Gabriel, B. L. *SEM: a user's manual for materials science*. (American Society for Metals, 1985).

15. Newbury, D. E. *Advanced scanning electron microscopy and X-ray microanalysis*. (Plenum Press, 1986).

16. Bohr, N. On the constitution of atoms and molecules Part I. *Philos. Mag. Ser. 6* **26,** 1–25 (1913).

17. Friel, J. J. *Microbeam Analysis*. (San Francisco Press).

18. Suryanarayana, C. & Norton, M. G. *X-Ray diffraction: a practical approach*. (Plenum Press, 1998).

19. Freund, L. B. & Suresh, S. *Thin film materials: stress, defect formation, and surface evolution*. (Cambridge University Press, 2003).

20. Morrison, J. L. The realization of ultraviolet luminescent nanocrystals and ceramics. (2011).

21. Newton, I. *Opticks; or, A treatise of the reflections, refractions, inflections & colours of light. Based on the 4th ed., London, 1730;* (Dover Publications, 1952).

22. Stafsnes, M. H. *et al.* Isolation and characterization of marine pigmented bacteria from Norwegian coastal waters and screening for carotenoids with UVA-blue light absorbing properties. *J. Microbiol.* **48,** 16–23 (2010).

23. Tønnesen, H. H. *The photostability of drugs and drug formulations*. (Taylor & Francis, 1996). at <http://site.ebrary.com/id/10057202>

24. Bauman, R. P. *Absorption spectroscopy*. (Wiley, 1962).

25. Barańska, H., Łabudzińska, A. & Terpiński, J. *Laser Raman spectrometry: analytical applications*. (PWN-Polish Scientific Publishers ; E. Horwood ; Distributors, Halsted Press, 1987).

26. Raman, C. A New Type of Secondary Radiation. *Nature* **121,** 501–502 (1928).

27. Hummel, R. E. & Wissmann, P. *CRC Handbook of Optical Properties: Optics of Small Particles, Interfaces and Surfaces*. (C R C Press LLC, 1997).

28. Porto, S. P. S. in *Light Scatt. Spectra Solids* (Wright, G. B.) 1–24, (Springer Berlin Heidelberg, 1969).

29. Pinczuk, A. & Burstein, E. in *Light Scatt. Solids I* 23–78, (Springer Berlin Heidelberg, 1983).

30. Lord Rayleigh. On the scattering of light hy small particles. *Phil Mag* **XLI,** 447–454 (1871).

31. Grasselli, J. G. & Bulkin, B. J. *Analytical Raman spectroscopy*. (Wiley, 1991).

32. Landau, L. D., Pitaevskii, L. P. & Lifshìtz, E. M. *Statistical physics*. (Butterworth-Heinemann, 1980).

33. Smith, E. & Dent, G. *Modern Raman spectroscopy: a practical approach*. (J. Wiley, 2005).

34. Huso, J., Morrison, J. L., Bergman, L. & McCluskey, M. D. Anharmonic resonant Raman modes in $Mg_{0.2}Zn_{0.8}O$. *Phys. Rev. B* **87,** 125205 (2013).

Chapter 3 Analytical methods for the characterization of semiconductor alloys from transmittance spectra

When applied to a semiconductor thin film material, the optical transmittance measurement can convey valuable information of the material's properties. The current chapter will introduce:

- The development of the derivative analysis method for an accurate determination of the optical band gap of a semiconductor alloy from its optical transmittance spectrum.
- The Urbach energy analysis for studying the electronic energy band tailing in semiconductor alloys.
- Calculating the thickness of a film from the interference pattern in its transmittance spectrum.

3.1 The development of an analytical method for an accurate determination of the band gap energy in alloys from transmittance spectra

A semiconductor is a material which has electrical conductivity to a degree between that of metal and that of an insulator. In a semiconductor the valence band is filled by electrons and the conduction band is separated in energy from the upper edge of the valence band. This energy range between the valence and the conduction band, where no electron states can exist, is characterized as a band gap (E_g). When exposed to light irradiation, a semiconductor material is transparent to photons with energies lower than its band gap energy E_g. However, photons with energies higher than E_g will be absorbed by the semiconductor in which electrons will be excited from the valence band to the conduction band, as illustrated in Figure 3.1.

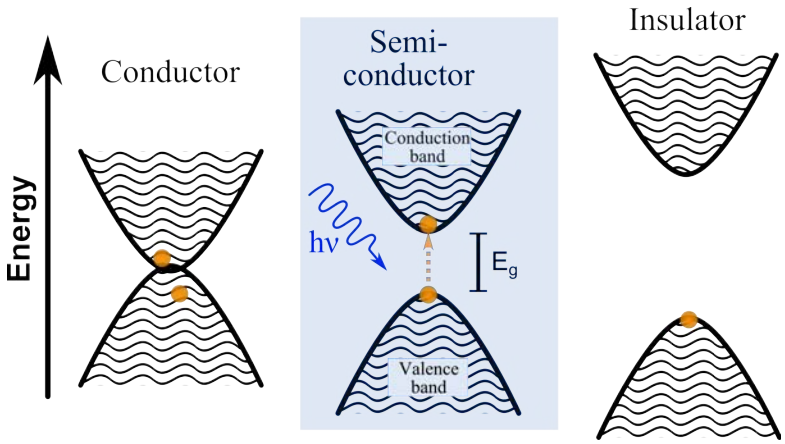

Figure 3.1: An illustration of light absorption in semiconductors. In semiconductors a valence band is filled by electrons and is separated from a conduction band by a gap in energy (band gap). Incident light with an energy lower than the band gap will be transmitted through the material. However, light with sufficient energies can excite electrons from the valence band to the conduction band, resulting the absorption of light.

Such a light absorption process can be observed via transmission spectroscopy. Figure 3.2 shows an example transmittance spectrum of a ZnO film. The sinusoidal pattern exhibited in the highly transparent region is due to thin film interference. The thickness of a film can be calculated from the interference pattern and details will be discussed later in Section 3.3. The abrupt cutoff in the measured transmittance corresponds to the light absorption caused by the electronic transition from the valence band to the conduction band. Following proper analytical methods, the value of band gap energy E_g of the semiconductor can be extrapolated.

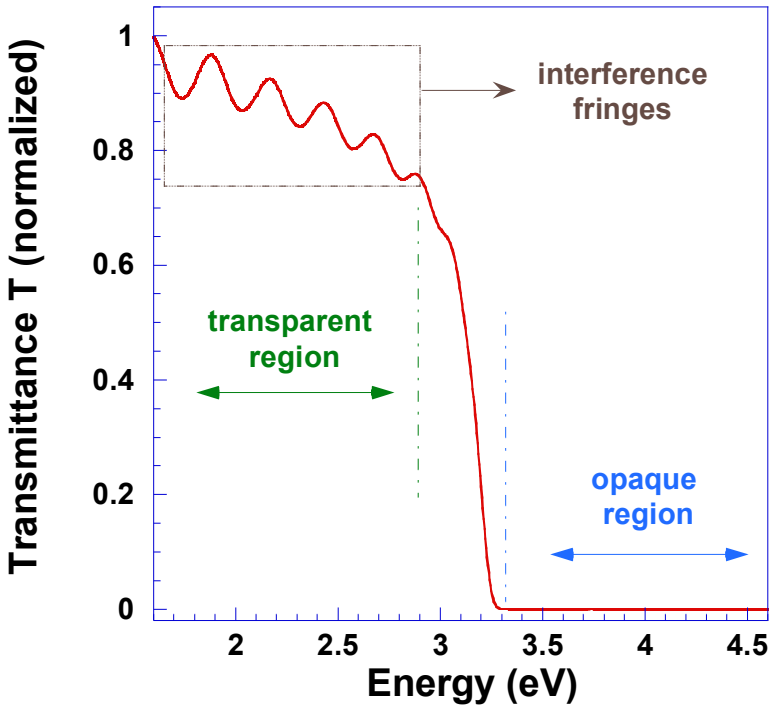

Figure 3.2: A transmittance spectrum of a ZnO film grown via sputtering. The horizontal axis is the energy of the incident light and the vertical axis is the measured transmittance, normalized. The film is highly transparent to light with energies below the band gap and is opaque to light with energies higher than the band gap. A cutoff in the transmittance at approximately 3.2 eV suggests where the inter-band electronic transitions occur. The sinusoidal pattern at the transparent region is due to thin film interference.

3.1.1 The absorption of light in thin film semiconductor materials

A beam of light with frequency *v* traveling in a material along a direction $\vec{x}$ at a speed *V* can be considered as a propagating plane wave and thus can be described as[1]

$$U(\vec{x},t) = A_0 \cdot e^{i\left(2\pi\nu t - \vec{k}\cdot\vec{x} + \varphi\right)} \tag{3.1}$$

where $\vec{k}$ is the wave vector with a magnitude $k = \frac{2\pi\nu}{V}$ and with a direction in which the wave propagates. This expression is rewritten as

$$U(x,t) = A_0 \cdot e^{i\left(2\pi\nu t - \frac{2\pi\nu x}{V} + \varphi\right)} \tag{3.2}$$

In a material with a refractive index of $\eta_r = n - i\kappa$, the speed of light *V* can be obtained by[1]:

$$\frac{1}{V} = \frac{\eta_r}{c} = \frac{n}{c} - \frac{i\kappa}{c} \tag{3.3}$$

where the real part *n* and the imaginary part κ of the refractive index is associated to the phase velocity and the absorption loss to the light wave, respectively. Substituting Equation 3.3 into Equation 3.2, an expression describing the light propagating through a material as a plane wave is obtained:

$$U(x,t) = A_0 \cdot e^{\frac{-2\pi\nu\kappa x}{c}} \cdot e^{i\left(2\pi\nu t - \frac{2\pi\nu xn}{c} + \varphi\right)} = A_x \cdot e^{i\theta_x} \tag{3.4}$$

where $A_x = A_0 \cdot e^{\frac{-2\pi\nu\kappa x}{c}}$ and $\theta_x = \frac{2\pi\nu xn}{c} - 2\pi\nu t + \varphi$ is the amplitude and the phase angle of the light wave after it traveled a distance *x*, respectively. The resultant amplitude A_x and phase angle θ_x indicate that as the light propagates in the material, its intensity is attenuated and its phase angle is altered.

Now let us focus on the transmission and absorption of light occurring in a film with thickness *t* and reflectivity *R*. A beam of light entered the film at normal incidence with intensity I_0. It traveled through and left the film with remaining intensity I'. The transmittance (T) of the material is defined as $T = \frac{I'}{I_0}$. In consideration of the reflection and transmission occurring on both the air-film interface and the film-substrate interface, along with the multiple internal reflections within the film, the transmittance T of the film can be obtained by[2]

$$T = \frac{I'}{I_0} = \frac{(1-R)^2 e^{\frac{-4\pi\nu\kappa x}{c}}}{1-R^2 e^{\frac{-8\pi\nu\kappa x}{c}}} = \frac{(1-R)^2 e^{-\alpha t}}{1-R^2 e^{-2\alpha t}} \tag{3.5}$$

Where $\alpha = \frac{4\pi\nu\kappa}{c}$ is defined as the absorption coefficient[2] of the film.

For semiconductor materials, the reflectivity R is insignificant and thus negligible near the absorption edge[3]. Therefore for the purpose of band gap analysis, the transmittance T of a semiconductor film with thickness t can be expressed as

$$T = e^{-\alpha t} \tag{3.6}$$

Consequently, with measured transmittance and film thickness t, the absorption coefficient α of a semiconductor film can be obtained:

$$\alpha = -\ln T \cdot t^{-1} \tag{3.7}$$

3.1.2 The conventional linear fitting analysis for band gap studies

For a semiconductor material with allowed direct electronic transitions (i.e. ZnO), the absorption coefficient α associated with inter-band optical absorption processes can be described by a model developed by Ridley et al.[4] based on quantum mechanics:

$$\alpha = \frac{8}{3}\beta a_H^2 \left(\frac{R_H}{E}\right)\frac{1}{\eta_r}\frac{p_{cv}^2}{2\mathrm{m}}\left(\frac{2m_r^*}{\hbar^2}\right)^{3/2}\left(E-E_g\right)^{1/2} \tag{3.8}$$

where E is the energy of incident light, η_r is the energy dependent refractive index, and, all other parameters are material constants. This model has been applied in optical band gap analysis in semicondutors[5]. Equation 3.8 can be written as

$$\alpha = C^* \frac{1}{E\,\eta_r}\left(E-E_g\right)^{1/2} \tag{3.9}$$

where $C^* = \frac{8}{3}\beta a_H^2 R_H \frac{p_{cv}^2}{2\mathrm{m}}\left(\frac{2m_r^*}{\hbar^2}\right)^{3/2}$ is a constant.

Comparing Equation 3.7 and Equation 3.9, a correlation between the band gap energy E_g and the experimentally measured transmittance T can be established as:

$$\alpha = -\ln T\, t^{-1} = C^* \cdot \frac{1}{E\,\eta_r}\cdot\left(E-E_g\right)^{1/2} \tag{3.10}$$

Equivalently,

$$\alpha^2 E^2 \eta_r^2 = \left(-\ln T \cdot t^{-1}\right)^2 E^2\,\eta_r^2 \propto \left(E-E_g\right) \tag{3.11}$$

According to Equation 3.11, a plot of $\left(\alpha^2 E^2 \eta_r^2\right)$ (an equivalent of $\left[\left(-\ln T \cdot t^{-1}\right)^2 E^2 \eta_r^2\right]$) versus E will yield a straight line over the energy range above E_g and will intersect the energy axis at the value of E_g. Therefore the value of band gap energy E_g

can be extrapolated via a fitting to the linear region of the plot, as shown in Figure 3.3. Here the thickness of the film was calculated from the sinusoidal interference pattern in the transmittance spectrum and the details will be discussed in Section 3.3. Values of the refractive index η_r were reported by Teng et al[6].

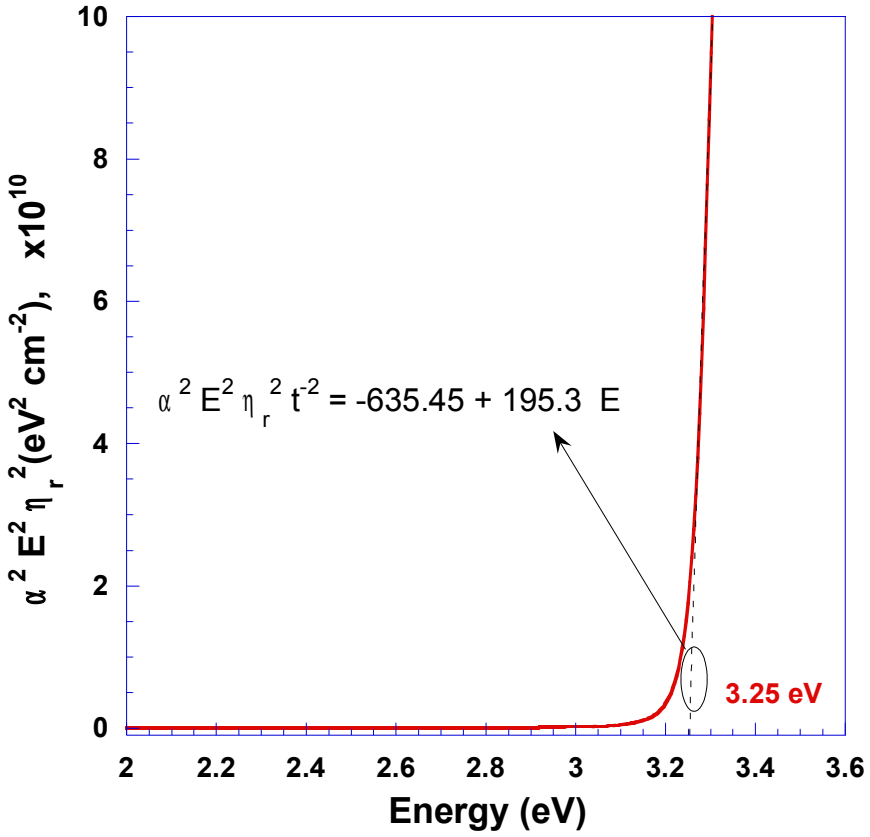

Figure 3.3: Extrapolating band gap energy via fitting the linear region of the $\left(\alpha^2 E^2 \eta_r^2\right)$ *versus E plot. The fitted line should intersect the energy axis at the value of band gap energy* E_g*. The energy dependent refractive index* η_r *is reported by Teng et al*[6]*. The film's thickness was calculated from the interference pattern at the high transmittance region and the details of calculation will be discussed in Section 3.3.*

3.1.3 The obstacles of the linear fitting analysis

The main obstacle encountered by the linear fitting analysis is its ambiguity when applied to materials with localized electronic energy states extending into the energy gaps. In these materials, electronic transitions involving in-band energy states will cause a broadened absorption edge[2,7], instead of an abrupt cutoff in the transmittance spectrum. When an absorption edge is not sharply defined, the usual extrapolation of the band gap energy via linear fitting may not render good results.

The Tauc plot of a $ZnS_{0.28}O_{0.72}$ film and a ZnO film grown for this work are shown in Figure 3.4 as an example. Comparing to the well defined absorption edge in the ZnO film, the absorption edge in $ZnS_{0.28}O_{0.72}$ film is broadened due to absorption processes associated with in-band electronic energy states. In such case the conventional linear fitting analysis is no longer a reliable method for band gap analysis. Due to the lack of a well defined linear region, linear fittings can be performed to selected regions in the plot and lead to arbitrary values of band gap energy, as shown in Figure 3.5.

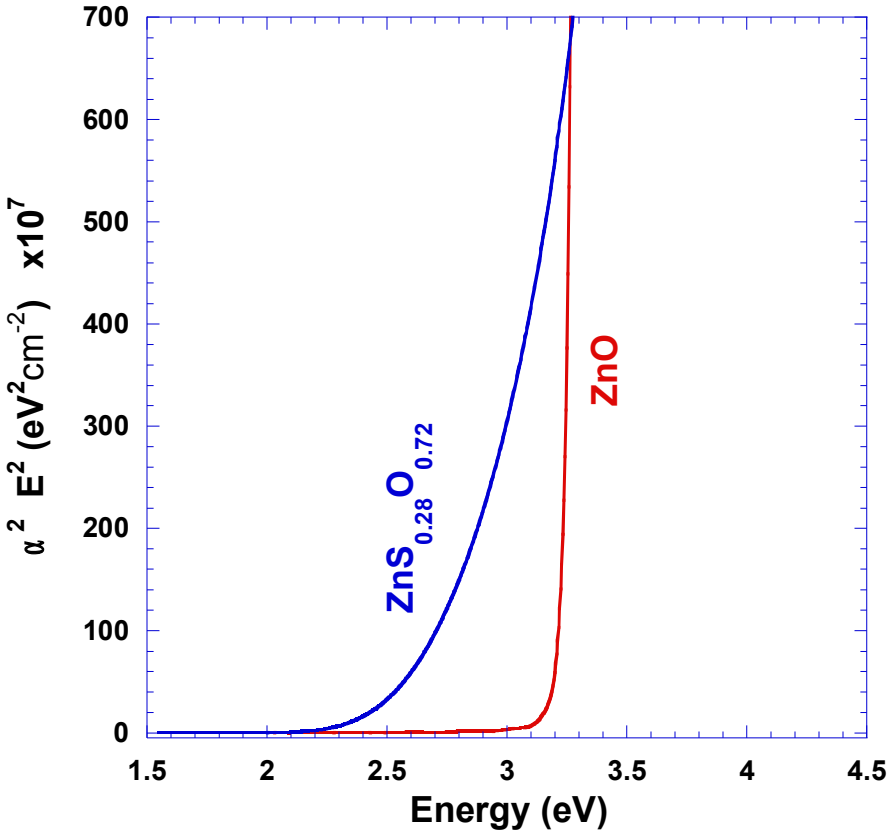

Figure 3.4: Tauc plot of a $ZnS_{0.16}O_{0.84}$ thin film and a ZnO thin film. Tauc plot of ZnO exhibits a well defined linear region while no obvious linear region in the plot of $ZnS_{0.16}O_{0.84}$ is observed due to sub-gap absorptions.

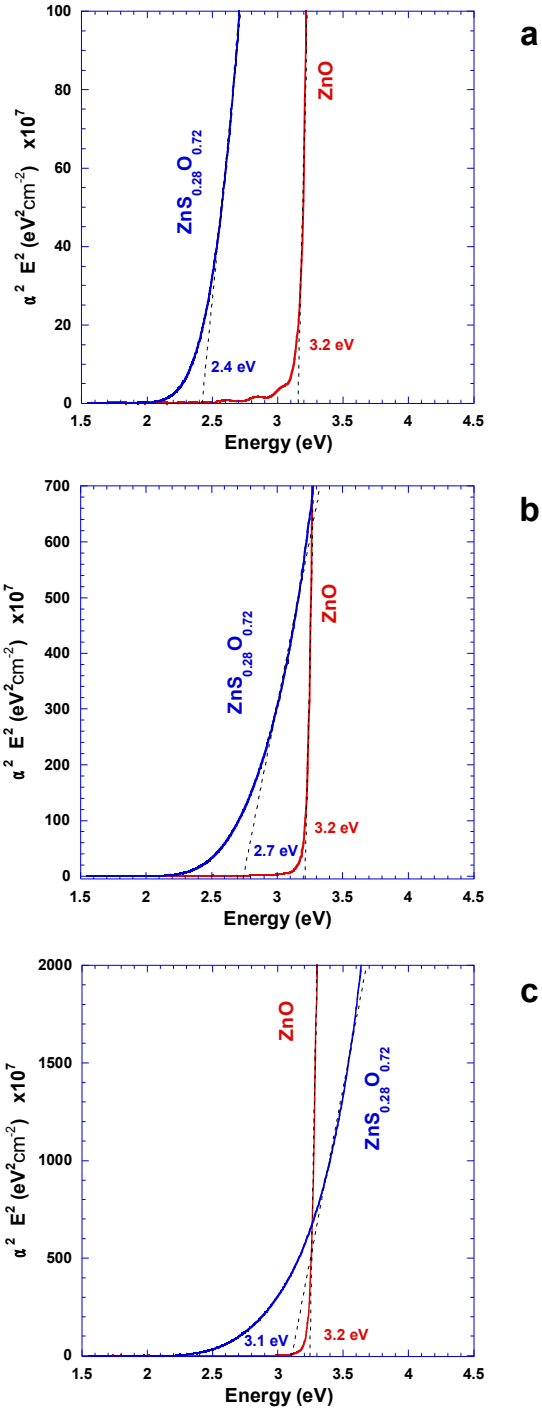

Figure 3.5: The linear fitting analysis for extrapolation band gap energy is not applicable to the $ZnS_{0.16}O_{0.84}$ thin film studied here due to the lack of well defined linear region in the Tauc plot. Fittings to differently selected regions of the plot ***(a)****,* ***(b)*** *and* ***(c)*** *give arbitrary values of E_g.*

Another issue of this linear fitting method is that experimentally determining the precise values of the energy dependent refractive index η_r of a material, especially around the band gap region, is not a trivial procedure. Thus in practice it is common to assume a constant η_r for a certain material and therefore a plot of $\left(\alpha^2 \cdot E^2\right)$ versus E could be utilized to obtain a reasonable value of band gap energy. Such approach is well known as the *Tauc plot* and has been widely used for determining the band gap in various semiconductor materials.[8–11]. For a material whose refractive index η_r does not show strong energy dependence, i.e. ZnO, assuming a constant η_r still yields reliable results. However, for a material whose refractive index η_r shows a drastic change at the onset of the inter-band transitions[12], constant η_r is no longer a reasonable assumption and thus the Tauc plot is no longer a suitable method for band gap analysis.

Given the obstacles addressed above, a more reliable method for band gap analysis is in demand. The following section will focus on the development of the derivative method which takes the first order derivative of the measured transmittance with respect to the incident photon energy and determines the value of band gap from a resultant inflection point. The derivative analysis method is suggested to be a more appropriate procedure for phase segregated alloy and nanostructures who exhibit broadened absorption edges.

3.1.4 The development of the derivative method for an accurate determination of band gap energies in alloys

Start with the Ridley's model[13] of absorption coefficient α expressed as Equation 3.8, combine all the constant terms and rewrite it as

$$\alpha = C^* \frac{1}{E\eta_r}(E - E_g)^{1/2} \tag{3.12}$$

where C^* is a constant, E is the energy of incident light, and η_r is the energy dependent refractive index. According to Equation 3.6, the transmittance T can be expressed as

$$T = \mathrm{e}^{-C^* \frac{1}{E\eta_r}(E-E_g)^{1/2} \cdot t^{-1}} = \mathrm{e}^{-C^{**} \frac{1}{E\eta_r}(E-E_g)^{1/2}} \tag{3.13}$$

where the film's thickness t is involved in the constant C^{**}.

Next, the first order derivative of the transmittance T with respect to the energy of incident light E is performed:

$$\frac{dT}{dE} = -e^{-C^{**}(E)^{-1}\eta_r^{-1}\sqrt{(E-E_g)}} \cdot \frac{d}{dE}\left[C^{**}(E)^{-1}\eta_r^{-1}\sqrt{(E-E_g)}\right]$$

$$= -e^{-C^{**}(E)^{-1}\eta_r^{-1}\sqrt{(E-E_g)}} \cdot C^{**}\left\{-(E)^{-2}\eta_r^{-1}\sqrt{(E-E_g)} + (E)^{-1}\frac{d[\eta_r^{-1}\sqrt{(E-E_g)}]}{dE}\right\}$$

$$= -e^{-C^{**}(E)^{-1}\eta_r^{-1}\sqrt{(E-E_g)}} \cdot C^{**}\left[-(E)^{-2}\eta_r^{-1}\sqrt{(E-E_g)} + \frac{d\eta_r^{-1}}{dE}\frac{\sqrt{(E-E_g)}}{E} + \frac{1}{2\eta_r}\frac{1}{E\sqrt{(E-E_g)}}\right] \tag{3.14}$$

$$= -e^{-C^{**}(E)^{-1}\eta_r^{-1}\sqrt{(E-E_g)}} \cdot C^{**}\left[-(E)^{-2}\eta_r^{-1}\sqrt{(E-E_g)} - \frac{1}{\eta_r^2}\frac{d\eta_r}{d(E)}\frac{\sqrt{(E-E_g)}}{E} + \frac{1}{2\eta_r}\frac{1}{E\sqrt{(E-E_g)}}\right]$$

Or,

$$\frac{dT}{dE} = -C^{**}\exp\left[-C^{**}\frac{1}{E\,\eta_r}\sqrt{E-E_g}\right] \cdot\left[\frac{-1}{E^2\,\eta_r}\sqrt{E-E_g}-\frac{d\,\eta_r}{dE}\frac{\sqrt{E-E_g}}{E\,\eta_r^2}+\frac{1}{2\,\eta_r E\sqrt{E-E_g}}\right] \tag{3.15}$$

Assuming that $\frac{d\,\eta_r}{dE}$ is not badly behaved, which is a reasonable assumption[14], at the point where the energy of incident light *E* approaches that of the band gap, i.e. $E \to E_g$, Equation 3.15 yields

$$\lim_{E\to E_g}\frac{dT}{dE} = -1\,C^{**}\left(-0-0+\frac{1}{0}\right)\to -\infty \tag{3.16}$$

Which in practice will appear in the plot of $\frac{dT}{dE}$ versus *E* as a sharp inflection pointing at where the incident photon energy equals the material's band gap E_g.

This derivative method for extrapolating the value of band gap energy advances the conventional linear fitting analysis in one aspect that it is applicable to materials with or without well defined absorption edges, as shown in Figure 3.6. On the other hand, the energy dependent refractive index η_r plays no role in determining where the inflection point occurs. Thus no approximation of a constant η_r is needed.

The derivative analysis has been successfully performed previously for the studies of the band gaps in $In_xGa_{1-x}N$ semiconductor alloys[15–18]. However, to our knowledge no detailed derivation of this method has been reported at the time of this writing.

It is worth mentioning that both the conventional and the inflection point analysis discussed above are based on Equation 3.6, which neglected the reflecting effects occurring at both the air-film interface and the film-substrate interfaces, along with the multiple internal

reflection occurring within the film. However, when the reflection at all the interfaces are taken into consideration, $\left[\alpha^2(E)^2\right]$ is no longer directly proportional to $(E-E_g)$. Therefore the theoretical foundation of the conventional linear fitting analysis is no longer valid. However, the inflection point analysis retains its accuracy. The proof is presented in Appendix A.

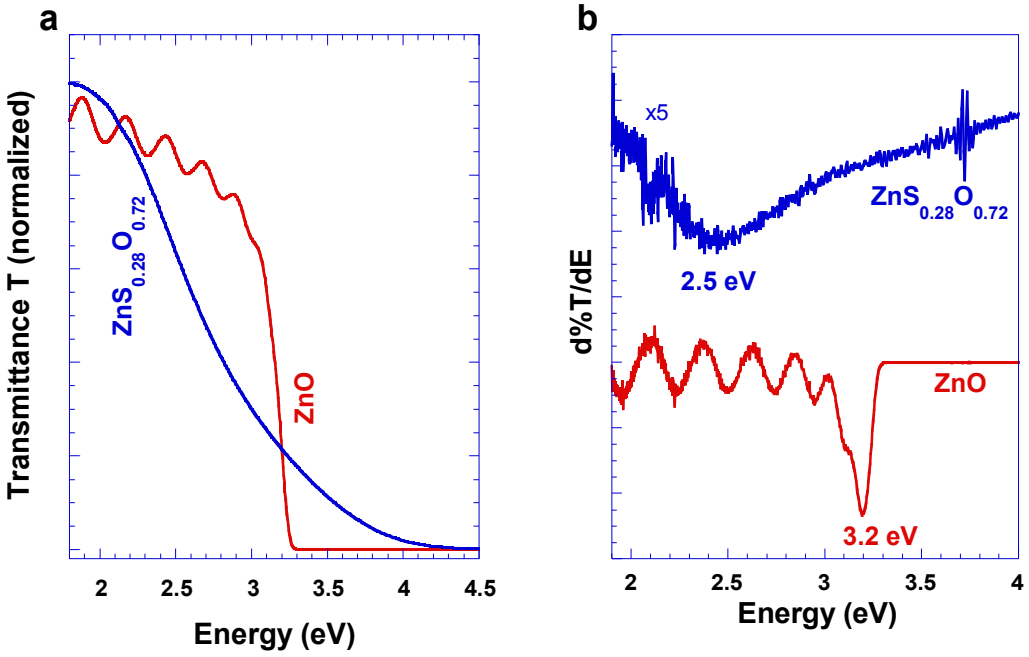

Figure 3.6: ***a)*** *The transmittance spectrum of ZnO exhibits a well defined absorption edge. While that of* $ZnS_{0.28}O_{0.72}$ *alloy shows a broadened absorption edge.* ***b)*** *The derivative analysis method was applied to the spectra of both materials and the values of the band gap energy can be determined unambiguously.*

3.2 Urbach energy: a measure of the extended electronic states in the band gap

Ideally, momentum-conserving transitions between parabolic electronic energy bands obeying the model described by Equation 3.8 predict a sharp absorption edge with no absorption occurring at phonon energies below E_g, which appears as an sharp edge at the band gap energy E_g in an absorption spectrum. In practice, however, the observed absorption edges of various semiconductor materials appear like a gentle slope extending exponentially into the energy region below E_g, as shown in Figure 3.7 by a comparison between the absorption coefficient α of a $Mg_{0.65}Zn_{0.35}O$ thin film and that of a ZnO single crystal. Such exponential absorption edge was first reported by Urbach in 1953[19] and was observed in heavily doped semiconductors, amorphous semiconductors, and semiconductor alloys[11,20–26].

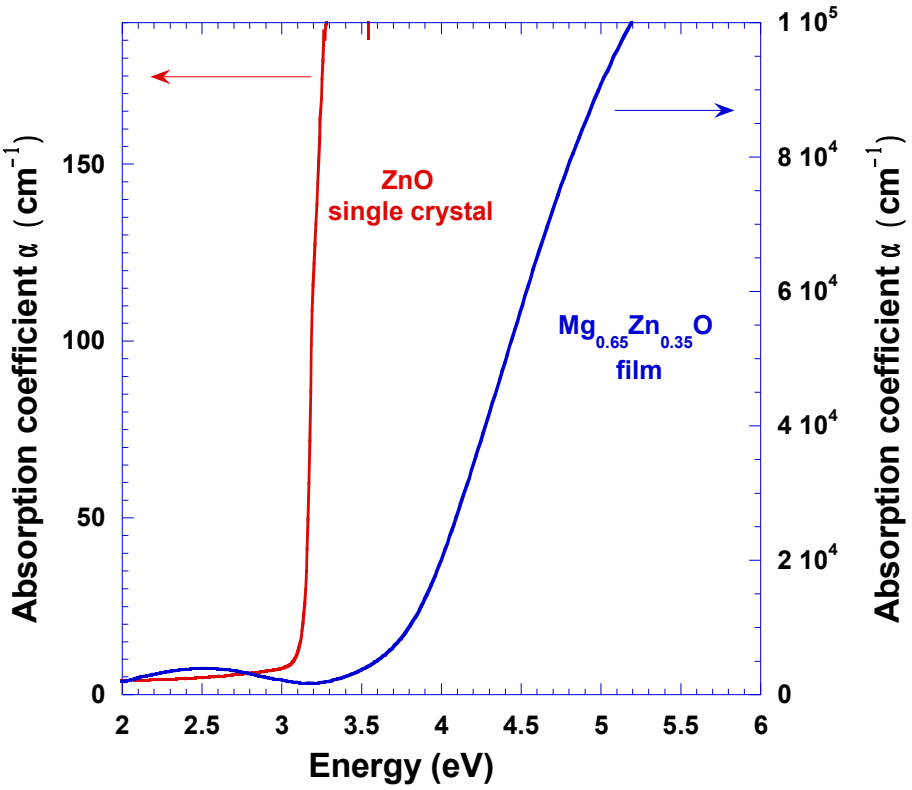

Figure 3.7: The absorption coefficient α of a $Mg_{0.65}Zn_{0.35}O$ thin film exhibits an exponential tail, comparing to the sharp absorption edge of the ZnO single crystal.

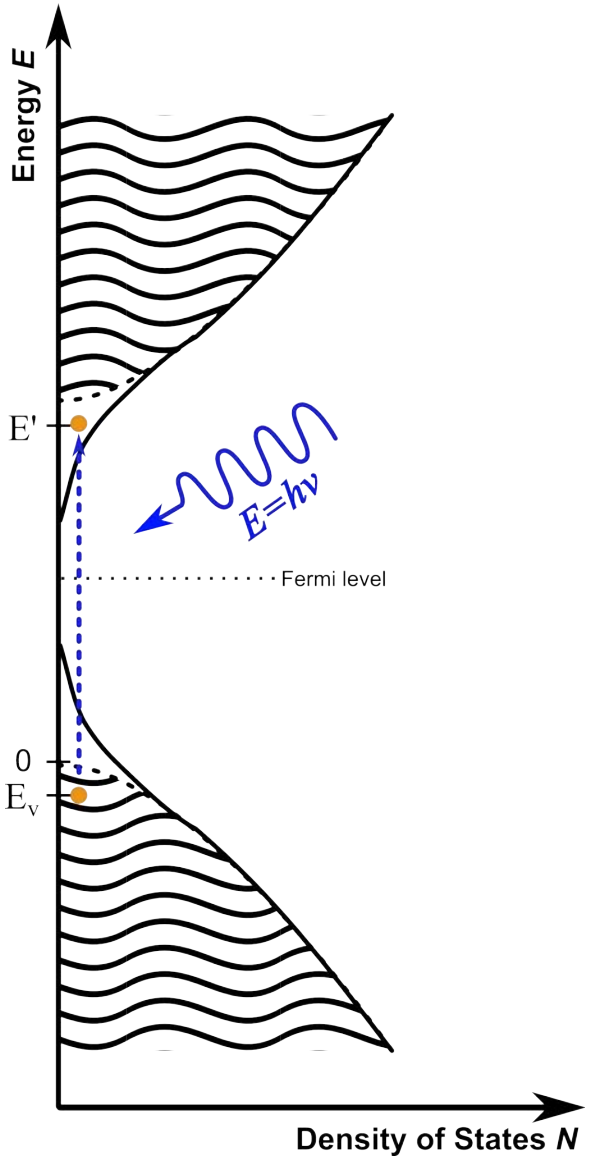

Figure 3.8: The electronic transitions involving "band tail" states in the band gap correspond to an absorption coefficient $\alpha \propto e^{E/E_u}$ *, where the parameter* E_u*, is known as Urbach energy, describes the exponential distribution of the localized states.*

Pankove[22] proposed the correlation between the exponential absorption edge and the exponential distribution of electronic energy states in the band gap. Consider electron transitions from energy E_v in the parabolic valence band to energy E' in the exponential tail of conduction band, as shown in Figure 3.8. The initial and final density of states is then given by $N_i \propto E_v^{1/2}$ and $N_f \propto e^{E'/E_u}$, respectively, where E_u is an empirical parameter describing the distribution of energy states. The absorption coefficient corresponds to this type of electronic transitions is proportional to the product of the densities of initial and final states integrated over all possible transitions for a given energy E:[22]

$$\alpha(E) = A \int_{\xi}^{E-\xi} (E_v)^{1/2} e^{E'/E_u} dE' \tag{3.17}$$

Where A is a constant and ξ is an infinitesimal amount of energy. Apply the constraint of energy conservation $E_v = E' - E$, and, making the following change of variable

$x = \frac{(E - E')}{E_u}$, Equation 3.17 can be written as[22]

$$\alpha(E) = A\ E_u^{2/3}\ e^{E/E_u} \int_{(E+\xi)/E_u}^{\xi/E_u} x^{1/2} e^{-x} dx \tag{3.18}$$

The integral part is independent of E since $E >> E_u$ [22] and therefore

$$\alpha(E) = C^* e^{E/E_u} \tag{3.19}$$

Or,

$$\ln \alpha(E) = C^{**} + \frac{E}{E_u} \tag{3.20}$$

Where C^* and C^{**} are constants. Hence, a plot of $\ln \alpha(E)$ versus E should yield a straight line in the energy region below band gap, where the sub-band absorptions occur[25]. The

reciprocal of the straight line's slope gives the value of E_u, as illustrated in Figure 3.9.

The parameter E_u is commonly addressed as Urbach Energy and is a measure of the localized electronic energy levels within the band gap. During the past several decades efforts have been made to study the exact cause of the Urbach tails in materials. Phonon interactions, defects and impurities, excitons and structural disorders in materials have been reported to be associated to the observed Urbach tails[6,8,27,28]. In this work exponential absorption tails have been observed in $Mg_xZn_{1-x}O$ films and Urbach energies E_u have been extrapolated in order to investigate the origin of the localized sub-band gap states.

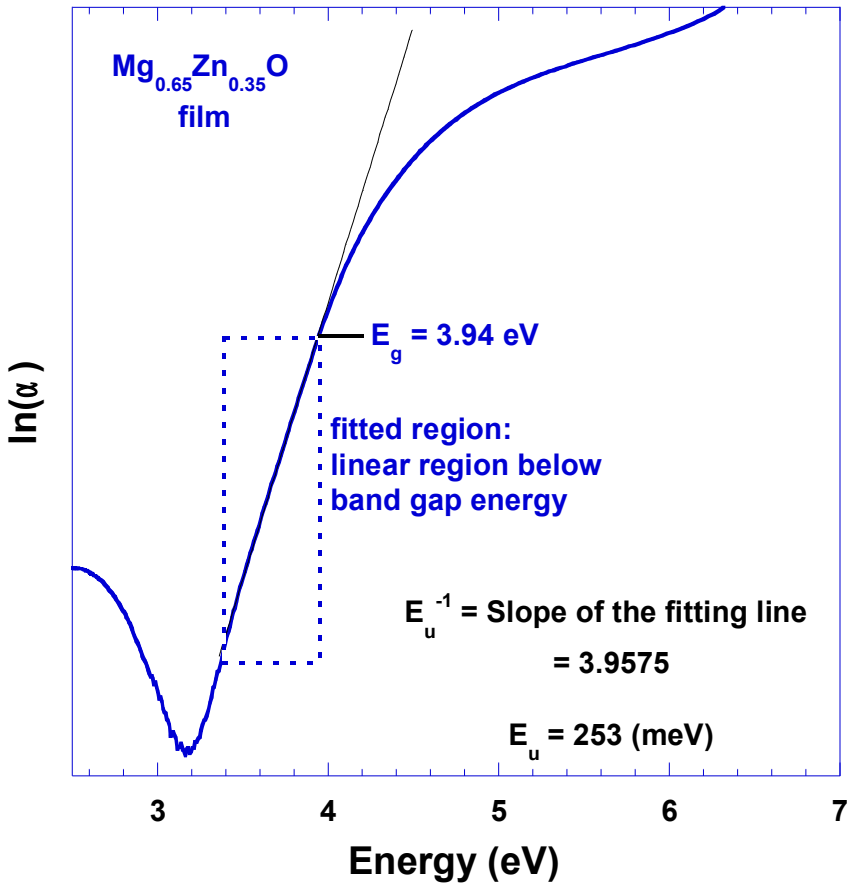

Figure 3.9: An example of extrapolating the value of Urbach energy E_u of the $Mg_{0.65}Zn_{0.35}O$ alloy from its transmittance spectrum. The vertical axis is the logarithm of the absorption coefficient and the horizontal axis is the incident photon energy. Fitting for the linear region just below band gap energy, where the electronic transition involving the tail states occurs, gives E_u as the reciprocal of the slope of the fitting line.

3.3 Calculating the thickness of films via interference patterns

When incident light travels through a film at a speed *V*, reflections occur on both the air-film and the film-substrate interfaces. According to Equation 3.4, as the light wave of frequency ν is getting internally reflected in a film with a refractive index $\eta_r = n - i\kappa$ and a thickness *t*, the wave will exit the film multiple times with a change to the incident phase angle of Δθ, 3Δθ, 5Δθ, etc., where

$$\Delta\theta = \theta_1 - \theta_0 = \theta(x=t) - \theta(x=0) = \frac{2\pi\nu nt}{V} \tag{3.21}$$

As illustrated in Figure 3.10.

The change in the phase angle will cause interference between different orders of the transmitted light wave. Let us consider the first and second order of the transmitted light whose intensities are higher than following orders. The interference between the two light waves yields a resultant intensity of[1]

$$I = I_1 + I_2 + 2\sqrt{I_1 I_2}\cos\delta \tag{3.22}$$

where I_1 and I_2 is the intensity of the first and the second order transmitted light, respectively. δ is the phase difference between the two waves. In this case,

$$\delta = \theta_2 - \theta_1 = 2\Delta\theta = \frac{4\pi\nu nt}{V} \tag{3.23}$$

It can be concluded from Equation 3.22 and Equation 3.23 that certain frequencies will cause constructive or destructive interferences between the two orders of transmitted light, which will result in a sinusoidal pattern in the transmittance spectrum of the film of study, as shown earlier in Figure 3.2.

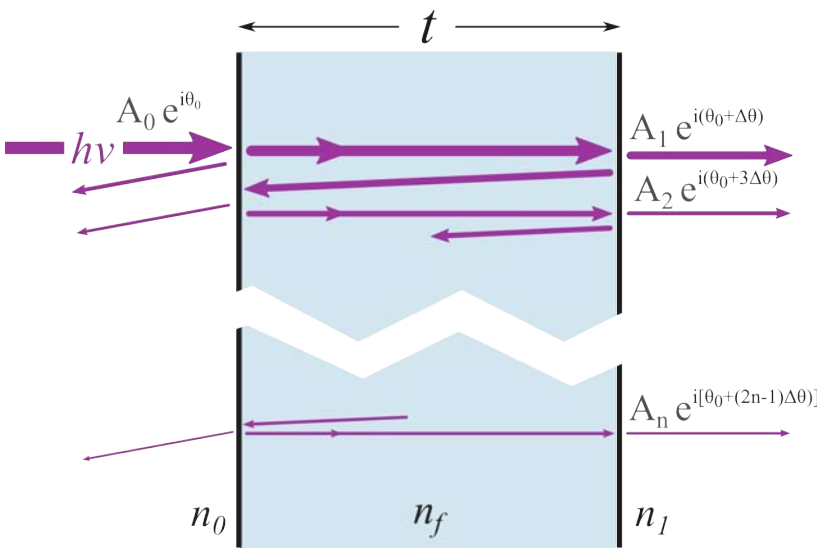

Figure 3.10: When incident light travels through a film, reflections occur on the two interfaces and multiple internal reflections occur within the film. The change in the phase angle each time the light wave propagates in the film will cause constructive and destructive interference between different orders of transmitted light wave when certain conditions are met, resulting in interference fringes in the transmittance spectrum.

Based on the interference fringes shown in the transmittance spectrum, a film's thickness can be calculated following the method proposed by Manifacier et al[29].

In the example transmittance spectrum shown in Figure 3.11, consider the upper and lower envelopes enclosing the maximum points and the minimum points of the sinusoidal wave of interference pattern as two functions with respect to the wavelength λ: $T_{max}(\lambda)$ and $T_{min}(\lambda)$, respectively. Expressions of these functions can be obtained via polynomial fitting for a high accuracy.

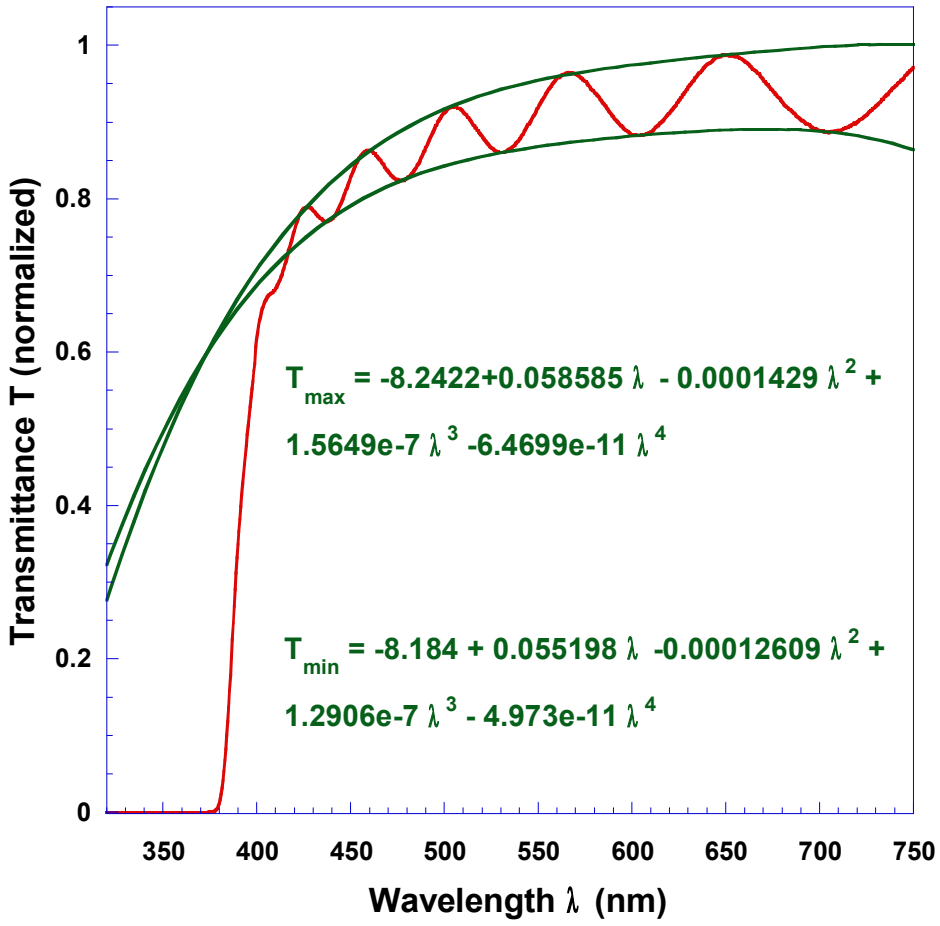

Figure 3.11: The transmittance spectrum of a ZnO film. Maximum and Minimum points of interference pattern appearing at the high transmittance region were fitted to obtain envelope functions $T_{max}(\lambda)$ and $T_{min}(\lambda)$, respectively.

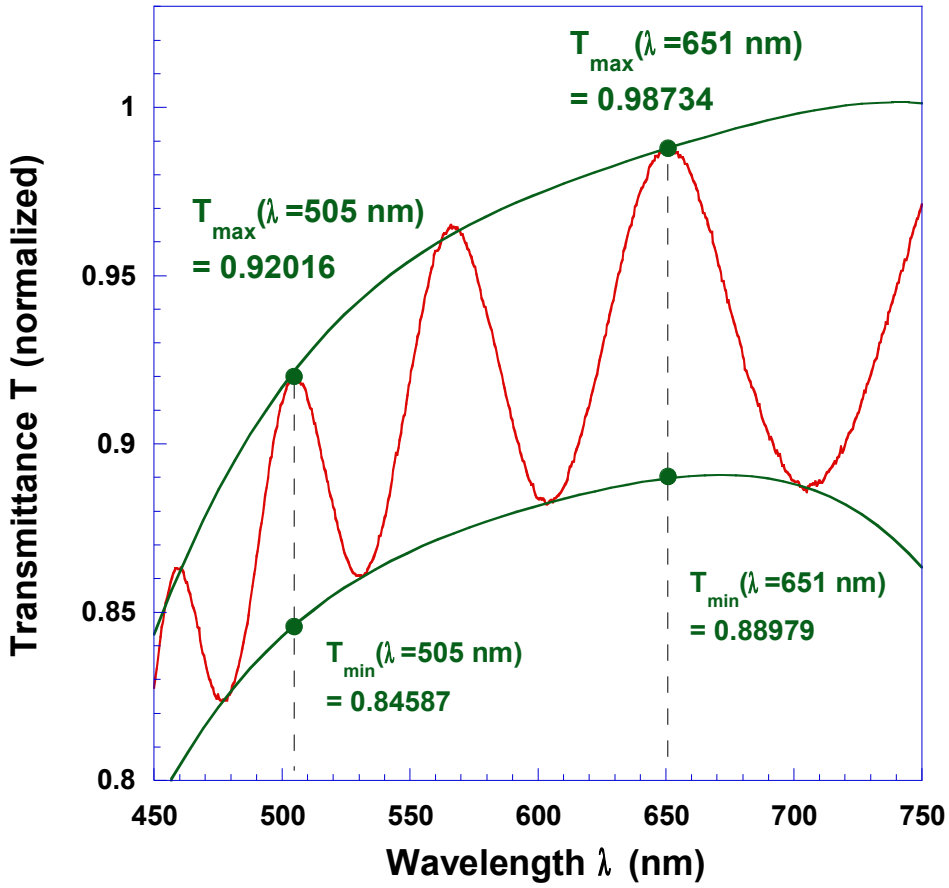

Figure 3.12: Two maximum points at λ=505 nm and λ=651 nm on the interference pattern were chosen. The functions of T_{min} and T_{max} at various wavelengths were calculated from the fitted functions obtained previously in Figure 3.11 for further calculations.

Choose two wavelength values which both yield maxima (or minima) in the interference region of the transmittance spectrum. As shown in Figure 3.12, λ_1=505 nm and λ_2=651 nm, which both correspond to maximum points, were chosen for the following calculation.

Next, calculate the real part of the refractive index $n(\lambda)$ at the two chosen wavelengths, respectively, following equation[29]

$$n(\lambda)=\left[N+\left(N^2-n_0^2\cdot n_1^2\right)^{\frac{1}{2}}\right]^{\frac{1}{2}} \tag{3.24}$$

where

$$N(\lambda)=\frac{n_0^2+n_1^2}{2}+2n_0n_1\frac{T_{max}(\lambda)-T_{min}(\lambda)}{T_{max}(\lambda)\cdot T_{min}(\lambda)} \tag{3.25}$$

n_0 and n_1 are the real part of the refractive indices of the media before and beyond the thin film, respectively. Under double beam configuration with background correction as done in this work, both media can be considered as air and thus $n_0=n_1=1$. In the example shown here,

$$\begin{aligned} N\left(\lambda_1=505\,nm\right)&=\frac{n_0^2+n_1^2}{2}+2n_0n_1\frac{T_{max}-T_{min}}{T_{max}T_{min}}\\ &=\frac{1+1}{2}+2\times\frac{0.92016-0.84587}{0.92016\times0.84587}\\ &=1.190894 \end{aligned} \tag{3.26}$$

Therefore,

$$\begin{aligned} n\left(\lambda_1=505\,nm\right)&=\left[N\left(\lambda_1=505\,nm\right)+\left(N\left(\lambda_1=505\,nm\right)^2-n_0^2n_1^2\right)^{1/2}\right]^{1/2}\\ &=1.355582 \end{aligned} \tag{3.27}$$

Similarly, at the wavelength of 651 nm,

$$N\left(\lambda_2 = 651\,nm\right) = 1.222077 \tag{3.28}$$

And

$$n\left(\lambda_2 = 651\,nm\right) = 1.387282 \tag{3.29}$$

Then the thickness *t* of the film can be calculated following the equation[29]

$$t = \frac{M\,\lambda_1\lambda_2}{2\left(n\left(\lambda_1\right)\cdot\lambda_2 - n\left(\lambda_2\right)\cdot\lambda_1\right)} \tag{3.30}$$

Where M is the number of oscillations in the interference pattern between the two extrema (M= 2 in this case). For the ZnO film examined in this example, a thickness of

$$\begin{aligned} t &= \frac{M\,\lambda_1\lambda_2}{2\left(n\left(\lambda_1\right)\cdot\lambda_2 - n\left(\lambda_2\right)\cdot\lambda_1\right)} \\ &= \frac{2\times 505\,nm\times 651\,nm}{2\left(1.355582\times 651\,nm - 1.387282\times 505\,nm\right)} \\ &= 1807.279\,nm \;\approx 1.807\,\mu m \end{aligned} \tag{3.31}$$

was obtained.

For better results, enough fringes should be seen in a transmittance spectrum in order to guarantee the accuracy of the fitted wave envelope functions $T_{min}(\lambda)$ and $T_{max}(\lambda)$. Also the data interval during the transmittance acquisition should be small enough to allow the extreme points to be unambiguously identified. Overall, the interference pattern appeared in the high transmittance region of dielectric thin films are proved to be a useful tool for research, process and quality control applications.

3.4 Conclusion

When applied to semiconductor materials, optical transmission spectroscopy is an information-dense analysis technique. Various material properties can be unraveled following proper data analysis methods.

In this chapter the derivative method for the band gap analysis of semiconductor materials was derived from the mathematical model of the optical absorption processes and was proved to yield more accurate results than the conventional linear fitting analysis method.

Transmittance spectra of semiconductor alloys exhibit broadened absorption edges which contain information about electron states within the band gap and can be quantified as a parameter known as Urbach energy. The interference fringes observed in transmittance spectra can be employed to calculate the thickness of a film.

3.5 References

1. Hecht, E. *Optics*. (Addison-Wesley, 2002).

2. Pankove, J. I. *Optical Processes in Semiconductors*. (Courier Dover Publications, 2012).

3. Tan, S. T. *et al.* Properties of polycrystalline ZnO thin films by metal organic chemical vapor deposition. *J. Cryst. Growth* **281,** 571–576 (2005).

4. Ridley, B. K. *Quantum Processes in Semiconductors*. (Oxford University Press, 2013).

5. Butcher, K. S. A., Wintrebert-Fouquet, M., Chen, P. P.-T., Timmers, H. & Shrestha, S. K. Detailed analysis of absorption data for indium nitride. *Mater. Sci. Semicond. Process.* **6,** 351–354 (2003).

6. Teng, C. W. *et al.* Refractive indices and absorption coefficients of $Mg_xZn_{1-x}O$ alloys. *Appl. Phys. Lett.* **76,** 979–981 (2000).

7. Tauc, J. *Amorphous and liquid semiconductors*. (Plenum, 1974).

8. Tan, S. T. *et al.* Blueshift of optical band gap in ZnO thin films grown by metal-organic chemical-vapor deposition. *J. Appl. Phys.* **98,** 013505 (2005).

9. Srikant, V. & Clarke, D. R. Optical absorption edge of ZnO thin films: The effect of substrate. *J. Appl. Phys.* **81,** 6357–6364 (1997).

10. Lee, B.-S. *et al.* Investigation of the optical and electronic properties of $Ge_2Sb_2Te_5$ phase change material in its amorphous, cubic, and hexagonal phases. *J. Appl. Phys.* **97,** 093509 (2005).

11. Wei, W., Jin, C., Narayan, J. & Narayan, R. J. Optical and electrical properties of

gallium-doped $Mg_xZn_{1-x}O$. *J. Appl. Phys.* **107,** 013510 (2010).

12. Bahl, S. K. & Chopra, K. L. Amorphous Versus Crystalline GeTe Films. II. Optical Properties. *J. Appl. Phys.* **40,** 4940–4947 (2003).

13. Ridley, B. K. *Quantum Processes in Semiconductors*. (OUP Oxford, 1999).

14. Stern, F. Dispersion of the Index of Refraction Near the Absorption Edge of Semiconductors. *Phys Rev Phys. Rev.* **133,** A1653–A1664 (1964).

15. Wang, M. *et al.* Optical and structural properties of solgel prepared MgZnO alloy thin films. *THIN SOLID FILMS* **516,** 1124–1129 (2008).

16. Viswanatha R, C. S., Basu S, Sarma DD. Blue-emitting copper-doped zinc oxide nanocrystals. *J. Phys. Chem. B* **110,** 22310–2 (2006).

17. Parker, C. A. *et al.* Optical band gap dependence on composition and thickness of $In_xGa_{1-x}N$ (0. *Appl. Phys. Lett.* **75,** 2566–2568 (1999).

18. Ullrich, B., Zhang, C., Schubert, E. F., Cunningham, J. E. & Klitzing, K. v. Transmission spectroscopy on sawtooth-doping superlattices. *Phys. Rev. B* **39,** 3776–3779 (1989).

19. Urbach, F. The Long-Wavelength Edge of Photographic Sensitivity and of the Electronic Absorption of Solids. *Phys. Rev.* **92,** 1324–1324 (1953).

20. Rai, R. C. Analysis of the Urbach tails in absorption spectra of undoped ZnO thin films. *J. Appl. Phys.* **113,** 153508–153508–5 (2013).

21. Shen, W. Z. *et al.* Bandtail characteristics in InN thin films. *Appl. Phys. Lett.* **80,** 2063–2065 (2002).

22. Pankove, J. I. Absorption Edge of Impure Gallium Arsenide. *Phys. Rev.* **140,** A2059–A2065 (1965).

23. Meeder, A. *et al.* Direct measurement of Urbach tail and gap state absorption in $CuGaSe_2$ thin films by photothermal deflection spectroscopy and the constant photocurrent method. *J. Appl. Phys.* **92,** 3016–3020 (2002).

24. Zanatta, A. R., Mulato, M. & Chambouleyron, I. Exponential absorption edge and disorder in Column IV amorphous semiconductors. *J. Appl. Phys.* **84,** 5184–5190 (1998).

25. Wood, D. L. & Tauc, J. Weak Absorption Tails in Amorphous Semiconductors. *Phys. Rev. B* **5,** 3144–3151 (1972).

26. Fanchini, G. & Tagliaferro, A. A new interpretation of the Urbach energy in amorphous carbon films. *Diam. Relat. Mater.* **13,** 1402–1407 (2004).

27. Hvedstrup Jensen, G. & Skettrup, T. Absorption edge and urbach's rule in ZnO. *Phys. Status Solidi B* **60,** 169–173 (1973).

28. Srikant, V. & Clarke, D. R. On the optical band gap of zinc oxide. *J. Appl. Phys.* **83,** 5447–5451 (1998).

29. Manifacier, J. C., Gasiot, J. & Fillard, J. P. A simple method for the determination of the optical constants n, k and the thickness of a weakly absorbing thin film. *J. Phys. [E]* **9,** 1002 (1976).

Chapter 4 Optical studies of alloy inhomogeneities in $Mg_xZn_{1-x}O$ films

4.1 Overview

As introduced in Chapter 1, the band gap of ZnO can be tuned by alloying MgO with ZnO. ZnO has a band gap of 3.2 eV while the band gap of MgO is 7.8 eV. Due to the small mismatch of the covalent radius and of the electronegativity between Zn and Mg (see Table 4.1 (b)), the band gap of $Mg_xZn_{1-x}O$ is expected to increase from 3.2 eV to higher values with respect to an increasing Mg composition *x*. Such expansion of the band gap of ZnO into deep UV region paves its way for applications in UV light emitting[1,2] and metal-insulator-semiconductor (MIS) based photodetectors[3–5].

Compound	Structure	Lattice Constants[76] (Å)	Band Gap (eV)
MgO	Rocksalt cubic	a=4.2	7.8 [78]
ZnO	Hexagonal Wurtzite	a=3.2 c=5.2	3.2 [76]

(a)

Atom	Covalence Radius[77] (Å)	Electronegativity[77] (Pauling's)	Oxidation States[77]
Mg	1.36	1.31	+2
Zn	1.25	1.65	+2
O	0.73	3.44	-2, -1

(b)

Table 4.1: Selective material properties of ***a)*** *ZnO and MgO;* ***b)*** *Zn, Mg, and, O.*

However, due to the differences in the crystal structures and the lattice constants as listed in Table 4.1 (a), the $Mg_xZn_{1-x}O$ alloy system has solubility issues. The phase diagram of ZnO-MgO in Figure 4.1 predicts that the thermodynamic solid solubility of MgO in ZnO is less than 4 at.%.[6] Yet growth methods with a thermodynamically non-equilibrium condition made the synthesis of $Mg_xZn_{1-x}O$ with higher solubility limits possible. Ohtomo et al., who pioneered the research of $Mg_xZn_{1-x}O$ demonstrated the first synthesis of high-quality

$Mg_xZn_{1-x}O$ thin films via pulsed laser deposition (PLD) with Mg compositions up to x=0.36 while maintaining the wurtzite structure[7,8]. Hexagonal $Mg_xZn_{1-x}O$ thin film up to x=0.49 have also been achieved via Molecular beam epitaxy (MBE), metal organic vapor-phase epitaxy (MOVPE) and magnetron sputtering growth[9–12]. On the other hand, the phase diagram predicts that the solubility of ZnO in cubic MgO lattices has a higher limit of x=0.55. The growth of cubic $Mg_xZn_{1-x}O$ via PLD has been achieved with Mg compositions from x=0.50 to 1[13–15]. Between the well defined wurtizte and cubic regions is a mixed phase region where both the wurtzite and cubic phases could exist simultaneously and numerous effects could occur.

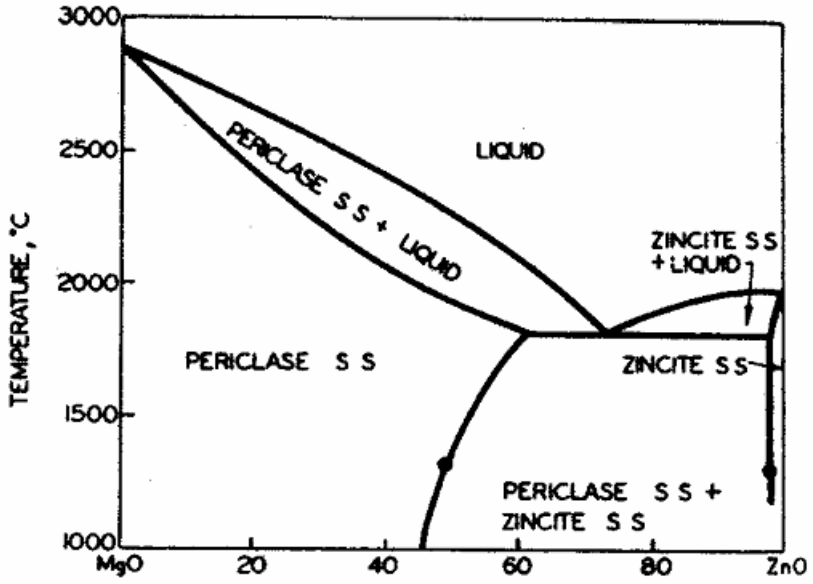

Figure 4.1: Phase diagram of a ZnO-MgO alloy system provided by Segnit et al.[6]. Under thermodynamic equilibrium conditions the alloy of Mg composition x=0 to ~0.04 exhibits purely wurtzite crystal structure while for Mg composition x ranging from ~0.55 to 1 it exhibits purely rocksalt-cubic structure. At intermediate Mg composition range of ~0.04<x<~0.55 a mixed phase exists.

For ternary semiconductor materials, the compositional and structural inhomogeneity has

a great impact on their optical properties and thus has an influence on the potential device performance. A profound investigation into the inhomogeneity is important for improving material qualities toward the realization of viable devices.

4.2 The synthesis of $Mg_xZn_{1-x}O$ thin films

The $Mg_xZn_{1-x}O$ thin films studied in this work were grown on (111) CaF_2 substrates and (001) α-quartz (SiO_2) substrates via reactive DC magnetron sputtering described in Chapter 2. The base pressure of the growth chamber was 10^{-6} Torr. Metal sputtering targets of mixed Mg-Zn with desired compositional ratios were custom made in our material synthesis laboratory. The films were grown in an Ar-O_2 environment at a pressure of 11 mTorr and the sputtering power delivered to the target was at 30 W. The sputtering duration was typically 2 hours and the substrate temperature was held at 250 ^oC throughout the growth.

CaF_2 and quartz were chosen as substrate materials because their wide band gap of ~12 eV[16] and ~9.3 eV[17], respectively, which allows for high transparency in the wavelength range from 190 nm to 800 nm (6.5 eV to 1.5 eV) as presented in Figure 4.2. Therefore the optical properties of the $Mg_xZn_{1-x}O$ films will not be concealed by substrates. It has been reported that the choice of substrate is crucial to the film qualities in epitaxial growth processes[18,19]. However, for the films grown in this work no substrate related effects were observed, as expected for films with micro-grain morphologies.

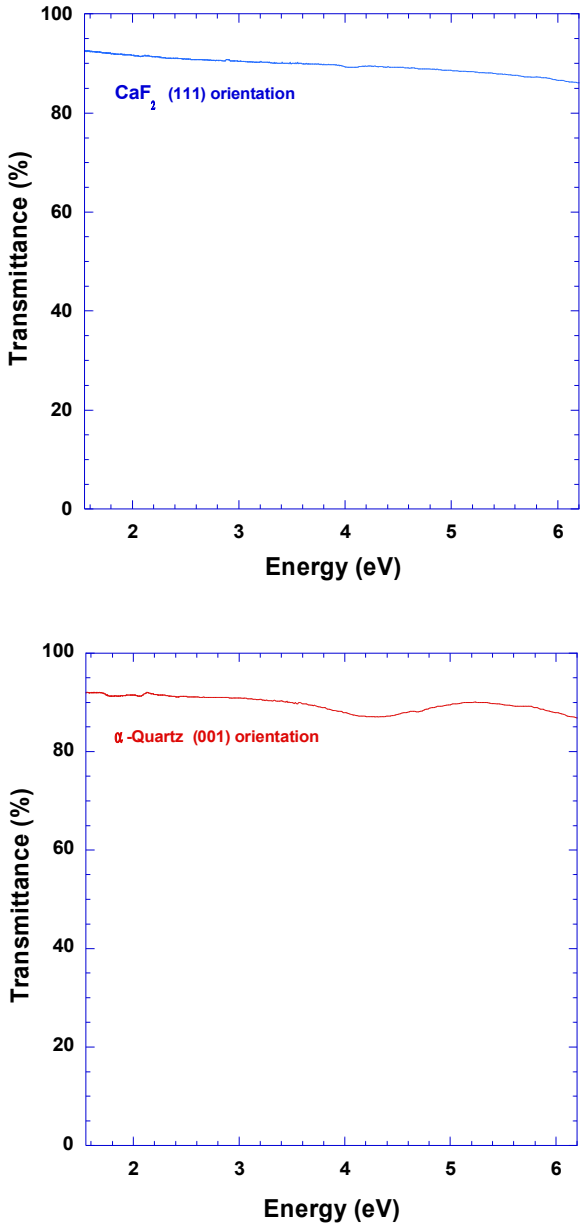

*Figure 4.2: The transmission spectra of **a)** CaF_2 (111) and **b)** α-quartz (001) slides. Both materials show high transparency to light expanding a wide range and will not block the optical feature of the ZnO based alloys. Thus they serve as good substrates for the growth of $Mg_xZn_{1-x}O$ films in this study.*

The thicknesses of the $Mg_xZn_{1-x}O$ films were calculated from the interference patterns observed in transmittance spectra, as outlined in Chapter 3. The films were found to have an average thickness of 400 nm. The elemental compositions were determined by energy dispersive X-ray spectroscopy (EDS). EDS indicated that in this work $Mg_xZn_{1-x}O$ thin films with Mg composition $0 \leq x \leq 0.78$ were achieved.

Figure 4.3 shows representative SEM images of the $Mg_xZn_{1-x}O$ thin films with a Mg composition $x = 0$, 0.16, 0.30, and, 0.49. The films were found to have polycrystalline morphologies. The SEM image of the ZnO film in Figure 4.3 (a) exhibits hexagonal needle structured grains. While the image of the film with $x=0.49$ in Figure 4.3 (d) has grains with less defined structures. As can be seen from the images in Figure 4.3 (a) to (d), the grain size of the films decreased with respect to the increasing Mg composition. This change in morphology suggests that the degree of crystallinity of the films decreased by the incorporation of Mg, and is consistent with the finding for $Mg_xZn_{1-x}O$ films grown by spray pyrolysis[20,21] and by magnetron sputtering[22]. Such phenomena may be attributed to solid solution impurity drag[23], in which MgO, when present in the solid solution, has an effect of decreasing the overall rate of boundary migration in ZnO. Similar behavior of MgO was reported in studies of the grain growth in Al_2O_3 ceramic material with MgO as a solute[24].

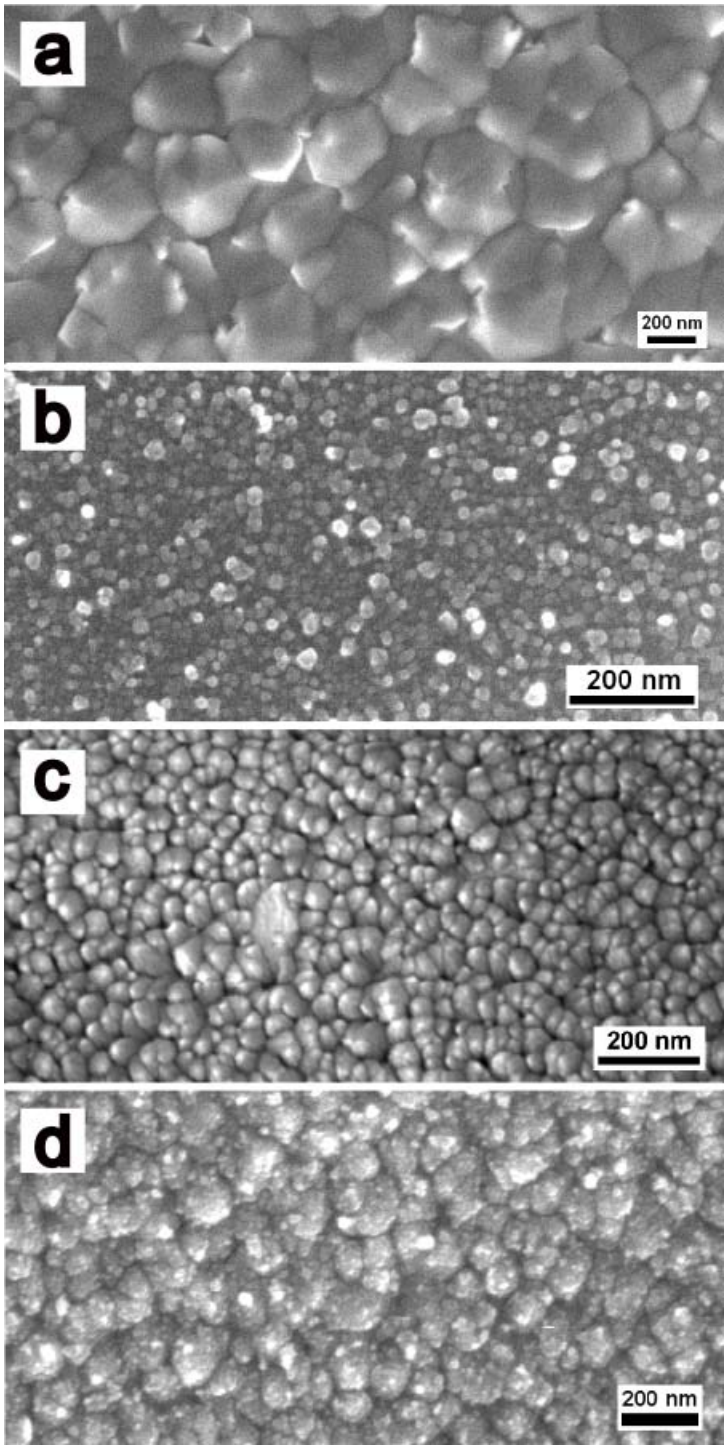

*Figure 4.3: SEM images of $Mg_xZn_{1-x}O$ films of **a)** x=0, **b)** x=0.16, **c)** 0.30, and, **d)** x=0.49 grown via magnetron sputtering for this work. The grain size of the films decreased with the increasing of Mg composition, indicating a decrease in the degree of crystallinity, which may be attributed to the impurity drag effect of MgO in the solid solution of MgO-ZnO.*

In order to identify the crystal structure and quality of the $Mg_xZn_{1-x}O$ films, X-ray diffraction (XRD) was performed for two different acquisition times of 2 hours and 14 hours and representative spectra were shown in Figure 4.4.

The XRD spectra with a 2-hour acquisition time suggested that $Mg_xZn_{1-x}O$ films with Mg composition from x=0 to x=0.65 all have diffraction patterns corresponding to the wurtzite structure. The diffraction peak of the film with x=0 appears at 33.75º, which registers closely with the reference peak of wurtzite (002) phase of ZnO at 34º. Films with x=0.49 and 0.65 show diffraction peaks which register with the same phase but with a slight shift toward higher angles, which is consistent with what was observed in $Mg_xZn_{1-x}O$ alloys in various crystal forms including nanocrystallites and thin films[25,26]. This shift in the (002) diffraction peak suggests a decreasing length in c axis of the wurtzite lattice, and a decreasing in atomic planar spacing due to strains in the films[27]. The peak is weakened and broadened as the Mg composition increases, indicating a decreasing in the crystal quality and grain size, which is in agreement with the observation in the SEM images. When the Mg composition reaches x=0.68 and x=0.78, the $Mg_xZn_{1-x}O$ films show diffraction peaks at 43.9º and 43.7º, respectively, which correspond to the peak of rocksalt cubic (200) phase at 43º. XRD spectra with a long data acquisition time of 14 hours were obtained from the films of x=0.65 and x=0.68. The film of x=0.65 has an additional diffraction peak corresponding to the cubic phase, and the film of x=0.68 has an additional weak peak corresponding to the wurtzite phase. This indicates a phase segregation in the $Mg_xZn_{1-x}O$ films, where two or more different crystal structures coexist. Further investigation into such structural inhomogeneity in $Mg_xZn_{1-x}O$ alloys will be discussed in later this chapter.

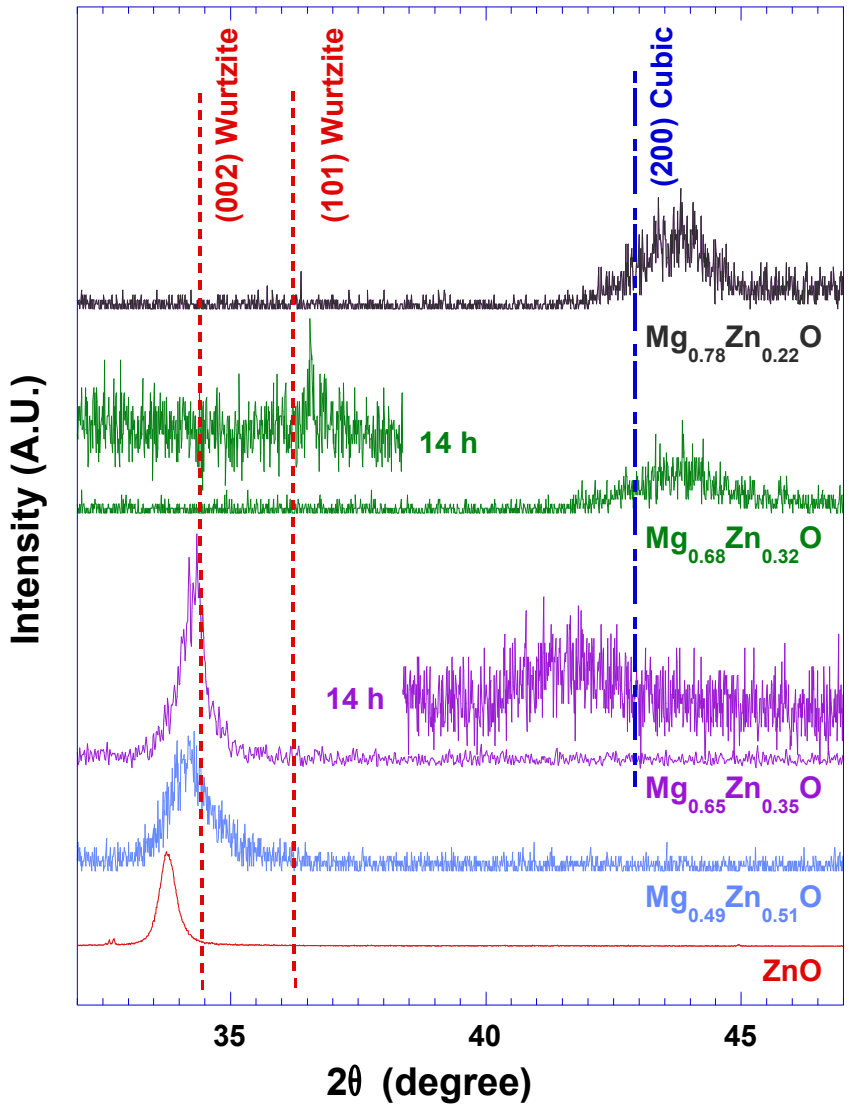

Figure 4.4: XRD spectra of $Mg_xZn_{1-x}O$ films with x=0, 0.49, 0.65, 0.68, 0.78. The XRD for a data acquisition time of 2 h indicate that at up to Mg composition x=0.65 the films are of the wurtzite structure, while those of x=0.68 and x=0.78 correspond to the cubic rocksalt structure. For a data acquisition time of 14 h, the XRD indicates that the film of x=0.65 has an additional diffraction peak corresponding to the cubic phase, and the film of x=0.68 has an additional weak peak corresponding to the wurtzite phase.

4.3 Optical band gap and band tailing analysis of $Mg_xZn_{1-x}O$ thin films via transmission spectroscopy

4.3.1 Optical band gap analysis

To investigate the optical properties of the $Mg_xZn_{1-x}O$ thin films, transmission spectroscopy was utilized and representative transmittance spectra were presented in Figure 4.5. As can be seen in Figure 4.5, the absorption edge occurs at higher energies as the Mg composition *x* increases. Figure 4.6 (a) presents the Tauc linear fitting analysis of the transmittance spectra, indicating that the band gap of the alloys expands from 3.23 eV to 5.92 eV as the Mg composition *x* increases from *x*=0 to 0.78. The Tauc analysis is a commonly used methods for analyzing band gap of semiconductors[28,29]. However, the previous studies had suggested that for materials yield relatively broad absorption edges, including alloys, phase segregated alloys, and, nanostructures, the derivative method is a more appropriate procedure[30–32]. The details in the development of this analytical method was discussed in Chapter 3. Figure 4.6 (b) presents the band gap values of the $Mg_xZn_{1-x}O$ alloys analyzed via the derivative method. The results in Figure 4.6 (a) and (b) indicate that for all but two samples, the *x*=0.61 and *x*=0.65, both methods are in good agreement. As will be discussed in the following sections, the alloys of *x*=0.61 and *x*=0.65 are among the alloys that were found via selective resonant Raman scattering to exhibit structural inhomogeneity. The development of the derivative method in Chapter 3 suggested that it is a more straightforward approach for determining the majority-phase band gap value of the alloys in this study.

In light of the above analysis, $Mg_xZn_{1-x}O$ alloys with band gaps ranging from 3.20 eV to 5.67 eV were achieved.

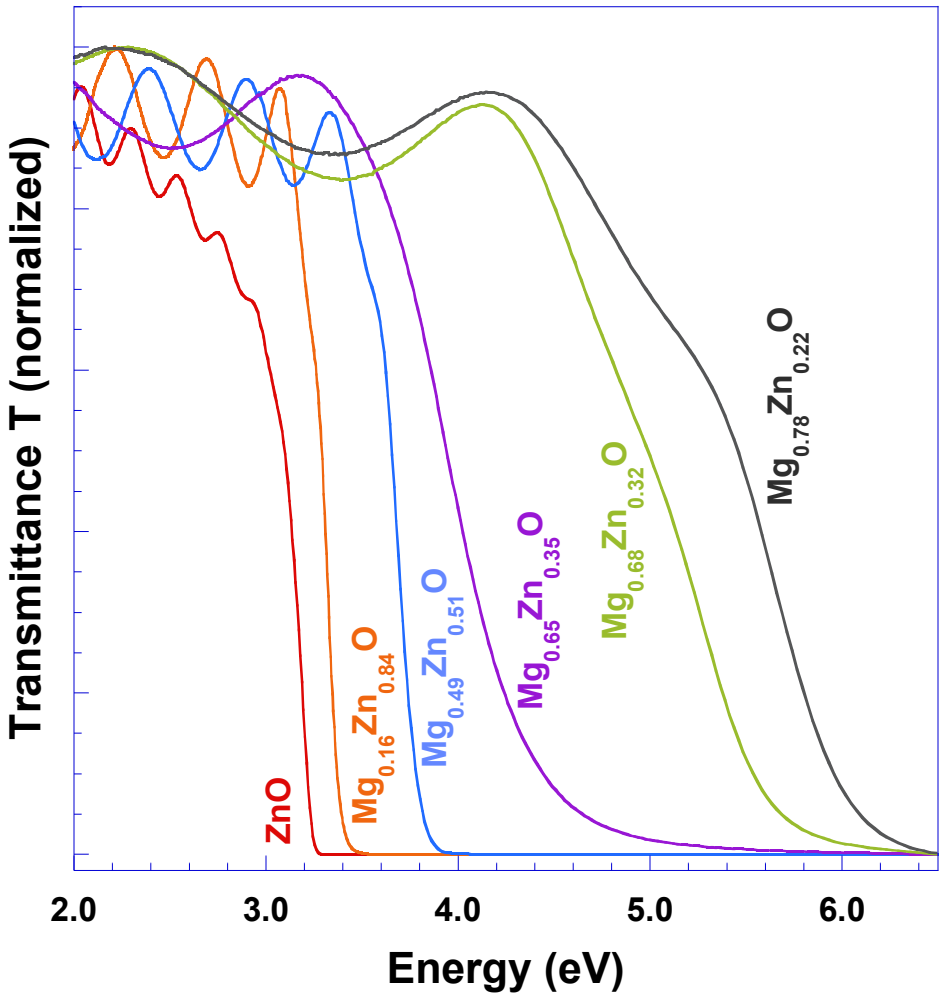

Figure 4.5: Representative transmission spectra of $Mg_xZn_{1-x}O$ thin films with x=0, 0.16, 0.49, 0.65, 0.68, and 0.78. The absorption edge shifts toward the higher energy end with respect to the increasing in Mg composition. For the films with x≥0.65, energy levels in between conduction and valence bands result in broadened absorption edges.

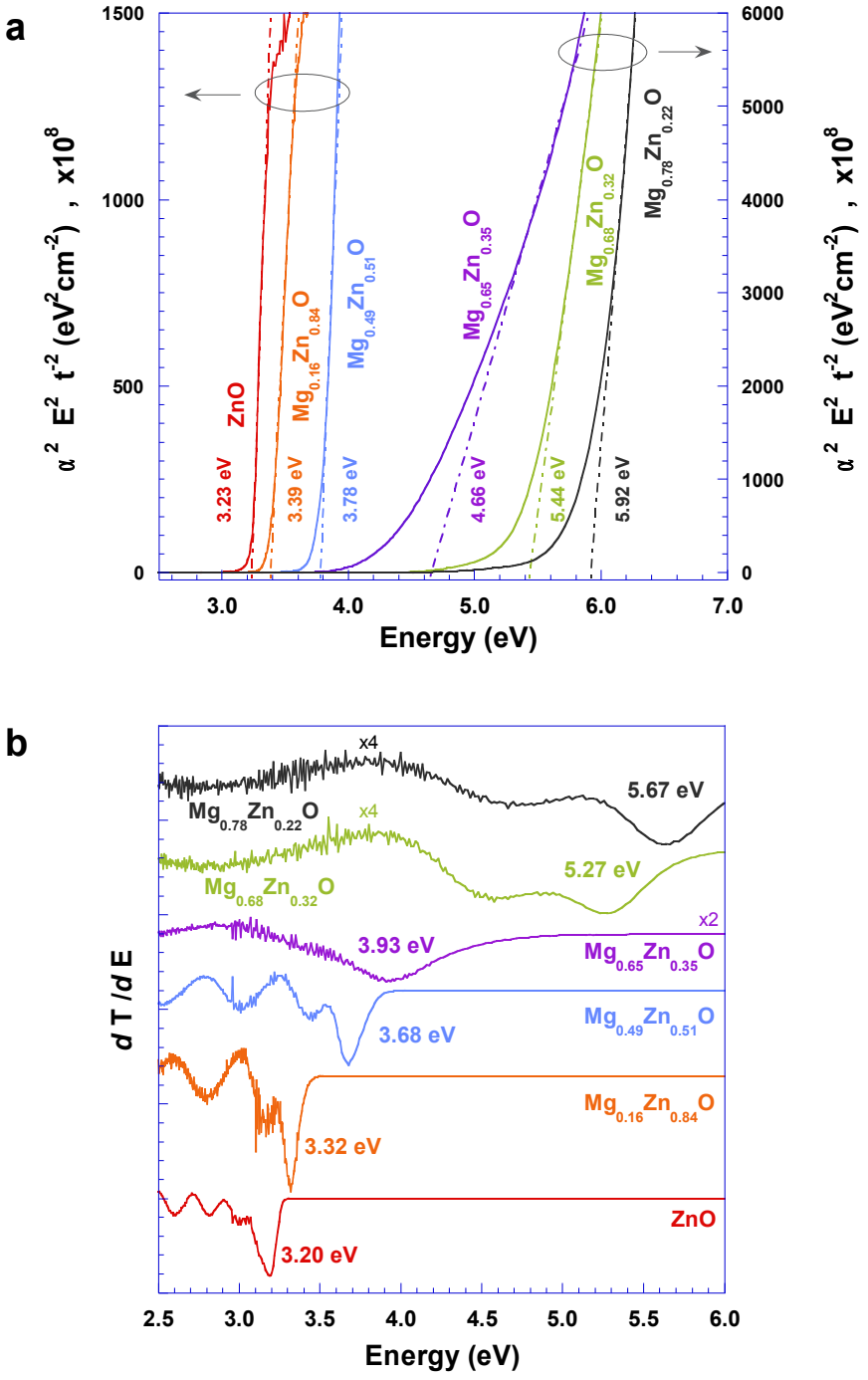

Figure 4.6: Representative spectra showing the bandgap of $Mg_xZn_{1-x}O$ films determined ***a)*** *via Tauc plot linear fitting analysis, and,* ***b)*** *via the derivative method analysis. The bandgaps are marked. The main minimum corresponds to the bandgap energy. The additional minima are the film interference patterns. The derivative analysis was proved to be a more appropriate method for obtaining majority-phase bandgap value of the alloys.*

4.3.2 Urbach energy analysis

As can be seen in Figure 4.5, the absorption edges of the $Mg_xZn_{1-x}O$ films appear broadened with respect to the increasing Mg composition. When investigating the behavior of the absorption coefficient α, an exponential "tail" can be observed in the energy region below the band gap, as shown earlier in Chapter 3, Section 3.2.

First reported in 1953[33], such exponential tail in absorption coefficient is known as *Urbach tail* which is caused by electronic transitions associated with localized electronic energy states extended into the band gap. The "steepness" of a Urbach tail can be quantified as Urbach energy (E_u) which gives a measure of the extent of the tail states distribution.

Urbach energies of the $Mg_xZn_{1-x}O$ grown for this study were extrapolated from their transmittance spectra following the procedures introduced in Section 3.2, Chapter 3. Representative extrapolation results are shown in Figure 4.7. As can be seen from the summary of the Urbach energy values in Figure 4.16. For Mg composition $x < 0.30$, E_u of $Mg_xZn_{1-x}O$ alloys remained below 100 meV with small variations. While for alloys of $0.30 \leq x \leq 0.78$, E_u increased from 98 meV to 435 meV and exhibited a strong compositional sensitive behavior.

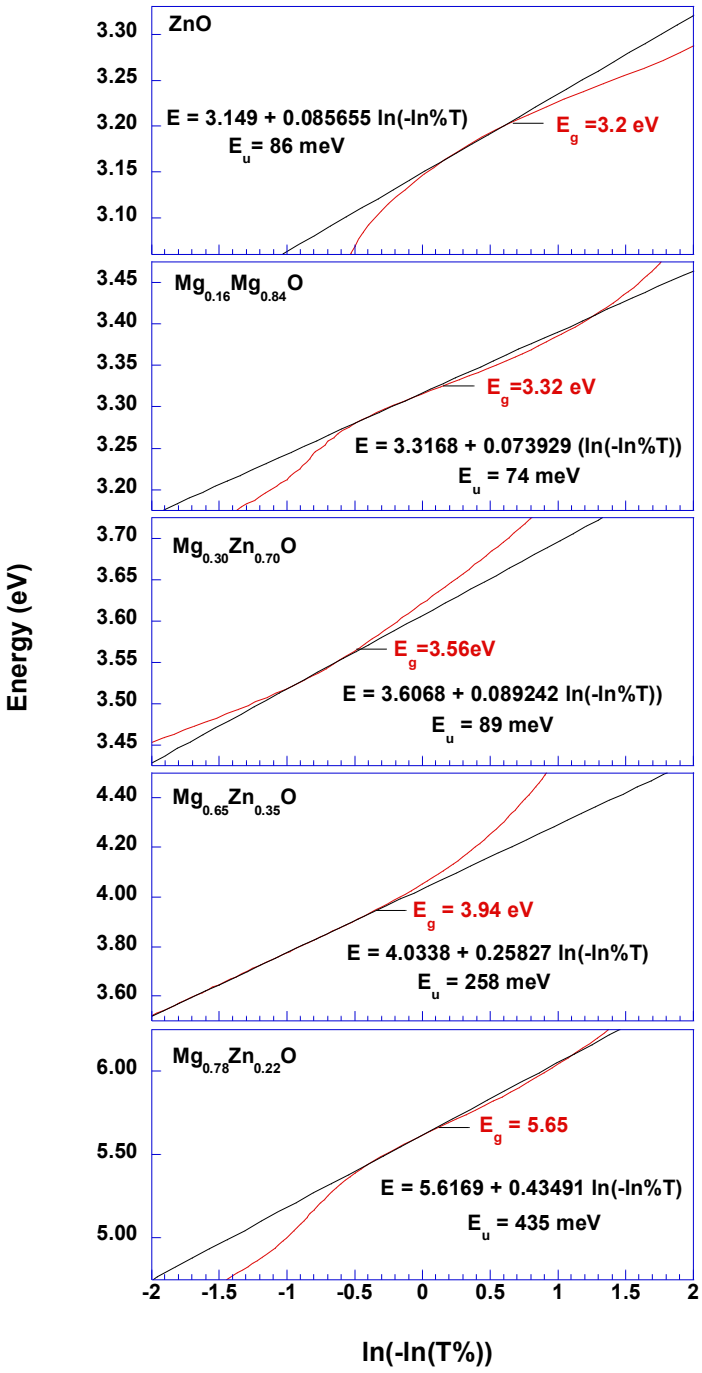

Figure 4.7: Representative plots presenting the extrapolation of Urbach energy E_u of $Mg_xZn_{1-x}O$ films from their transmittance spectra. The value of E_u increases with respect to the Mg composition x, indicating alloying induced localized electron energy states within the band gaps.

Urbach energy has two contributing effects: $E_u = X + Y(T)$,[34,35] where X is the static contribution and $Y(T)$ is a temperature dependent effect due to an increase of the internal electric fields induced by thermal vibration[28] and the thermal occupancy of phonon state[34–36]. Given that all transmission measurements in this study were conducted at room temperature, the thermal contribution is expected to be a systematic effect and thus not the dominant contribution to the alloy composition sensitive behavior of E_u in $Mg_xZn_{1-x}O$ alloys. Furthermore, the thermal effect was found to be negligible for $Mg_xZn_{1-x}O$ alloys grown by pulsed laser deposition[37].

The static contribution to E_u may be induced by several mechanisms. The ones which are relevant to the $Mg_xZn_{1-x}O$ alloy films grown for this study are listed as following:

(1) The granular morphologies in the $Mg_xZn_{1-x}O$ films introduce structural defects such as grain boundaries and dangling bonds. These defects induce distortion of the lattice periodicity, which can cause deformation of the energy band in a semiconductor[38,39], and thus result in electronic energy states in the band gap;

(2) Compositional fluctuations due to alloying can also result in an exponential tail of the respective density of states[40,41];

Further investigations into the extent of contributions from structural defects and from alloy compositional fluctuations will be discussed later in this Chapter.

4.4 The structural inhomogeneity in $Mg_xZn_{1-x}O$ alloys probed via selective resonant Raman scattering

As was discussed in Chapter 3, in Raman scattering when the laser excitation energy is in the vicinity of one of the energy absorption bands of the crystal (i.e. the band gap),

resonant multi-phonon scattering occurs, whose order depends on the strength of the electron-phonon interaction. Previous study of our group has found that in ZnO and $Mg_xZn_{1-x}O$ alloys the longitudinal optical (LO) phonon mode exhibits outgoing resonance up to the tenth order[42]. The resonant Raman scattering also gives high intensity which is usually many orders of magnitude greater than that of a non-resonant scattering event. Such intensity enhancement enables spectra to be obtained from material with low concentrations[43] and small sizes such as semiconductor single quantum dots and quantum wells with sizes of only a few nanometers[44,45]. For an alloy system with phase segregation properties, the domains of the segregated minority phase can be in a size regime too small to be detected by X-ray diffraction (XRD). However, with proper choices of excitation energies, resonant Raman scattering corresponding to different phases could be achieved and thus even embedded minority phases become detectable. Therefore such selective resonant Raman scattering (SRRS) serves as a sensitive technique of probing inhomogeneity properties in an alloy system.

The SRRS of $Mg_xZn_{1-x}O$ alloy films were acquired at room temperature in a backscattering geometry using the Jobin-Yvon T64000 micro-Raman/photoluminescence system equipped with a charge-coupled device (CCD) detector. The probing spot has a spatial resolution of ~1μm and the spectral resolution of the system is ~2cm^{-1}, as introduced in Chapter 2. Both excitation sources of a Kimmon HeCd laser operating at 3.8 eV (325 nm) and a frequency-doubled Lexel Ar-ion laser operating at 5.1 eV (244 nm) were employed in the data acquisition for all films. The spectra of Raman scattering of the $Mg_xZn_{1-x}O$ alloys with both excitations are presented in Figure 4.8.

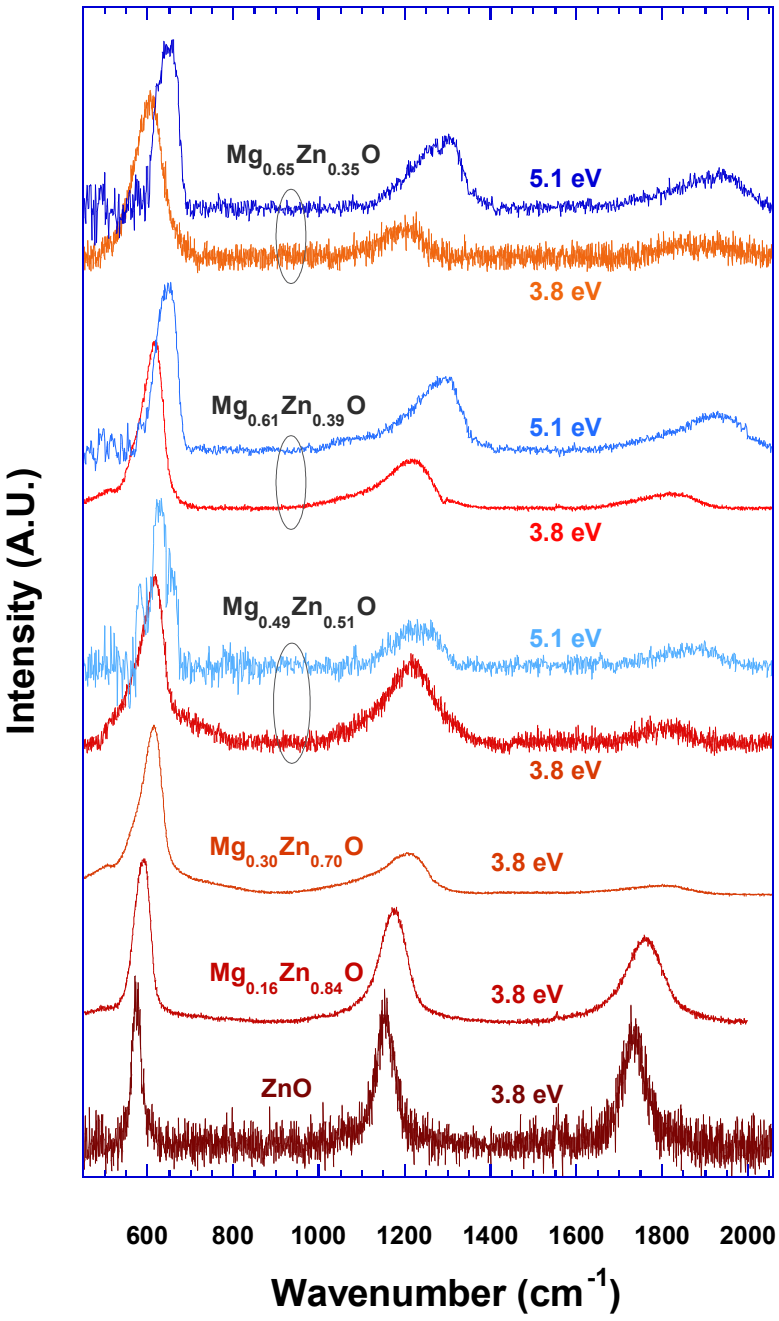

Figure 4.8: The SRRS spectra at room temperature of the LO modes and their higher orders of the $Mg_xZn_{1-x}O$ films. The alloys with x=0, 0.12, and 0.30 exhibit resonant Raman scattering only with the 3.8 eV excitation. The alloys with x=0.49, 0.61, and 0.65 exhibit resonant Raman scattering with both the 3.8 eV and the 5.1 eV excitations. The alloys with x=0.68 and 0.78 did not have Raman scattering upon the 5.1 eV excitation.

According to the Raman selection rules, the scattering of the longitudinal optical (LO) phonon mode in ZnO with the wurtzite structure is allowed[46]. The spectra of the $Mg_xZn_{1-x}O$ films of lower Mg composition (x=0, 0.16, 0.30, 0.49, 0.61, and 0.65), with confirmed wurtzite crystal structure by XRD, exhibit the first LO phonon mode and its higher orders as shown in Figure 4.8, indicating a resonant behavior. The films with x=0, 0.16, and 0.30 did not show any LO Raman scattering under the 5.1 eV excitation. The band gap values of theses films were found to be ranging from 3.2 eV to 3.7 eV as shown in Figure 4.6 (b), which is within the excitation energy range. The SRRS results indicate that this group of $Mg_xZn_{1-x}O$ alloys does not have a significant phase segregation.

In contrast, as can be seen in Figure 4.8, films of Mg compositions x=0.49, 0.61, and, 0.65 exhibit resonant scattering under both the 3.8 eV excitation and the 5.1 eV excitation. Moreover, the 5.1 eV excitation resulted in a significantly higher LO mode frequency. This trend excludes the possibility that the different Raman frequencies under the two excitations are due to probing into the Brillouin zone. The dispersion curve of the LO phonon of ZnO and MgO is a decreasing function of the k-vector[47]. Therefore the 3.8 eV excitation, with a smaller wave vector, should result in a higher frequency LO phonon relative to that of the 5.1 eV excitation, which is not the case observed in this work. Furthermore, a depth profile of the Raman frequency was performed with the 5.1 eV excitation in order to check the impact of its short absorption length and look for possible surface domain segregation with Mg-rich alloys. This experiment resulted in a variance in LO phonon frequencies of about 3 cm^{-1}, which is within the experimental error. Thus a surface segregation is also excluded.

XRD scans with a long acquisition time of 14 hours found that the $Mg_{0.65}Zn_{0.35}O$ film with a wurtzite phase component also exhibits a weak diffraction peak corresponding to the

rocksalt cubic phase, as shown in Figure 4.4. Due to the inversion symmetry of the rocksalt structure, first order Raman scattering is not allowed, however by introducing defects and impurities into the lattice such symmetry can be relaxed and thus the first order Raman scattering can occur[48,49]. It has also been reported that forbidden LO phonons may become Raman active under resonant conditions due to the Fröhlich interaction mechanism[50].

In light of the above results, the different LO phonon frequencies obtained under the two excitations can then be explained in the term of selective resonant enhancement for which each excitation is in resonance with energetically compatible composition fluctuation. The high-frequency LO phonon observed in $Mg_xZn_{1-x}O$ alloys with x=0.49, 0.61 and 0.65 under the 5.1 eV excitation can be attributed to a resonance behavior from Mg-rich rocksalt cubic phase domains with higher band gaps, while the lower frequency LO phonon observed under the 3.8 eV excitation is due to Zn-rich wurtzite phase domains with lower band gaps.

Figure 4.9 summarizes the peak positions of first order LO phonon mode, and the values of band gap energy in $Mg_xZn_{1-x}O$ alloys as a function of Mg composition *x*. Only one mode is observed in the $Mg_xZn_{1-x}O$ alloys, as predicted by the modified random-element-isodisplacement (MREI) model[51]. This model gives the criterion for the existence of the one mode pattern as that the mass (m) of substituting element must not be smaller than the reduced mass (μ) of the compound formed by the other two elements[52]. For $Mg_xZn_{1-x}O$, since $m_{Mg} > \mu_{ZnO}$ and $m_{Zn} > \mu_{MgO}$, such criterion is met therefore the one-mode behavior is exhibited. The frequency of the first order LO phonon under 3.8 eV excitation shows a monotonous increasing from 575 to 622 cm^{-1} as the Mg composition increases from x=0 to x=0.30. This change can be attributed to the change in bond length and reduced mass, which suggests a successful substitution of Mg into the ZnO system. Similar results were found in a

previous study on the resonant Raman behavior of the LO mode in $Mg_xZn_{1-x}O$ films with the wurtzite structure[53]. Such increase in LO peak position shows a saturation in alloys of x=0.49 to 0.65. Meanwhile, a resonance behavior with 5.1 eV excitation was observed with higher LO phonon frequencies at 632 cm^{-1}, 656 cm^{-1}, and, 661 cm^{-1}. Previous study on the phonon behavior in pure cubic phase $Mg_xZn_{1-x}O$ has found LO phonon components at 650 cm^{-1} for similar Mg compositions as these two samples, which is in agreement with what was found in this work[52]. The cubic domains in the two alloys with Mg composition *x*=0.49 and 0.61 may be too small to be detected by XRD analysis. The two alloys with Mg composition *x*=0.68 and 0.78, having the cubic phase in XRD, showed no Raman scattering under the 5.1 eV excitation, which is consistent with the previously discussed Raman selection rules for the rocksalt cubic structure. Furthermore, under room temperature these samples did not show any meaningful evidence under the 3.8 eV excitation of detectable wurtzite phase domains either.

As can be seen in Figure 4.9, the phase segregation in $Mg_xZn_{1-x}O$ alloy films is also indicated in the change in band gaps. For alloys of *x*=0.49 to *x*=0.65, a saturation in the band gap is shown. The alloys of *x*=0.68 and *x*=0.78 with a cubic phase have significantly higher band gaps. This confirms that the derivative method is an accurate approach for obtaining the band gap of the majority-phase.

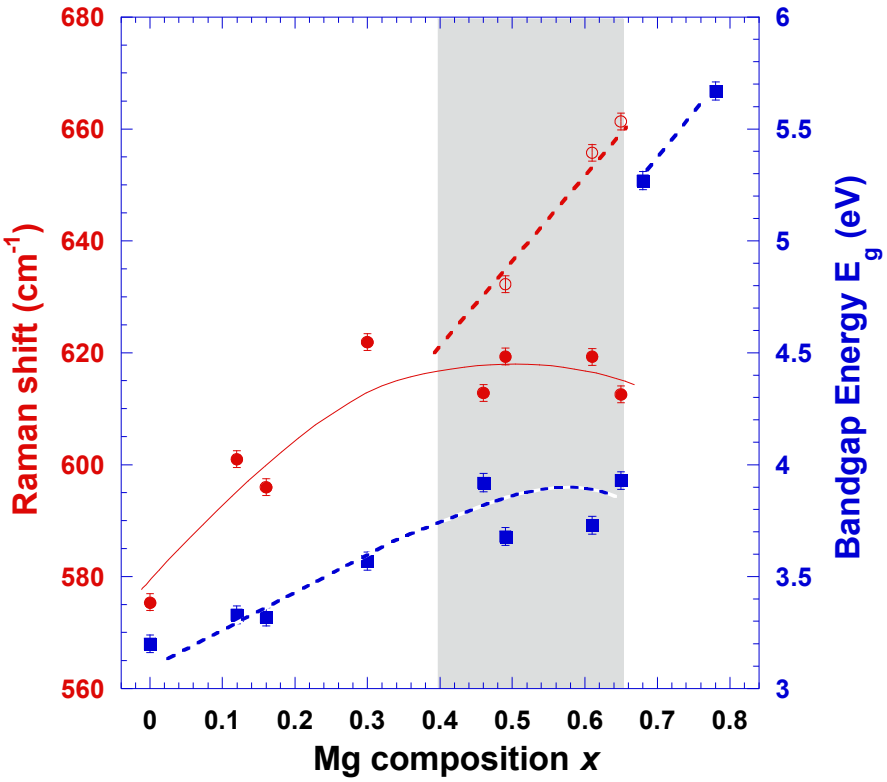

Figure 4.9: A summary of the first order LO phonon frequencies obtained via SRRS, and the bandgaps obtained via the inflection point analysis of the $Mg_xZn_{1-x}O$ alloys grown for this study. The solid circles conclude data acquired under the 3.8 eV excitation while the open circles conclude data acquired under 5.1 eV excitation. The solid squares represent the bandgap energy. The frequencies of the first order LO phonon of $Mg_xZn_{1-x}O$ films under 3.8 eV excitation increases monotonously with the increasing Mg composition from x=0 to x=0.30, due to the changes in bond length and reduced mass in the alloys, suggesting a successful alloying. The increase in LO peak position under 3.8 eV saturates beyond x=0.49 and resonance behavior with 5.1 eV excitation with higher LO frequencies was observed, which is consistent with the phonon behavior in cubic phase $Mg_xZn_{1-x}O$ alloys. The alloys of high Mg composition (x=0.68 and 0.78) with cubic structure did no show any resonant behavior under either excitation, as predicted by the selection rules. Similar phase segregation effect can be seen in the change in bandgap energy as well. The shaded area suggests possible phase segregation region and the curves are guides to the eye.

4.5 The study of phonon dynamics in $Mg_xZn_{1-x}O$ alloys

4.5.1 The Raman spectral line broadening analysis

As can be seen in Figure 4.8, the Raman spectral lines of $Mg_xZn_{1-x}O$ films show a broadening with respect to the Mg composition. Figure 4.10 focuses on the first order of LO phonon peaks in Raman spectra for all $Mg_xZn_{1-x}O$ films acquired under 3.8 eV excitation.

The LO spectral lines for all alloys of $x>0$ show an asymmetric line-shape which is composed of two contributions: a main peak of high intensity, accompanied with a weaker peak at the lower frequency side. In contrast, the Raman spectral line of the ZnO has little asymmetry component. As reported by the previous work of $Mg_xZn_{1-x}O$ nanocrystals[54], the main spectral line of both the $Mg_xZn_{1-x}O$ alloys and the ZnO may be attributed to the LO mode, while the weaker peak at a lower frequency is due to the alloying effect. The random substitution of Mg into ZnO lattice results in distortion of the lattice periodicity, which gives a rise to a relaxation of the $\mathbf{q}=0$ selection rule in Raman scattering[55]. Thus for the LO mode scattering in this case the minor components at lower frequencies are a collective of modes with $\mathbf{q}>0$[56]. Based on the analysis above, deconvolution of the spectral lines to two Voigt peaks were performed by fitting via the software Peakfit. An example fitting of the first order LO peak for $Mg_{0.65}Zn_{0.35}O$ is shown in Figure 4.10. The intense main peak with higher phonon frequency is the interest of this study. The degree of broadening is measured as the full width at half maximum (FWHM) of a peak, represented by Γ.

The FWHM of the first order LO Raman mode and the respective Urbach energy E_u of the $Mg_xZn_{1-x}O$ films grown for this study are summarized in Figure 4.16. The broadening of LO peaks shows a Mg composition sensitive behavior.

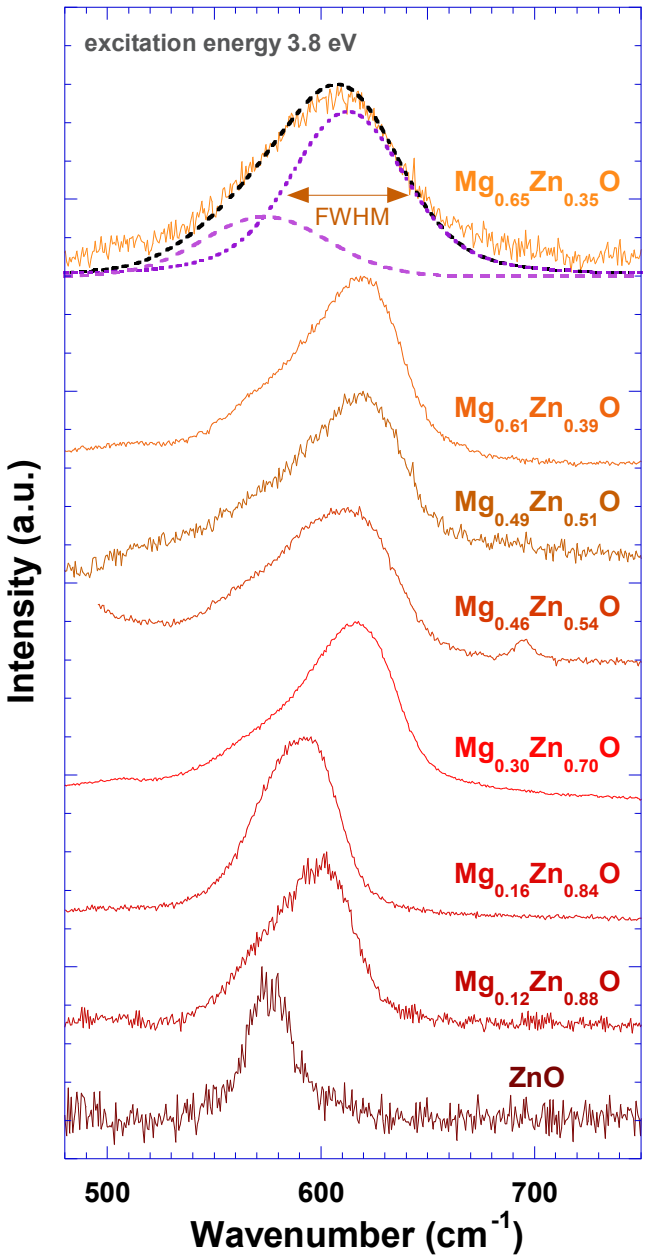

Figure 4.10: The first order of LO phonon spectra for all $Mg_xZn_{1-x}O$ alloys which are in resonant with the 3.8 eV excitation. A trend of broadening in the spectral linewidth with respect to the increasing Mg composition is observed and peaks were fitted to obtain the value of FWHM. A representative fitting is shown in dashed lines for the spectrum of $Mg_{0.65}Zn_{0.35}O$.

The possible mechanisms of the main Raman spectral line broadening applicable to the $Mg_xZn_{1-x}O$ alloy films grown for this study include:

(1) The granular morphologies in the $Mg_xZn_{1-x}O$ films introduce structural defects such as grain boundaries and dangling bonds, which distort the periodicity of the lattice structure. The interaction between phonons and such distortion shortens the phonon lifetime and therefore cause a homogeneous broadening of spectral lines[57–59], as illustrated in Figure 4.11 (a);

(2) The alloy compositional fluctuation causes variations in the phonon frequency of the alloy[60–63], which results in a Raman spectral line broadening known as the inhomogeneous broadening, as illustrated in Figure 4.11 (b);

(3) Phonon decay due to the alloy's nature of anharmonicity[64] also shortens phonon lifetime and thus cause the homogeneous broadening.

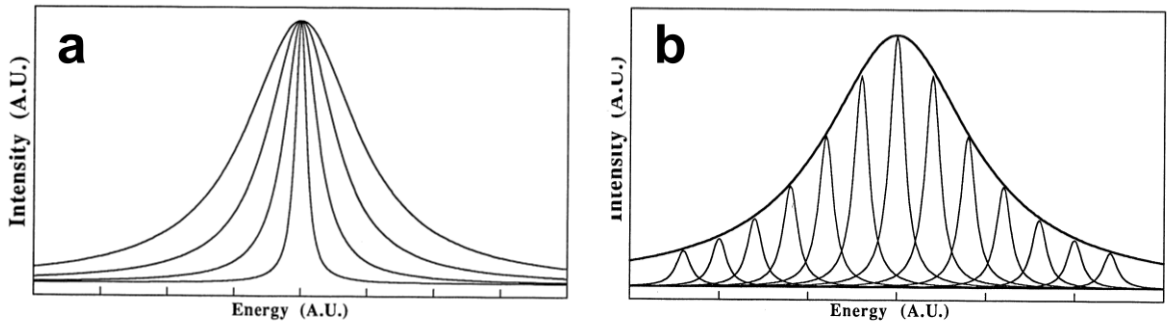

Figure 4.11: The Raman spectral line broadening mechanisms: ***(a)*** *homogeneous broadening and* ***(b)*** *inhomogeneous broadening.*

4.5.2 Investigation into the phonon decay in $Mg_xZn_{1-x}O$ alloys films due to anharmonicity

Further studies on the phonon decay effect in the $Mg_xZn_{1-x}O$ films were carried out, in order to quantify the contribution of phonon decay due to anharmonicity to the broadening of Raman spectral lines.

The behavior of the Raman spectral line broadening with respect to temperature may be described in terms of the phonon decay model proposed by Balkanski[40]. In such model, an optical phonon decays into two and three phonons, referred to as three- and four-phonon decay process. According to this model, Raman spectral linewidth as a function of temperature can be expressed[65]:

$$\Gamma(T)=\Gamma_0+\Delta\Gamma(T)=\Gamma_0+A\cdot\left[1+\sum_{i=1}^{2}\frac{1}{e^{\frac{\hbar\omega_i}{k_BT}}-1}\right]+B\cdot\left\{1+\sum_{j=1}^{3}\left[\frac{1}{e^{\frac{\hbar\omega_j}{k_BT}}-1}+\frac{1}{\left(e^{\frac{\hbar\omega_j}{k_BT}}-1\right)^2}\right]\right\} \qquad (4.1)$$

where Γ_0 represents the temperature independent Raman spectral line broadening. While $\Delta\Gamma(T)$ is the broadening effect due to phonon decay processes. ω_i (i=1, 2, 3) are the frequencies of the phonons involved in the decay channels. The anharmonic constant *A* and *B* give a measure of the probability of three- and four-phonon decay process occurring. By using Equation 4.1 as a fitting model for the experimental results of Raman spectral line broadening, the contribution of phonon decay induced broadening can be quantified. The procedures of performing such model fitting will be discussed as following.

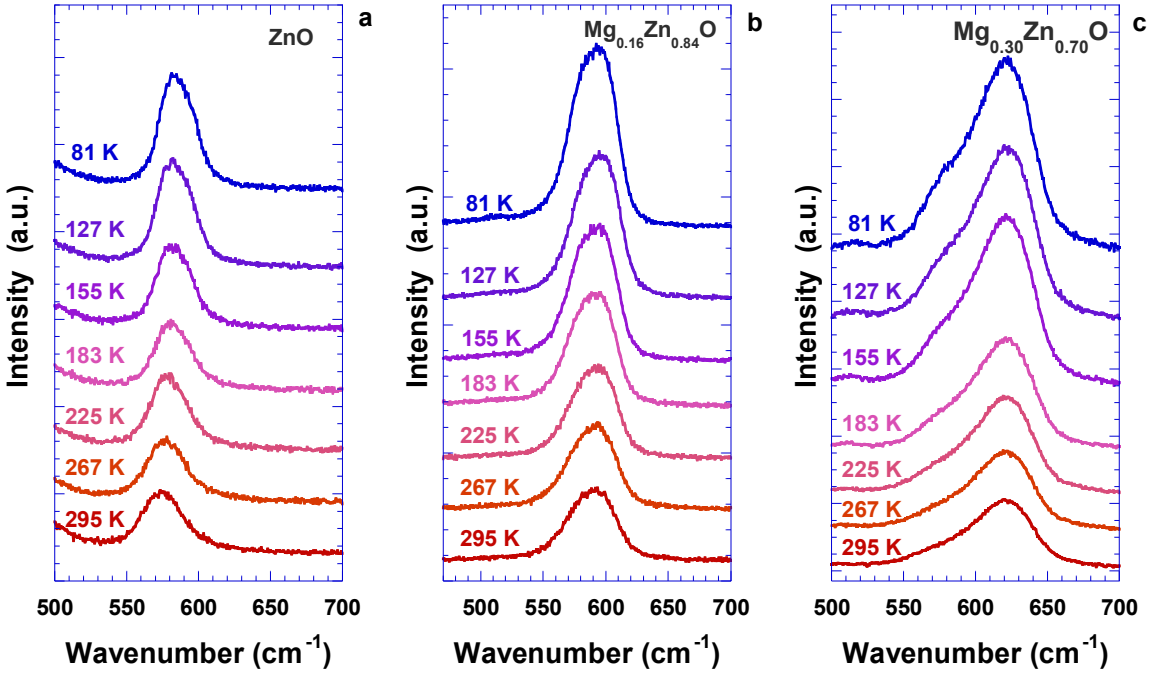

Figure 4.12: Raman spectra of the first order LO mode in ***(a)*** *ZnO,* ***(b)*** *$Mg_{0.16}Zn_{0.84}O$, and,* ***(c)*** *$Mg_{0.30}Zn_{0.70}O$ films at various temperatures from 81K to room temperature. The peak positions showed an increasing while the FWHM showed a continuous decreasing with the reduction of temperature.*

- Step 1-3: Acquiring experimental results of Raman line widths as a function of temperature Γ(T).

Resonant Raman spectra of $Mg_xZn_{1-x}O$ films with x=0, x=0.16, and, x=0.30 were acquired under the 3.8 eV excitation at various temperatures from 295 K down to 81 K. Figure 4.12 presents the first order LO phonon mode of the films at representative temperatures. As can be seen from Figure 4.12, as temperature increases the main peak exhibits a continuous broadening.

- Step 2-3: Obtaining reasonable phonon decay channels of $Mg_xZn_{1-x}O$ alloys for the model fitting of Γ(T).

In order to perform a reliable model fitting with Equation 4.1, the phonon decay channels ω_i can be obtained in advance.

Balkanski's model states that the Raman frequency at a given temperature, ω(T), can be calculated as[40]:

$$\omega(T)=\omega_0 - C\cdot\left[1+\sum_{i=1}^{2}\frac{1}{e^{\frac{\hbar\omega_i}{k_B T}}-1}\right] - D\cdot\left\{1+\sum_{j=1}^{3}\left[\frac{1}{e^{\frac{\hbar\omega_j}{k_B T}}-1}+\frac{1}{\left(e^{\frac{\hbar\omega_j}{k_B T}}-1\right)^2}\right]\right\} \qquad (4.2)$$

where ω_0 is the harmonic term of the LO phonon frequency which is temperature independent. C and D are anharmonic constants which are similar to constants A and B in Equation 4.1.

The phonon frequencies of the decay channel ω_i may be determined from the phonon dispersion curves and phonon density of states with the constraint that the conservation of both energy AND momentum holds. However, the phonon dispersion curves of $Mg_xZn_{1-x}O$

alloys are currently unknown, therefore an approximation is needed. The most fundamental approximation of decay channels is the Klemens[66] model, which approximates that in the three-phonon decay process one optical phonon decays into two phonons with identical frequencies. With the restraint of energy conservation (i.e. $\omega_1+\omega_2=\omega_0$), for three-phonon process, Klemens model yields $\omega_1=\omega_2=\frac{\omega_0}{2}$.

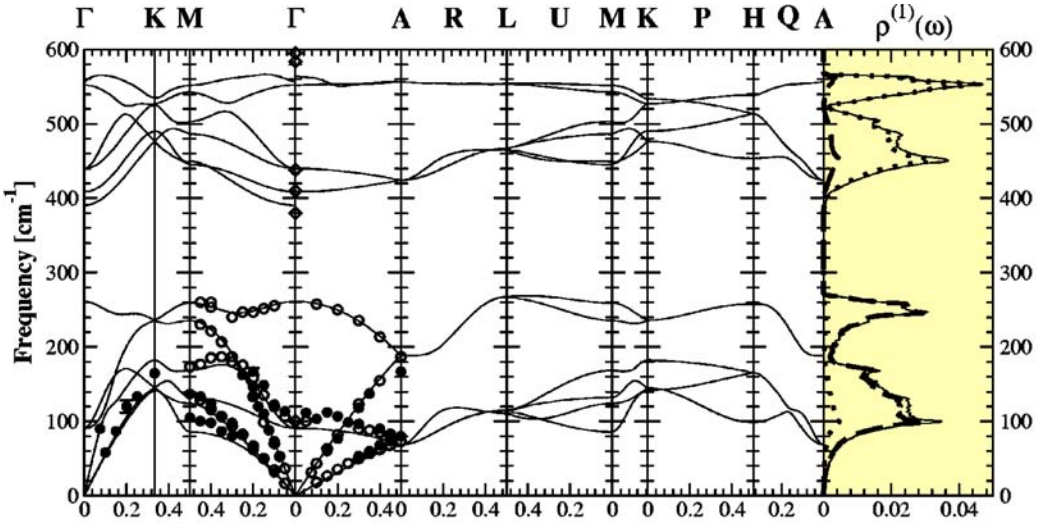

Figure 4.13: The phonon dispersion curves of ZnO with a wurtzite structure, calculated by Serrano et al.[68].

However, for materials having wurtzite structure such as GaN[67] and ZnO[68] this approximation is typically invalid since according to their phonon dispersion curves there are no possible phonon states exist in the required energy region, and it is expected to be the case for wurtzite $Mg_xZn_{1-x}O$ as well. Instead, we consider the Ridley channel decay model[67,69], where a single LO mode decays into a TO and a TA mode. Previous work by Cuscó *et al.*[70] based on this decay model and the phonon dispersion curves[68] shown in Figure 4.13

established a reasonable decay channel for pure wurtzite structured ZnO, in which a LO mode ω_0 decays into a TO mode of $\omega_1 = 455$ cm^{-1} and a TA mode of $\omega_2 = 120$ cm^{-1} in the L-M direction[70].

Since the dispersion curves of $Mg_xZn_{1-x}O$ alloys with wurtzite structures are currently unknown, their TO phonon frequencies were estimated by considering following known factors: the behavior of the zone center phonons with respect to Mg composition, the phonon dispersion curves of wurtzite ZnO, and, the Mg composition of the film. The composition dependence of the frequency of zone-center phonons $\omega^{\Gamma}(x)$ in $Mg_xZn_{1-x}O$ is suggested by Ye *et al.*[71] as following:

$$\omega^{\Gamma}(x)=\omega_{ZnO}(1-x)+\omega_{MgO}(x)-bx(1-x) \tag{4.3}$$

For the zone center TO mode in $Mg_xZn_{1-x}O$ the appropriate values for Equation 4.3 are reported by Wenckstern *et al.*[72]to be: $\omega_{ZnO} = 406$ cm^{-1}, $\omega_{MgO} = 408$ cm^{-1} and $b = -67$ cm^{-1}. Therefore for Mg composition x=0.16, $\omega_{TO}^{\Gamma}(0.16)\approx 415\,cm^{-1}$ is obtained. The decay process in wurtzite ZnO are dominated by phonons in the L-M direction which are at different frequencies than the zone center phonons, and it is probable that wurtzite $Mg_xZn_{1-x}O$ follows a similar behavior. Therefore it is assumed that the frequency difference between the zone center and branches in the L-M direction is only weakly dependent on composition. Based on the known dispersion curves of wurtzite ZnO as shown in Figure 4.13 the frequency difference between the zone center and L-M direction is estimated to be $\Delta\omega_{TO}^{\Gamma-LM}\approx 49\,cm^{-1}$. As a result the frequency of the TO mode decay channel in $Mg_{0.16}Zn_{0.84}O$ is estimated to be $\omega_1=\omega_{TO}^{\Gamma}(0.16)+\Delta\omega_{TO}^{\Gamma-LM}\approx 464\,cm^{-1}$. For determining the

appropriate TA mode decay channel the constraint of energy conservation was applied such that $\omega_2=\omega_0-\omega_1$. Following the same estimation, the TO mode frequency of $Mg_{0.30}Zn_{0.70}O$ is $\omega_1=\omega_{TO}^{\Gamma}(0.30)+\Delta\omega_{TO}^{\Gamma-LM}\approx 470\,cm^{-1}$.

Based on the above estimation, the experimental data of temperature dependent LO phonon frequencies in $Mg_xZn_{1-x}O$ films of x=0, x=0.16, and, x=0.30 were fitted by the three-phonon process decay model (i.e. D ≡ 0 in Equation 4.2) and it appears to be largely adequate, as shown in Figure 4.14. The phonon decay channels are thus obtained from this model fitting and are concluded as:

Material	ω_0 (cm^{-1})	ω_1 (cm^{-1})	$\omega_2=\omega_0-\omega_1$ (cm^{-1})
ZnO	593	455	138
$Mg_{0.16}Zn_{0.74}O$	605	460	145
$Mg_{0.30}Zn_{0.70}O$	625	480	145

Table 4.2: The phonon decay channels ω_0, ω_1, and, ω_2 in $Mg_xZn_{1-x}O$ films obtained by fitting the experimental results of LO phonon frequencies at various temperatures with the three-phonon decay model.

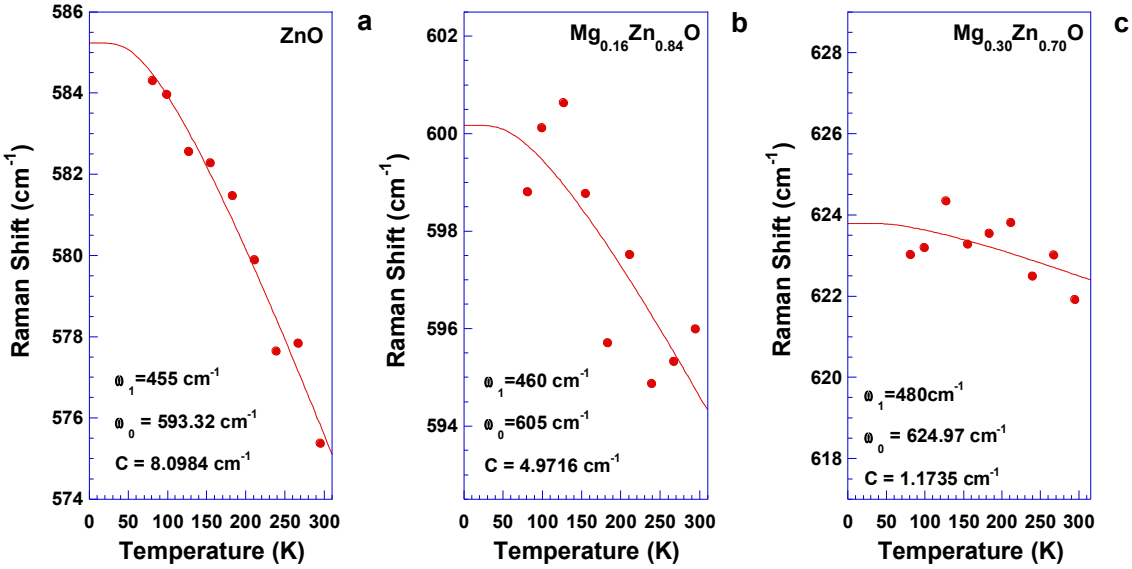

Figure 4.14: The temperature dependent behavior of LO phonon frequencies in (a) ZnO, (b) $Mg_{0.16}Zn_{0.84}O$, and, (c) $Mg_{0.30}Zn_{0.70}O$ films were modeled in terms of three-phonon process and phonon decay channels ω_1 and $\omega_2=\omega_0-\omega_1$, consequently, for individual alloy can be obtained via fitting.

- Step 3-3: Performing Γ(T) model fitting with obtained phonon decay channels ω_0, ω_1, and ω_2.

The decay channels obtained above can then be used in fitting the temperature dependent FWHM of the first order LO mode in ZnO, $Mg_{0.16}Zn_{0.74}O$, and, $Mg_{0.30}Zn_{0.70}O$ with the three-phonon process (i.e. B ≡ 0 in Equation 4.1). Figure 4.15 presents the fitting results. The two contributions to the Raman line broadening, Γ_0 and ΔΓ(300K), obtained from the fittings are summarized as following:

Material	Γ(300K) (cm^{-1})	Γ_0 (cm^{-1})	$\Delta\Gamma = \Gamma(300K) - \Gamma_0$ (cm^{-1})
ZnO	32	23±2	9±2
$Mg_{0.16}Zn_{0.74}O$	33	19±2	14±2
$Mg_{0.30}Zn_{0.70}O$	44	33±2	11±2

Table 4.3: The temperature independent contribution in Raman line broadening Γ_0 and the phonon decay contribution in broadening $\Delta\Gamma$ in $Mg_xZn_{1-x}O$ films obtained by fitting the experimental results of the FWHM of first order LO Raman spectra at various temperatures with the three-phonon decay model.

Considering the error from spectrometer and from model fitting of ~2 cm^{-1}, The contribution to Raman line broadening due to phonon decay process $\Delta\Gamma_{x=0} \approx 9 \pm 2$ cm^{-1}, $\Delta\Gamma_{x=0.16} \approx 14 \pm 2$ cm^{-1}, and, $\Delta\Gamma_{x=0.30} \approx 11 \pm 2$ cm^{-1} show small variation and no obvious alloy composition dependence. While the temperature independent broadening Γ_0 corresponding to structural defects and alloy compositional composition exhibits a significant increase from $\Gamma_0^{x=0} \approx 23 \pm 2$ cm^{-1} and $\Gamma_0^{x=0.16} \approx 19 \pm 2$ cm^{-1}, to $\Gamma_0^{x=0.30} \approx 33 \pm 2$ cm^{-1}, which agrees well with the Mg composition dependent increase in the FWHM of the first order LO peaks of $Mg_xZn_{1-x}O$ alloys at room temperature, as shown in Figure 4.16. Based on the discussion above, it can be concluded that in the $Mg_xZn_{1-x}O$ alloy films grown for this work, the structural defects and

the alloy compositional fluctuations serve as the dominant mechanism of the Raman spectral line broadening. While the broadening effect due to phonon decay is not significant.

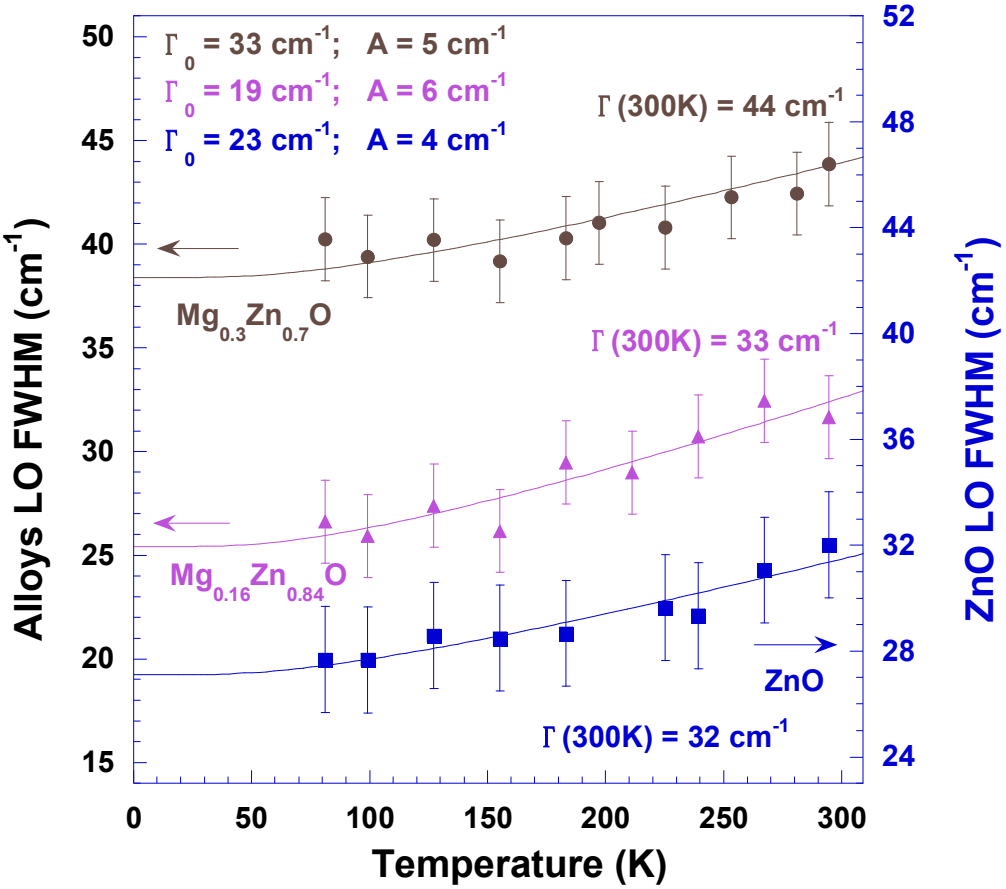

Figure 4.15: The temperature dependent FWHM of the first order LO Raman main peak of ZnO, $Mg_{0.16}Zn_{0.84}O$, and, $Mg_{0.30}Zn_{0.70}O$ films. The data were fitted by the three-phonon decay model. The broadening $\Delta\Gamma$ due to phonon decay process exhibit no obvious alloy composition dependent. While the inherent broadening factor Γ_0 corresponding to structural defects and compositional fluctuations appears to be dominating the Raman broadening observed in this study.

4.5.3 The strong correlation between Urbach energy and Raman spectral line width

Figure 4.16 presents the summary of Urbach energy and Raman line width as a function of Mg composition. Comparing the Mg composition sensitive behavior of the FWHM of the main LO peak with that of the Urbach energy E_u, a strong correlation between the two can be seen. Recall the possible mechanisms that may induce electronic tail states in the band gap as addressed in Section 4.3.2, it is suggested that the effect of structural defects and alloy compositional fluctuations serve as the dominant mechanisms of both the Raman line broadening and the Urbach energy of the $Mg_xZn_{1-x}O$ alloys grown for this work.

For the $Mg_xZn_{1-x}O$ alloys with low Mg composition ($0 \leq x < 0.30$), the solubility of Mg^{2+} is sufficient that Mg^{2+} 's randomly substitute Zn^{2+} sites in a wurtzite ZnO lattice, with little fluctuation in the Mg composition throughout the film. However, the granular morphologies of the films, as shown in Figure 4.3, create grain boundaries and dangling bonds. Such structural defects distort the periodicity in the lattice and thus cause the localization of electronic states in the band gap, and, shorten the phonon lifetime. On the other hand, for the $Mg_xZn_{1-x}O$ alloys with Mg composition $x \geq 0.30$, the distribution of Mg^{2+} in the ZnO lattice started to exhibit inhomogeneous due to the tendency of phase segregation. Such fluctuations in alloy compositions cause electronic band tail states[73,74] and variations in phonon frequencies[56], which are reflected by the increased Urbach energy and the broadened LO phonon spectral line, respectively. More fluctuations in the alloy compositions can exhibit when the Mg content increases[75], which explains the significant increase in E_u and FWHM values of $Mg_xZn_{1-x}O$ alloys in deep phase segregation region, as shown in Figure 4.16.

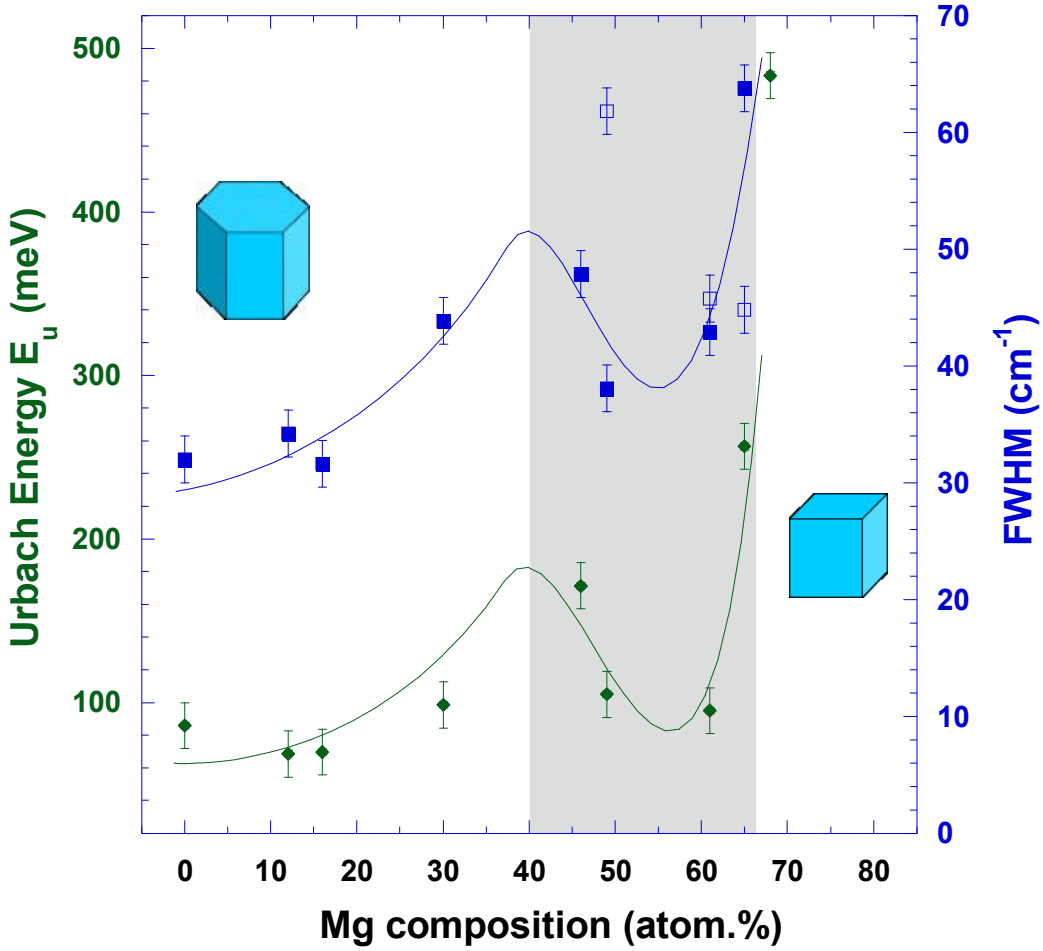

Figure 4.16: The FWHM of the first order LO Raman main peak of the $Mg_xZn_{1-x}O$ alloys (solid squares) as a function of the Mg composition. A strong correlation between the Raman line width and Urbach energy (solid diamonds) is shown.The shaded area represents the possible phase segregation region and the lines are guides to the eye.

4.6 Conclusion

$Mg_xZn_{1-x}O$ thin films were synthesized via reactive magnetron sputtering. Bandgap engineering of $Mg_xZn_{1-x}O$ alloys was successfully achieved from 3.2 eV to 5.7 eV, as an increasing Mg composition from x=0 to x=0.78.

The phase segregation characteristic due to the difference in crystal structures between the two end members, was probed via Selective resonant Raman scattering. Alloys with Mg composition $0 \leq x \leq 0.30$ exhibited resonant behavior only with the 3.8 eV excitation, indicating the film growth favoring the wurtzite phase without segregating. Alloys with higher Mg composition $0.49 \leq x \leq 0.65$ were found to be in resonance with both the 3.8 eV and the 5.1 eV excitations, indicating the coexisting of both wurtzite and cubic phases. For alloys with a Mg composition $x \geq 0.68$, no meaningful Raman scattering occurred, suggesting no existing of detectable wurtzite domains. The possible phase segregation range of the studied $Mg_xZn_{1-x}O$ alloys was found to be approximately $0.40 \leq x \leq 0.65$.

A correlation was found between the Urbach energy and the first order LO Raman linewidth in the $Mg_xZn_{1-x}O$ alloys. Investigation into the phonon dynamics via temperature dependent Raman scattering below room temperature suggested that the phonon decay process is not the dominant mechanism of the LO Raman main peak broadening. Both the Urbach tail absorption and the Raman spectral line broadening are induced by structural defects and alloy compositional fluctuations in the $Mg_xZn_{1-x}O$ alloy films.

4.7 References

1. Wu, P.-C., Lee, H.-Y. & Lee, C.-T. Enhanced light emission of double heterostructured MgZnO/ZnO/MgZnO in ultraviolet blind light-emitting diodes deposited by vapor cooling condensation system. *Appl. Phys. Lett.* **100,** 131116 (2012).

2. Choi, Y.-S., Kang, J.-W., Kim, B.-H. & Park, S.-J. Enhanced ultraviolet emission of MgZnO/ZnO multiple quantum wells light-emitting diode by p-type MgZnO electron blocking layer. *Opt. Express* **21,** 31560–31566 (2013).

3. Jun, L. *et al.* Applications of Cubic MgZnO Thin Films in Metal–Insulator–Silicon Structures. *Chin. Phys. Lett.* **21,** 1135 (2004).

4. A. Lloyd Spetz, A. B. High Temperature Sensors Based on Metal–Insulator–Silicon Carbide Devices. *Phys. Status Solidi A* **162,** 493 – 511 (2001).

5. Wang, P. *et al.* Steady-state characteristics and transient response of MgZnO-based metal-semiconductor-metal solar-blind ultraviolet photodetector with three types of electrode structures. *Opt. Express* **21,** 18387–18397 (2013).

6. Segnit, E. R. & Holland, A. E. The System MgO-ZnO-SiO_2. *J. Am. Ceram. Soc.* **48,** 409–413 (1965).

7. Ohtomo, A. *et al.* $Mg_xZn_{1-x}O$ as a II–VI widegap semiconductor alloy. *Appl. Phys. Lett.* **72,** 2466–2468 (1998).

8. Sharma, A. K. *et al.* Optical and structural properties of epitaxial $Mg_xZn_{1-x}O$ alloys. *Appl. Phys. Lett.* **75,** 3327–3329 (1999).

9. Ohtomo, A. *et al.* Structure and optical properties of ZnO/$Mg_{0.2}Zn_{0.8}O$ superlattices. *Appl. Phys. Lett.* **75,** 980 (1999).

10. Park, W. I., Yi, G.-C. & Jang, H. M. Metalorganic vapor-phase epitaxial growth and photoluminescent properties of $Zn_{1-x}Mg_xO$(0 #x2264;x #x2264;0.49) thin films. *Appl. Phys. Lett.* **79,** 2022–2024 (2001).

11. Xiong, D. P. *et al.* Deposition of ZnO and MgZnO films by magnetron sputtering. *Vacuum* **89,** 254–256 (2013).

12. Zhao, Y. *et al.* Ultraviolet Photodetector Based on a MgZnO Film Grown by Radio-Frequency Magnetron Sputtering. *ACS Appl. Mater. Interfaces* **1,** 2428–2430 (2009).

13. Choopun, S. *et al.* Realization of band gap above 5.0 eV in metastable cubic-phase $Mg_xZn_{1-x}O$ alloy films. *Appl. Phys. Lett.* **80,** 1529 (2002).

14. Wang, L. K. *et al.* Single-crystalline cubic MgZnO films and their application in deep-ultraviolet optoelectronic devices. *Appl. Phys. Lett.* **95,** 131113 (2009).

15. Yang, W. *et al.* Compositionally-tuned epitaxial cubic $Mg_xZn_{1-x}O$ on Si(100) for deep ultraviolet photodetectors. *Appl. Phys. Lett.* **82,** 3424–3426 (2003).

16. Verstraete, M. & Gonze, X. First-principles calculation of the electronic, dielectric, and dynamical properties of CaF2. *Phys. Rev. B* **68,** 195123 (2003).

17. Weinberg, Z. A., Rubloff, G. W. & Bassous, E. Transmission, photoconductivity, and the experimental band gap of thermally grown SiO2 films. *Phys. Rev. B* **19,** 3107–3117 (1979).

18. Ghosh, R., Basak, D. & Fujihara, S. Effect of substrate-induced strain on the structural, electrical, and optical properties of polycrystalline ZnO thin films. *J. Appl. Phys.* **96,** 2689–2692 (2004).

19. Srikant, V. & Clarke, D. R. Optical absorption edge of ZnO thin films: The effect of substrate. *J. Appl. Phys.* **81,** 6357–6364 (1997).

20. Yoshino, K., Oyama, S. & Yoneta, M. Structural, optical and electrical characterization of undoped ZnMgO film grown by spray pyrolysis method. *J. Mater. Sci. Mater. Electron.* **19,** 203–209 (2008).

21. Zhang, X., Li, X. M., Chen, T. L., Bian, J. M. & Zhang, C. Y. Structural and optical properties of $Zn_{1-x}Mg_xO$ thin films deposited by ultrasonic spray pyrolysis. *Thin Solid Films* **492,** 248–252 (2005).

22. Jung, E. Y., Lee, S. G., Sohn, S. H., Lee, D. K. & Kim, H. K. Electrical properties of plasma display panel with $Mg_{1-x}Zn_xO$ protecting thin films deposited by a radio frequency magnetron sputtering method. *Appl. Phys. Lett.* **86,** 3503 (2005).

23. Cahn, J. W. The impurity-drag effect in grain boundary motion. *Acta Metall.* **10,** 789–798 (1962).

24. Bennison, S. J. & Harmer, M. P. Effect of MgO Solute on the Kinetics of Grain Growth in A12O3. *J. Am. Ceram. Soc.* **66,** C–90–C–92 (1983).

25. Morrison, J. L. *et al.* Optical properties of ZnO and MgZnO nanocrystals below and at the phase separation range. *J. Appl. Phys.* **104,** 123519 (2008).

26. Morkoç, H. & Özgür, Ü. *Zinc oxide: fundamentals, materials and device technology.* (Wiley-VCH, 2009).

27. Freund, L. B. & Suresh, S. *Thin film materials: stress, defect formation, and surface evolution*. (Cambridge University Press, 2003).

28. Tauc, J. *Amorphous and liquid semiconductors*. (Plenum, 1974).

29. Tan, S. T. *et al.* Blueshift of optical band gap in ZnO thin films grown by metal-organic chemical-vapor deposition. *J. Appl. Phys.* **98,** 013505 (2005).

30. Che, H. *et al.* Optical Properties of ZnO-Alloyed Nanocrystalline Films. *J. Nanomater.* **2012,** (2012).

31. Wang, M. *et al.* Optical and structural properties of sol–gel prepared MgZnO alloy thin films. *Thin Solid Films* **516,** 1124–1129 (2008).

32. Viswanatha, R., Chakraborty, S., Basu, S. & Sarma, D. D. Blue-emitting copper-doped zinc oxide nanocrystals. *J. Phys. Chem. B* **110,** 22310–22312 (2006).

33. Urbach, F. The Long-Wavelength Edge of Photographic Sensitivity and of the Electronic Absorption of Solids. *Phys. Rev.* **92,** 1324–1324 (1953).

34. Bansal, B., Dixit, V. K., Venkataraman, V. & Bhat, H. L. Alloying induced degradation of the absorption edge of $InAs_xSb_{1-x}$. *Appl. Phys. Lett.* **90,** 101905 (2007).

35. Zanatta, A. R., Mulato, M. & Chambouleyron, I. Exponential absorption edge and disorder in Column IV amorphous semiconductors. *J. Appl. Phys.* **84,** 5184–5190 (1998).

36. Brunner, D. *et al.* Optical constants of epitaxial AlGaN films and their temperature dependence. *J. Appl. Phys.* **82,** 5090–5096 (1997).

37. Teng, C. W. *et al.* Refractive indices and absorption coefficients of $Mg_xZn_{1-x}O$ alloys. *Appl. Phys. Lett.* **76,** 979–981 (2000).

38. Batool, Z. *et al.* The electronic band structure of GaBiAs/GaAs layers: Influence of strain and band anti-crossing. *J. Appl. Phys.* **111,** 113108 (2012).

39. Reihlen, E. H., Jou, M. J., Jaw, D. H. & Stringfellow, G. B. Optical absorption and emission of $GaP_{1-x}Sb_x$ alloys. *J. Appl. Phys.* **68,** 760–767 (1990).

40. Balkanski, M., Wallis, R. F. & Haro, E. Anharmonic effects in light scattering due to optical phonons in silicon. *Phys. Rev. B* **28,** 1928–1934 (1983).

41. Lai, S. & Klein, M. V. Evidence for Exciton Localization by Alloy Fluctuations in Indirect-Gap $GaAs_{1-x}P_x$. *Phys. Rev. Lett.* **44,** 1087–1090 (1980).

42. Huso, J. *et al.* Optical transitions and multiphonon Raman scattering of Cu doped ZnO and MgZnO ceramics. *Appl. Phys. Lett.* **94,** 061919 (2009).

43. D. A. Long (Derek Albert). *Raman spectroscopy*. (McGraw-Hill, 1977).

44. Gammon, D. in *Raman Scatt. Mater. Sci.* (Weber, D. W. H. & Merlin, P. R.) 109–147 (Springer Berlin Heidelberg, 2000).

45. Gammon, D. *et al.* Nuclear Spectroscopy in Single Quantum Dots: Nanoscopic Raman Scattering and Nuclear Magnetic Resonance. *Science* **277,** 85–88 (1997).

46. Damen, T. C., Porto, S. P. S. & Tell, B. Raman Effect in Zinc Oxide. *Phys. Rev.* **142,** 570–574 (1966).

47. Bilz, P. D. H. & Kress, D. W. in *Phonon Dispers. Relat. Insul.* (Springer Berlin Heidelberg, 1979).

48. Raptis, C. Evidence of temperature-defect-induced first-order Raman scattering in pure NaCl crystals. *Phys. Rev. B* **33,** 1350–1352 (1986).

49. Ishikawa, K., Fujima, N. & Komura, H. First-order Raman scattering in MgO microcrystals. *J. Appl. Phys.* **57,** 973–975 (1985).

50. Smith, G. D., Firth, S., Clark, R. J. H. & Cardona, M. First- and second-order Raman spectra of galena (PbS). *J. Appl. Phys.* **92,** 4375–4380 (2002).

51. Chang, I. F. & Mitra, S. S. Application of a Modified Random-Element-Isodisplacement Model to Long-Wavelength Optic Phonons of Mixed Crystals. *Phys. Rev.* **172,** 924–933 (1968).

52. Chen, J. & Shen, W. Z. Long-wavelength optical phonon properties of ternary MgZnO thin films. *Appl. Phys. Lett.* **83,** 2154–2156 (2003).

53. Kong, J. F., Shen, W. Z., Zhang, Y. W., Yang, C. & Li, X. M. Resonant Raman scattering probe of alloying effect in ZnMgO thin films. *Appl. Phys. Lett.* **92,** 191910 (2008).

54. Huso, J. *et al.* Low temperature LO-phonon dynamics of MgZnO nanoalloys. *Appl. Phys. Lett.* **91,** 111906 (2007).

55. Parayanthal, P. & Pollak, F. H. Raman Scattering in Alloy Semiconductors: 'Spatial Correlation' Model. *Phys. Rev. Lett.* **52,** 1822–1825 (1984).

56. Liu, M. S., Bursill, L. A. & Prawer, S. Optical phonons of hexagonal $Al_xGa_{1-x}N$: Simulation and experiment. *J. Appl. Phys.* **90,** 1761–1767 (2001).

57. Falkovsky, L. A., Bluet, J. M. & Camassel, J. Strain-fluctuation effect on Raman spectra. *Phys. Rev. B* **55,** R14697–R14700 (1997).

58. Evans, D. J. & Ushioda, S. Strain induced phonon line broadening observed by surface reflection Raman scattering. *Solid State Commun.* **11,** 1043–1047 (1972).

59. Chen, J. *et al.* Probing Strain in Bent Semiconductor Nanowires with Raman Spectroscopy. *Nano Lett.* **10,** 1280–1286 (2010).

60. Olego, D. J., Raccah, P. M. & Faurie, J. P. Compositional dependence of the Raman frequencies and line shapes of $Cd_{1-x}Zn_xTe$ determined with films grown by molecular-beam epitaxy. *Phys. Rev. B* **33,** 3819–3822 (1986).

61. Lin, L. Y. *et al.* Raman investigation of anharmonicity and disorder-induced effects in $Zn_{1-x}Be_xSe$ epifilms. *Phys. Rev. B* **69,** 075204 (2004).

62. Pan, C.-J., Lin, K.-F., Hsu, W.-T. & Hsieh, W.-F. Raman study of alloy potential

fluctuations in $Mg_x Zn_{1-x} O$ nanopowders. *J. Phys. Condens. Matter* **19,** 186201 (2007).

63. Klochikhin, A. A., Davydov, V. Y. & Seel', E. R. Compositional fluctuations in isotopic solid solutions. *Phys. Solid State* **49,** 46–54 (2007).

64. Lang, G. *et al.* Anharmonic line shift and linewidth of the Raman mode in covalent semiconductors. *Phys. Rev. B* **59,** 6182–6188 (1999).

65. Burke, H. H. & Herman, I. P. Temperature dependence of Raman scattering in $Ge_{1-x}Si_x$ alloys. *Phys. Rev. B* **48,** 15016–15024 (1993).

66. Klemens, P. G. Anharmonic Decay of Optical Phonons. *Phys. Rev.* **148,** 845–848 (1966).

67. Ridley, B. K. The LO phonon lifetime in GaN. *J. Phys. Condens. Matter* **8,** L511–L513 (1996).

68. Serrano, J. *et al.* Pressure dependence of the lattice dynamics of ZnO: An ab initio approach. *Phys. Rev. B* **69,** 094306 (2004).

69. Barman, S. & Srivastava, G. P. Long-wavelength nonequilibrium optical phonon dynamics in cubic and hexagonal semiconductors. *Phys. Rev. B* **69,** 235208 (2004).

70. Cuscó, R. *et al.* Temperature dependence of Raman scattering in ZnO. *Phys. Rev. B* **75,** 165202 (2007).

71. Ye, J. D. *et al.* Effects of alloying and localized electronic states on the resonant Raman spectra of $Zn_{1-x}Mg_xO$ nanocrystals. *Appl. Phys. Lett.* **91,** 091901 (2007).

72. Feng, Z. C. *Handbook of Zinc Oxide and Related Materials: Volume One, Materials*. (CRC Press, 2012).

73. Han, B., Wessels, B. W. & Ulmer, M. P. Investigation of nanoscale composition fluctuations in InGaN using optical transmission spectroscopy and near-field scanning optical microscopy. *J. Appl. Phys.* **99,** 084312 (2006).

74. Liu, Z. L. *et al.* Alloy fluctuation induced exciton localization in high Mg content ($0.27 \leq x \leq 0.55$) wurtzite $Mg_xZn_{1-x}O$ epilayers. *J. Phys. Appl. Phys.* **43,** 285402 (2010).

75. Chen, J., Shen, W. Z., Chen, N. B., Qiu, D. J. & Wu, H. Z. The study of composition non-uniformity in ternary $Mg_x Zn_{1-x}O$ thin films. *J. Phys. Condens. Matter* **15,** L475–L482 (2003).

76. W Martienssen & Hans Warlimont. *Springer handbook of condensed matter and materials data*. (Springer, 2005).

77. *Table of Periodic Properties of the Elements*. (Sargent Welch Scientific Co, 1979).

78. Taurian, O. E., Springborg, M. & Christensen, N. E. Self-consistent electronic structures of MgO and SrO. *Solid State Commun.* **55,** 351–355 (1985).

Chapter 5 Lattice mismatched ZnS_xO_{1-x} alloys: Toward the realization of a new alloy functional in the visible range

While theoretical and experimental work has been done on cations-substituted zinc oxide (ZnO) based ternary alloys such as $Mg_xZn_{1-x}O$[1–4], reports on anionic substitutions in ZnO is scarce. Among different choices of anions-substituted ZnO alloys, ZnS_xO_{1-x} is a promising material due to its potential in band gap engineering ranging from the UV to the visible region. In this chapter we present the key points relating to ZnS_xO_{1-x} alloy systems, and, the guidelines for future research.

5.1 Overview of ZnS_xO_{1-x} alloys

Like ZnO, ZnS is also a chemically benign compound. It can be found in nature as the mineral sphalerite and is widely used as a pigment. Additionally, ZnS can be produced at low cost using waste materials such as smelters and slag[5]. While both ZnO and ZnS have band gaps in the UV range, 3.2 eV and 3.54 eV[6] respectively, a significant band gap bowing effect allows the band gap energy of ZnS_xO_{1-x} alloys to reach well into the visible range.

As mentioned in Chapter 1, the band gap of a ZnS_xO_{1-x} alloy has the form[7–9]

$$E_{g\ ZnS_xO_{1-x}} = x E_{g\ ZnS} + (1-x) E_{g\ ZnO} - b_{ZnS_xO_{1-x}}\, x\,(1-x) \tag{5.1}$$

where x is the alloy composition, and, b is known as the bowing parameter which describes the deviation of the alloy's band gap from a linear interpolation. In a ZnS_xO_{1-x} alloy system, the mismatch in the electronegativity and in the covalent radius between oxygen (O) and sulfur (S) atoms, as listed in Table 5.1, lead to a strong competition between anions in trapping electrons and thus the bowing parameter $b_{ZnS_xO_{1-x}}$ exhibits a strong alloy

composition dependence [8,10]. The theoretical calculation and experimental work conducted by Moon et al.[8] and by Persson et al.[11], respectively, concluded the band gaps of ZnS_xO_{1-x} alloys with different S compositions as shown in Figure 5.1 (b). Persson et al. attributed the band gap bowing effect to the valence band offset in a ZnS_xO_{1-x} alloy system[11], as illustrated in Figure 5.1 (a). Specifically, for S compositions $x \leq 0.5$, the valence band of ZnS_xO_{1-x} moved toward a higher energy relative to the valence band of ZnO by up to 0.82 eV, while the conduction band remained nearly the same. Once the S composition exceeds x=0.5, the conduction band of the ZnS_xO_{1-x} alloy begins to rise rapidly until it reaches the level of ZnS while the valence band remains nearly the same. Therefore band gap bowing appears as a net effect.

Atom	Covalent Radius (Å)	Electronegativity (Pauling)	Oxidation States
Zn	1.25	1.65	+2
O	0.73	3.44	-2
S	1.02	2.58	±2, +4, +6

Table 5.1: Selective atomic properties of Zn, S, and, O. The mismatch in size and electronegativity between O and S leads to a large bowing parameter in the ZnS_xO_{1-x} system. Various oxidation states of S increases the difficulty of synthesizing high quality ZnS_xO_{1-x} alloys.

Compound	Crystal Structure	Lattice Constant[6] (Å)	Band Gap[6] (eV)	Vapor Pressure (Torr)
ZnO	Wurtzite	a=3.2, c=5.2	3.2	13×10^{-3} at 849 K[12]
ZnS	Cubic Zinc blende Hexagonal Wurtzite*	a=5.4 a=3.82, c=6.26	3.54 3.67	2870 at 823 K[13]

Table 5.2: Selective material properties of ZnO and ZnS.

* The hexagonal wurtzite phase is a less stable form of ZnS. The transition from the zinc-blende form to the wurtzite form occurs at approximately 1020 ºC.

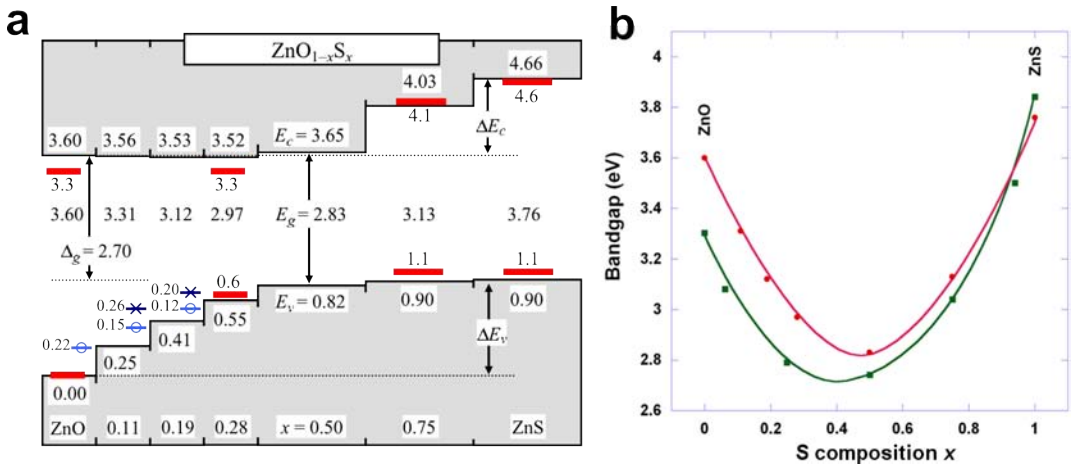

Figure 5.1: ***(a)****Theoretical calculations conducted by Persson et al*[11]*. shows the S composition dependent valence band offset in* ZnS_xO_{1-x} *alloys. Plot from Persson et al*[11]*.* ***(b)****Band gaps of* ZnS_xO_{1-x} *alloy as theoretically predicted by Moon et al.*[8] *(green squares) and experimentally obtained by Persson et al.*[11] *from* ZnS_xO_{1-x} *films grown via atomic layer deposition (red circles).*

With such band gap bowing, ZnS_xO_{1-x} alloys can achieve a wide band gap modulation into the visible region with a low fraction of S. Therefore ZnS_xO_{1-x} is considered as a potential alternate of ZnCdO in solid state visible laser applications, in order to eliminate the use of highly toxic material CdO[3]. Moreover, in photovoltaic devices, ZnS_xO_{1-x} buffer layers can enhance the conversion efficiency of Cu(In, Ga)Se_2 based solar cells[14]. These applications call for ZnS_xO_{1-x} alloys with tailored band gaps and good performances, which inspired an interest in synthesizing high quality ZnS_xO_{1-x} materials and investigating their structural and optical properties.

In spite of their attracting characteristics, successful alloying ZnS with ZnO is not a trivial task. First of all, the two end members have different crystal lattice structures (see Table 5.2) and the solubility limit of ZnS in ZnO and of ZnO in ZnS under thermodynamically equilibrium conditions are both low. Locmelis et al. reported the

solubility limits at each end as $0<x\leq0.05$ and $0.96\leq x<1$, respectively, for ZnS_xO_{1-x} single crystals grown under a thermodynamically equilibrium condition [15]. However, non-equilibrium material growth methods can be employed to fabricate metastable ZnS_xO_{1-x} alloys with expanded ranges of the alloy composition. Yoo et al achieved ZnS_xO_{1-x} films with $0<x<0.15$ via pulsed laser deposition[16]. Platzer et al. reported ultra thin ZnS_xO_{1-x} layers grown by atomic layer deposition with *x* reaching approximately 0.8~0.9 [14]. With reactive sputtering, Meyer et al. managed to synthesis wurtzite structured ZnS_xO_{1-x} films with an S composition extended covering the full range of $0\leq x\leq1$[17].

Another difficulty in the alloying process is the significant difference between the stability of ZnS and ZnO at the material growth temperature[8,18]. The synthesis of ZnO films usually requires a high growth temperature above 250 °C in order to achieve high crystal qualities. However, ZnS does not endure high temperature as ZnO does. The vapor pressure of ZnS is much higher than that of ZnO (see Table 5.2), which leads to the dissociation and evaporation of ZnS at common growth temperatures for ZnO. Significant material loss due to evaporation was observed in the growth of ZnS films at 340 °C[19]. Furthermore, sulfur has several oxidation states other than the S^{2-} state as in ZnS (see Table 5.1) and thus it is possible that sulfur form intermediate phases such as $ZnSO_4$ during the growth process. Therefore, a precise growth technique is needed in order to achieve ZnS_xO_{1-x} alloys with high crystal qualities and desirable S contents.

5.2 The synthesis of ZnS_xO_{1-x} thin films

The ZnS_xO_{1-x} films were grown on c-plane quartz substrates and Fluorinated Ethylene Propylene (FEP) substrates via RF magnetron sputtering using a ceramic ZnS (99.99%)

target and argon as the sputtering gas. The sputtering power was 30 Watt. During the film growth process, oxygen flow was introduced into the sputtering chamber under the precise control by a mass flow controller. With the controlled amount of oxygen in the chamber, part of sputtered ZnS clusters were oxidized on their path toward the substrate following the reaction of

$$2\,ZnS(s)+3\,O_2(g)\Rightarrow 2\,ZnO(s)+2\,SO_2(g) \tag{5.2}$$

The solid reaction product, ZnO, was deposited onto the substrate while the gaseous SO_2 was taken out of the chamber by the pumping system. Meanwhile, the rest of sputtered ZnS clusters landed on the substrate without being oxidized. The mixture of ZnS-ZnO deposited on the substrate went through diffusion and crystallization at an elevated temperature up to 250 ºC and as a result uniform ZnS_xO_{1-x} films were achieved.

Quartz was chosen as the substrate for its high transparency in the UV and visible region, as mentioned in Chapter 4. However, for the ZnS_xO_{1-x} films grown on quartz, the accurate ratio between O and S content was difficult to evaluate by energy dispersive spectroscopy (EDS), due to the overlapping of the O signal from the substrates. To avoid this issue, the voltage of the primary beam electrons in EDS was decreased in order to reduce the penetration depth of the electrons and thus avoid detecting O signals from the substrates. Following this approach enables the acquisition of meaningful EDS data for this work. On the other hand, using FEP as substrates eliminates the issue of O overlapping since FEP contains only carbon and fluorine. FEP displays a high transparency from the visible to the UV range. FEP also exhibits many desirable properties such as low coefficients of friction, resistance to chemical attack, heat sealability and high melting points. These material properties make FEP an excellent choice as a substrate or capping layer for UV optical

devices. Moreover, using FEP substrates for the ZnS_xO_{1-x} films has potential application in flexible electronics and films[20].

Figure 5.2 (a) and (b) show SEM images of the $ZnS_{0.28}O_{0.92}$ film grown on quartz and the $ZnS_{0.16}O_{0.84}$ film grown on FEP, respectively. Both films have polycrystalline morphologies. The inset in Figure 5.2 (b) is a photograph of the $ZnS_{0.16}O_{0.84}$ film grown on FEP, showing its transparency and flexibility.

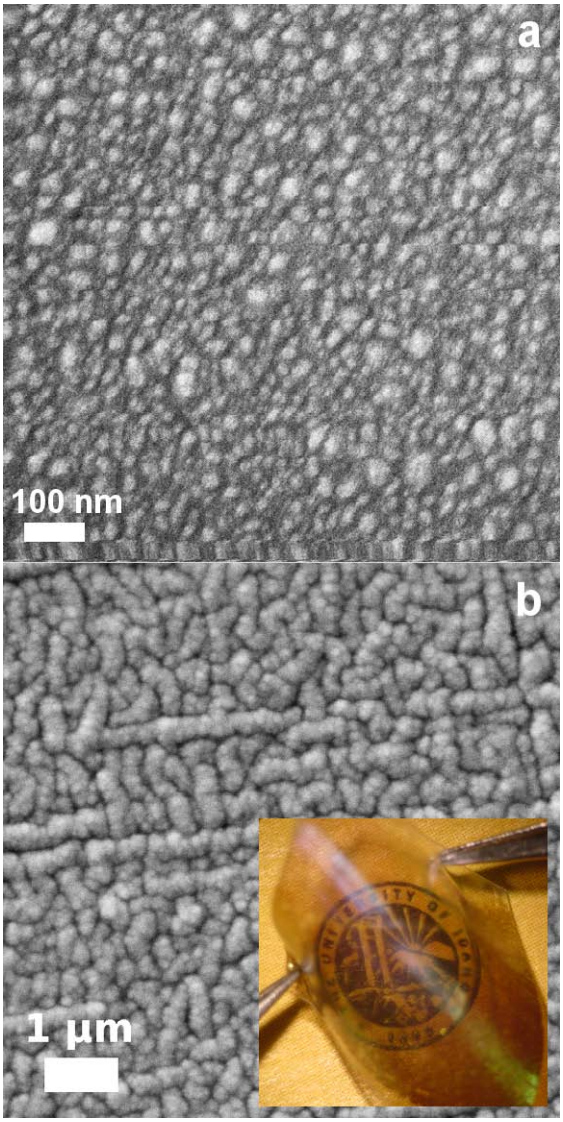

Figure 5.2: SEM images of ***a)*** *$ZnS_{0.28}O_{0.92}$ film grown on quartz substrate and* ***b)*** *$ZnS_{0.16}O_{0.84}$ film grown on FEP substrate. Both films show polycrystalline morphologies. The inset photo shows the flexibility of the ZnS_xO_{1-x} films grown on FEP.*

5.3 Bandgap analysis of ZnS_xO_{1-x} thin films

Optical transmission spectra of the ZnS_xO_{1-x} films grown for this work were acquired and the band gaps of the films were determined following the inflection point analysis method introduced in Chapter 3. Figure 5.3 (a) and (b) present the measured transmittance in films grown on quartz and FEP substrates, respectively. Figure 5.3 (c) and (d) present the corresponding extrapolation of band gaps via the inflection point analysis. The values of band gaps are summarized in Figure 5.4 and superimposed with theoretically calculation results by Moon et al.[8] and experimental data reported by Persson et al.[11]. As can be seen in Figure 5.4, for S compositions $0 \leq x < 0.20$ a band gap reduction from approximately 3.3 eV to 2.9 eV was achieved, which agrees well with the theoretical prediction[8] and previously reported experimental results[11]. However, in the vicinity of $x=0.20$ a diversion from the theoretical trend exhibited. Especially the $ZnS_{0.28}O_{0.72}$ film has a band gap of 2.5 eV, which is significantly lower than expected.

Such diversion of the band gaps from theory suggests possible defect energy levels emerging in ZnS_xO_{1-x} alloys with alloy composition $x>0.20$. Due to the high tendency of ZnS evaporation as mentioned in the previous section, the substrate temperature was decreased in order to achieve higher S contents in ZnS_xO_{1-x} alloy films. The relatively low growth temperature impeded the crystallization and strains relaxation during the film growth and therefore energy levels reside within the band gap were introduced by structural defects and lattice strains.

On the other hand, considering the common oxidation states of sulfur, S^{6+}, the formation of $-SO_4$ compounds might serve as another contributor to the defect energy states. Further investigations in identifying possible different forms of sulfur compound is needed in order

to gain a better knowledge of the alloying dynamics in ZnS_xO_{1-x} alloy systems.

The synthesis of high quality ZnS_xO_{1-x} alloys with tailored band gap is subject to the growth technique which is sensitive to multiple growth parameters such as the substrate temperature, the oxygen flow, the chamber's working pressure, and even the time of growth. A delicate balance needs to be drawn among all growth parameters in order to achieve the optimum growth condition.

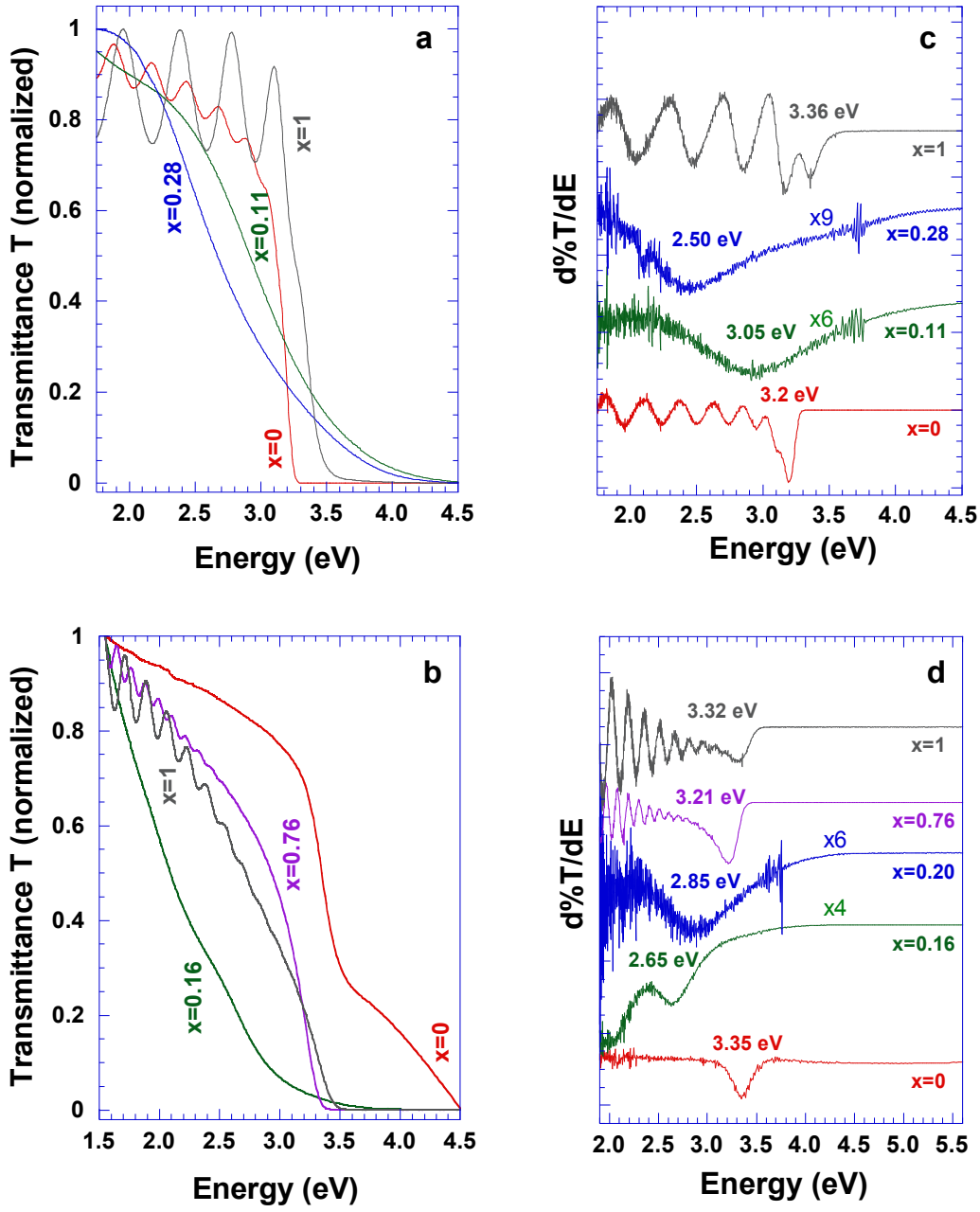

*Figure 5.3: Transmittance of representative ZnS_xO_{1-x} films grown on **a)** quartz and **b)** FEP substrates. A shift of the absorption edge toward the lower energy with respect to the S composition was observed in films grown on both substrates. The derivative method analysis was applied to the transmittance data and values of band gaps were obtained as shown in **c)** and **d)**.*

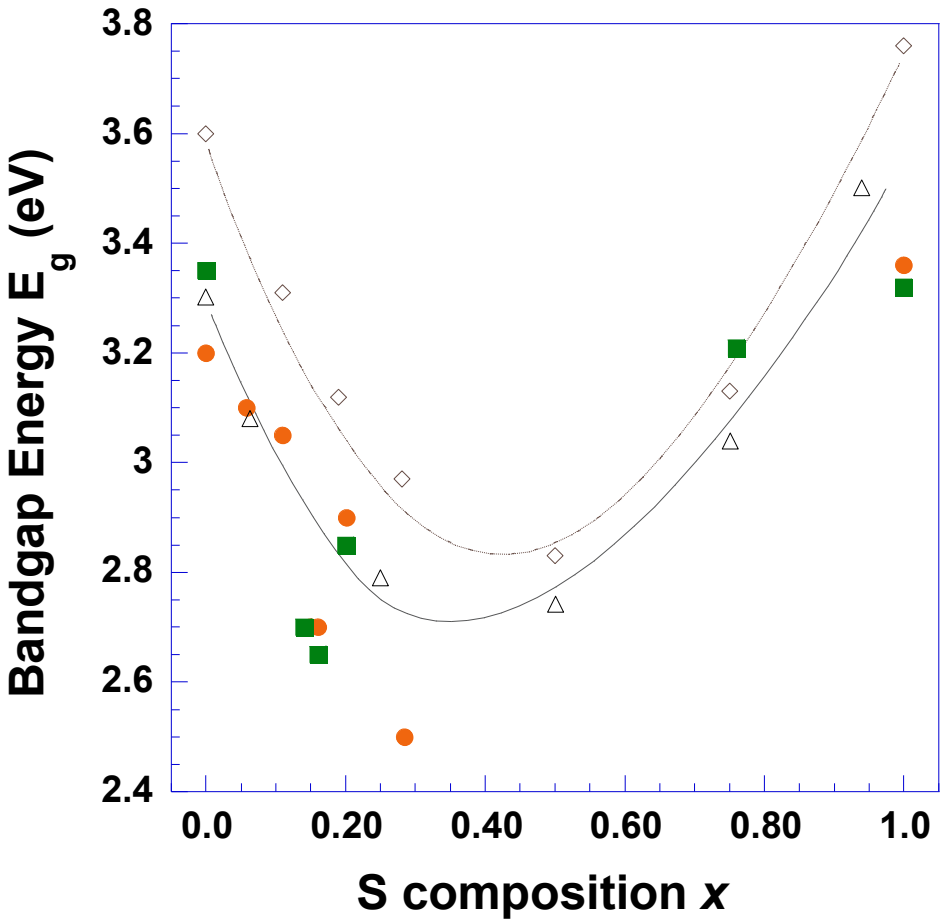

Figure 5.4: A summary of the band gap values of the ZnS_xO_{1-x} films grown on quartz substrates (solid circles) and on FEP substrates (solid squares) for this work. Theoretical calculation results reported by Moon et al[8] (open triangles) and experimental results by Persson et al.[11] (open diamonds) are presented as references. The curves are guides to the eye.

5.4 Future research directions

The present work paved the way for the realization of ZnS_xO_{1-x} alloys functional in the visible range. In order to improve the properties and performance of the alloys for practical applications, more research work need to be carried out in the future.

5.4.1 Improving the synthesis technique

The current magnetron sputtering process utilizes only one sputtering target of pure ZnS and introduces oxygen gas as the reactive agent in order to partially oxidize ZnS and get a mixture of ZnO-ZnS. As discussed in previous sections, finding a balance between multiple growth parameters and achieving the desired degree of partial oxidation is a challenging task. One possible route to bypass such sensitive oxidation process is dual gun sputtering, with a ZnS target and a ZnO target, at the same time. No reactive gas is needed in this configuration. The ratio between S and O composition in an obtained ZnS_xO_{1-x} film can be controlled either by tuning the delivering power of each gun, or by changing the relative distance between the substrate and each gun. One prospective advantage of dual gun sputtering is that by placing multiple substrates along the path between the two sputtering guns, a series of ZnS_xO_{1-x} films with various S compositions can be grown from one single run, which will greatly increase the efficiency of material synthesis.

Another obstacle in the film growth for this work is the residual water vapor in the vacuum chamber. Every time the chamber is exposed to the ambient environment for target changing or maintenance, the highly polar water molecules in the air will instantly get absorbed onto the internal surfaces of the chamber and the elastomer O-rings. Most of the volume gas in a vacuum chamber is pumped away when the chamber is pumped to a pressure

of 10^{-3} torr or below, leaving water vapor the predominant gas within the chamber[21]. During the growth of ZnS_xO_{1-x}, water vapor reacts with ZnS following the process[22],

$$ZnS(s)+H_2O(g)\Rightarrow ZnO(s)+H_2S(g) \tag{5.3}$$

which makes makes the degree of partial oxidation of ZnS harder to control. These water molecules cling to the inner surfaces of the chamber with weak bonds and can not be pumped away until they gain enough energy to break the bonds and leave the surface. Some practical solutions to the residual water vapor issue include heating the chamber and bombarding the inner surfaces with UV radiation[21]. Both methods provide the water molecules clinging on the inner surfaces with enough energy so that they can break off from the surfaces and eventually be pumped away.

5.4.2 Alloying dynamics in the ZnS_xO_{1-x} system

As mentioned in Section 5.3, the variety in oxidation states of sulfur brings complexity to the alloying dynamics in the ZnS_xO_{1-x} alloy system. Sulfur might take its most common S^{6+} state and form $ZnSO_4$, instead of the desired S^{-2} state for ZnS_xO_{1-x} alloys. X-ray photoelectron spectroscopy (XPS) can be utilized to identify different forms of sulfur in the alloy systems. By irradiating a material with a beam of X-tays while at the same time measuring the number of electrons that escape from the surface of the material and their kinetic energies, XPS spectra give information of the chemical states of a certain element in a material and their relative compositions. The investigation into the chemical states of sulfur will help with understanding the origins of defect energy states within the band gap and then improve the growth conditions accordingly.

5.4.3 Temperature dependent transmission measurement

The optical transmission measurements in this work were all conducted at room temperature. However a lot of characteristics of a material exhibit temperature dependent behavior, such as bandgap[23,24], refractive index, and electron-hole recombination dynamics. Therefore for a certain material, a measurement of its optical absorption process under various temperatures can convey much more information.

Recently an add-on adapter was designed and assembled by our group to accommodate the Instec hot/cold stage in the Cary 300 UV-Vis spectrophotometer so that the real time temperature dependent optical transmission measurement of a material can be carried out. Figure 5.5 shows the assembly of the customize adapter. The Instec hit/cold stage is mounted on a 3-axis positioner held by a rotational stage. Such design enables precision spacial and angular adjustment of the sample position within the limited space in the spectrophotometer's sample cell so that the sample being examined can be impinged at the light beam's focal point perpendicularly.

With this assembly it will be possible to perform in situ optical transmission measurement at various temperatures from 77 K to 873 K. Which enables the studies of the temperature dependent behavior of absorption coefficient[25], optical bandgap[26], and, Urbach energy[27]. Furthermore, transmission spectra obtained at low temperature can reveal the exciton related optical absorption process and thus study the excitonic structure in a bandgap[28,29]. A new horizon of research is waiting to be explored.

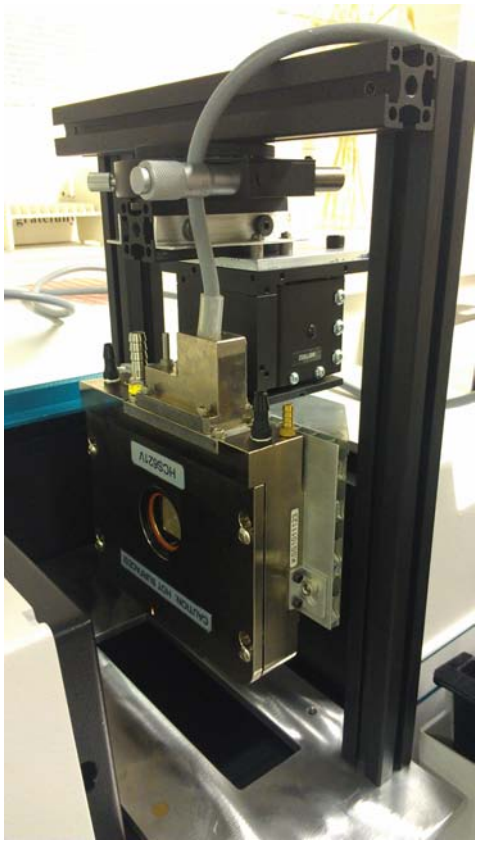

Figure 5.5: The setup of the customize designed and assembled adapter. The Instec hit/cold stage is mounted on a 3-axis positioner held by a rotational stage, allowing precision spacial and angular adjustment of the sample position within the limited space in the spectrophotometer's sample cell. With this setup a real time optical transmission measurement at temperatures from 77K to 873K is possible.

5.4.4 More possibilities of ZnO based alloys for tailored band gaps

Aside from the ZnS_xO_{1-x} alloys, there are other options of alloys for achieving a band gap energy down to the region of visible light. Substituting Zn^{2+} in ZnO lattices with Mn^{2+}, Co^{2+}, and, Ni^{2+} are all found to be able to decrease the band gap of ZnO[30]. Moreover, with the double gun configuration of the sputtering system and sputtering targets with proper

compositions, the creation of quaternary alloys will be achievable and it might stimulate a new line of research.

5.5 Conclusion

ZnS_xO_{1-x} alloy films grown on quartz and flexible FEP substrates were successfully achieved via reactive RF sputtering with delicate control of the growth conditions.

For the ZnS_xO_{1-x} alloy films, a band gap reduction from approximately 3.3 eV to 2.9 eV was achieved with S compositions $0 \leq x < 0.20$. This result agrees well with the theoretical and experimental data previously reported. However, the $ZnS_{0.28}O_{0.72}$ film has a band gap of 2.5 eV, which is significantly lower than expected. Such diversion of the band gaps from the theoretical prediction suggests defect energy levels emerging in ZnS_xO_{1-x} alloys with alloy composition $x > 0.20$. Relatively low substrate temperatures were employed during growth in order to avoid the ZnS evaporation and achieve higher S contents in ZnS_xO_{1-x} alloy films. The lack of thermal energy for crystallization and strains relaxation generated structural defects and lattice strains which caused energy levels within the band gap. Moreover, the variety in S oxidation states may lead to the formation of $-SO_4$ compounds and serve as another origin of the defect energy states.

Future research work will focus on the optimization of growth techniques for synthesizing ZnS_xO_{1-x} alloys with higher crystal qualities and more precisely controlled alloy compositions; Investigation the alloying dynamics in ZnS_xO_{1-x} alloy systems; Expanding the abilities of material characterization techniques, and, exploring other possible choices for ZnO based alloys.

5.6 References

1. Ohtomo, A. *et al.* $Mg_xZn_{1-x}O$ as a II–VI widegap semiconductor alloy. *Appl. Phys. Lett.* **72,** 2466–2468 (1998).

2. Chen, J., Shen, W. Z., Chen, N. B., Qiu, D. J. & Wu, H. Z. The study of composition non-uniformity in ternary $Mg_xZn_{1-x}O$ thin films. *J. Phys. Condens. Matter* **15,** L475–L482 (2003).

3. Makino, T. *et al.* Band gap engineering based on $Mg_xZn_{1-x}O$ and $Cd_yZn_{1-y}O$ ternary alloy films. *Appl. Phys. Lett.* **78,** 1237–1239 (2001).

4. Chen, J. & Shen, W. Z. Long-wavelength optical phonon properties of ternary MgZnO thin films. *Appl. Phys. Lett.* **83,** 2154–2156 (2003).

5. Auer, G. *et al.* in *Ullmanns Encycl. Ind. Chem.* (Wiley-VCH Verlag GmbH & Co. KGaA, 2000).

6. W Martienssen & Hans Warlimont. *Springer handbook of condensed matter and materials data*. (Springer, 2005).

7. Richardson, D. & Hill, R. The origins of energy gap bowings in substitutional semiconductor alloys. *J. Phys. C Solid State Phys.* **5,** 821 (1972).

8. Moon, C.-Y., Wei, S.-H., Zhu, Y. Z. & Chen, G. D. Band-gap bowing coefficients in large size-mismatched II-VI alloys: first-principles calculations. *Phys. Rev. B* **74,** 233202 (2006).

9. Tit, N., Dagher, S., Ayesh, A. & Haik, Y. Bowing Character in Wurtzite ZnO-Based Ternary Alloys. *J. Electron. Mater.* **41,** 3111–3118 (2012).

10. Wei, S.-H. & Zunger, A. Giant and Composition-Dependent Optical Bowing Coefficient in GaAsN Alloys. *Phys. Rev. Lett.* **76,** 664–667 (1996).

11. Persson, C., Platzer-Björkman, C., Malmström, J., Törndahl, T. & Edoff, M. Strong Valence-Band Offset Bowing of $ZnO_{1-x}S_x$ Enhances p-Type Nitrogen Doping of ZnO-like Alloys. *Phys. Rev. Lett.* **97,** 146403 (2006).

12. Anthrop, D. F. & Searcy, A. W. Sublimation and Thermodynamic Properties of Zinc Oxide. *J. Phys. Chem.* **68,** 2335–2342 (1964).

13. West, W. A. & Menzies, A. W. C. The Vapor Pressures of Sulphur between 100° and 550°

with related Thermal Data. *J. Phys. Chem.* **33,** 1880–1892 (1928).

14. Platzer-Björkman, C. *et al.* Zn(O,S) buffer layers by atomic layer deposition in $Cu(In,Ga)Se_2$ based thin film solar cells: Band alignment and sulfur gradient. *J. Appl. Phys.* **100,** 044506 (2006).

15. Locmelis, S. *et al.* Optical band gap in the system $ZnO_{1-x}S_x$. An experimental and quantum chemical study. *J. Mater. Sci.* **42,** 1965–1971 (2007).

16. Yoo, Y.-Z. *et al.* S doping in ZnO film by supplying ZnS species with pulsed-laser-deposition method. *Appl. Phys. Lett.* **81,** 3798–3800 (2002).

17. Meyer, B. K. *et al.* Structural properties and bandgap bowing of $ZnO_{1-x}S_x$ thin films deposited by reactive sputtering. *Appl. Phys. Lett.* **85,** 4929–4931 (2004).

18. Fan, X. F., Shen, Z. X., Lu, Y. M. & Kuo, J.-L. A theoretical study of thermal stability and electronic properties of wurtzite and zincblende ZnO_xS_{1-x}. *New J. Phys.* **11,** 093008 (2009).

19. Subbaiah, Y. P. V., Prathap, P. & Reddy, K. T. R. Structural, electrical and optical properties of ZnS films deposited by close-spaced evaporation. *Appl. Surf. Sci.* **253,** 2409–2415 (2006).

20. Huso, J., Morrison, John L, Che, H., Sundararajan, Jency P, Yeh, W. J., McIlroy, David, Williams, Thomas J & Bergman, L. ZnO and MgZnO Nanocrystalline Flexible Films: Optical and Material Properties. *J. Nanomater. J. Nanomater.* **2011,** 1–7 (2011).

21. Danielson, P. Reduce Water Vapor in Vacuum Systems. *RD Mag.* **42,** 10 (2000).

22. Kryshtab, T. *et al.* Luminescence and structure of ZnO–ZnS thin films prepared by oxidation of ZnS films in air and water vapor. *J. Lumin.* **129,** 1677–1681 (2009).

23. Bhosale, J. *et al.* Temperature dependence of band gaps in semiconductors: Electron-phonon interaction. *Phys. Rev. B* **86,** 195208 (2012).

24. O'Donnell, K. P. & Chen, X. Temperature dependence of semiconductor band gaps. *Appl. Phys. Lett.* **58,** 2924–2926 (1991).

25. Kovalev, D., Polisski, G., Ben-Chorin, M., Diener, J. & Koch, F. The temperature dependence of the absorption coefficient of porous silicon. *J. Appl. Phys.* **80,** 5978–5983 (1996).

26. Kwack, H.-S., Sun, Y., Cho, Y.-H., Park, N.-M. & Park, S.-J. Anomalous temperature

dependence of optical emission in visible-light-emitting amorphous silicon quantum dots. *Appl. Phys. Lett.* **83,** 2901–2903 (2003).

27. Rai, R. C. Analysis of the Urbach tails in absorption spectra of undoped ZnO thin films. *J. Appl. Phys.* **113,** 153508–153508–5 (2013).

28. Müller, A., Benndorf, G., Heitsch, S., Sturm, C. & Grundmann, M. Exciton–phonon coupling and exciton thermalization in $Mg_xZn_{1-x}O$ thin films. *Solid State Commun.* **148,** 570–572 (2008).

29. Muth, J. F., Kolbas, R. M., Sharma, A. K., Oktyabrsky, S. & Narayan, J. Excitonic structure and absorption coefficient measurements of ZnO single crystal epitaxial films deposited by pulsed laser deposition. *J. Appl. Phys.* **85,** 7884–7887 (1999).

30. Bhat, S. V. & Deepak, F. L. Tuning the bandgap of ZnO by substitution with Mn^{2+}, Co^{2+} and Ni^{2+}. *Solid State Commun.* **135,** 345–347 (2005).

Appendix

The derivative analysis method under more comprehensive circumstances

All approaches discussed in Section 3.1, Chapter 3 are based on the approximation of

$$I = I_0 e^{-\alpha t} \tag{1}$$

which defines the absorption coefficient α without considering the reflecting effect on the sample-air interface and the internal reflection within the sample. However, if we take the sample's reflectivity, which is energy dependent, into consideration for a higher degree of accuracy, the term $\alpha^2(E)^2$ is no longer directly proportional to the term $(E - E_g)$. Therefore, a plot of $\alpha^2 E^2$ versus E will not be linear and all the linear fitting approaches introduced previously are no longer applicable.

While all the linear extrapolation methods becoming invalid, the first order derivative approach remains its accuracy in determining the band gap energy with the factor of reflection taken into consideration. The proof is as following.

Considering reflection and transmission occurring on both the air-film interface and the film-substrate interfaces along with the multiple internal reflections occurring within the thin film, the transmission T through a film can be described as[1]

$$T = \frac{(1-R)^2 e^{-\alpha t}}{1 - R^2 e^{-2\alpha t}} \tag{2}$$

Where R is the Sample's reflectivity; α is its absorption coefficient; and t is its thickness. For the films studied in this work the order of magnitude of the quantity αt is $10^{-3} \sim 1$, which makes the term $e^{-2\alpha t}$ negligible and thus the denominator of this equation can be estimated as 1. We can now rewrite this equation as[1]

$$T=(1-R)^2 e^{-\alpha(E)t} \tag{3}$$

Then take the first order derivative of $\ln T$ with respect to energy *E,*

$$\frac{dT}{dE}=2(R-1)\left(\frac{dR}{dE}\right)\cdot e^{-\alpha(E)\cdot t}+(1-R)^2\cdot e^{-\alpha(E)\cdot t}\cdot\left(\frac{-d\alpha(E)}{dE}\right) \tag{4}$$

Now we investigate this function's behavior when the energy is approaching the value of band gap E_g ,

$$\lim_{E\to E_g}\frac{dT}{dE}=\lim_{E\to E_g}\left[2(R-1)\left(\frac{dR}{dE}\right)\cdot e^{-\alpha(E)\cdot t}\right]+\lim_{E\to E_g}\left[(1-R)^2\cdot e^{-\alpha(E)\cdot t}\cdot\left(\frac{-d\alpha(E)}{dE}\right)\right] \tag{5}$$

Let us start with the first part of Equation 5:

$$\lim_{E\to E_g}\left[2(R-1)\left(\frac{dR}{dE}\right)\cdot e^{-\alpha(E)\cdot t}\right]=\lim_{E\to E_g}\left[2e^{(-\alpha(E)\cdot t)}\right]\cdot\lim_{E\to E_g}\left[(R-1)\cdot\left(\frac{dR}{dE}\right)\right] \tag{6}$$

Since $\lim_{E\to E_g}\left[2e^{(-\alpha(E)\cdot t)}\right]$ is a constant, the term $\lim_{E\to E_g}\left[(R-1)\cdot\left(\frac{dR}{dE}\right)\right]$ will determine the behavior of Equation 6.

For the circumstance of normal incidence, which is the case in the transmission measurement performed in this study, the sample film's reflection coefficient *R* is given by[1]

$$R=\frac{(n-1)^2+k^2}{(n+1)^2+k^2} \tag{7}$$

Where *n* and *k* is the real and imaginary part of the refractive index of the material, respectively, and both of them are energy dependent. The extinction coefficient *k* can be written as $k=\frac{\alpha(E)\cdot\lambda}{4\pi}$. Converting the wavelength λ to energy E , it becomes $k=A^{*}\cdot\frac{\alpha(E)}{E}$, where $A^{*}=\frac{1240}{4\pi}$.

Therefore the reflectance can be written as a function of energy as

$$R=\frac{(n-1)^2+A^{*2}\cdot\frac{\alpha^2(E)}{E^2}}{(n+1)^2+A^{*2}\cdot\frac{\alpha^2(E)}{E^2}}=\frac{(n-1)^2E^2+A^{*2}\alpha^2(E)}{(n+1)^2E^2+A^{*2}\alpha^2(E)} \tag{8}$$

Now the behavior of $\left(\frac{dR}{dE}\right)$ can be investigated.

According to Equation 8,

$$\frac{dR}{dE}=\frac{I.-II.}{III.} \tag{9}$$

Where

$$\begin{aligned} I. &= \frac{d\left[(n-1)^2E^2+A^{*2}\alpha^2(E)\right]}{dE}\cdot\left[(n+1)^2E^2+A^{*2}\alpha^2(E)\right] \\ II. &= \frac{d\left[(n+1)^2E^2+A^{*2}\alpha^2(E)\right]}{dE}\cdot\left[(n-1)^2E^2+A^{*2}\alpha^2(E)\right] \\ III. &= \left[(n+1)^2\cdot E^2+A^{*2}\cdot\alpha^2(E)\right]^2 \end{aligned} \tag{10}$$

Solve for each part individually then combine the results,

$$\frac{dR}{dE}=\frac{4E^2\cdot\left[E^2\cdot\left(n^2(E)-1\right)-A^{*2}\cdot\alpha^2(E)\right]\cdot\frac{dn(E)}{dE}}{\left[(n+1)^2\cdot E^2+A^{*2}\cdot\alpha^2(E)\right]^2}$$
$$+\frac{8A^{*2}\cdot E^2\cdot n(E)\cdot\alpha(E)\cdot\frac{d\alpha(E)}{dE}}{\left[(n+1)^2\cdot E^2+A^{*2}\cdot\alpha^2(E)\right]^2} \tag{11}$$
$$-\frac{8A^{*2}\cdot E\cdot n(E)\cdot\alpha^2(E)}{\left[(n+1)^2\cdot E^2+A^{*2}\cdot\alpha^2(E)\right]^2}$$

Therefore,

$$\lim_{E\to E_g}\left[(R-1)\cdot\left(\frac{dR}{dE}\right)\right]=$$
$$\lim_{E\to E_g}\left\{\frac{-16\cdot E^4\cdot n(E)\cdot[E^2\cdot\left(n^2(E)-1\right)-A^{*2}\cdot\alpha^2(E)]}{\left[\left(n(E)+1\right)^2\cdot E^2+A^{*2}\cdot\alpha^2(E)\right]^3}\cdot\frac{dn(E)}{dE}\right\}$$
$$-\lim_{E\to E_g}\left\{\frac{32\cdot E^4\cdot A^{*2}\cdot n^2(E)\cdot\alpha(E)}{\left[\left(n(E)+1\right)^2\cdot E^2+A^{*2}\cdot\alpha^2(E)\right]^3}\cdot\frac{d\alpha(E)}{dE}\right\} \tag{12}$$
$$+\lim_{E\to E_g}\left\{\frac{32\cdot E^3\cdot A^{*2}\cdot n^2(E)\cdot\alpha^2(E)}{\left[\left(n(E)+1\right)^2\cdot E^2+A^{*2}\cdot\alpha^2(E)\right]^3}\right\}$$

In equation 12, the first term

$$\lim_{E\to E_g}\left\{\frac{-16\cdot E^4\cdot n(E)\cdot[E^2\cdot(n^2(E)-1)-A^{\prime 2}\cdot\alpha^2(E)]}{\left[(n(E)+1)^2\cdot E^2+A^{\prime 2}\cdot\alpha^2(E)\right]^3}\cdot\frac{dn(E)}{dE}\right\}$$
$$=\frac{-16\cdot {E_g}^4\cdot n(E_g)\cdot[{E_g}^2\cdot(n^2(E_g)-1)-A^{\prime 2}\cdot\alpha^2(E_g)]}{\left[(n(E_g)+1)^2\cdot {E_g}^2+A^{\prime 2}\cdot\alpha^2(E_g)\right]^3}\cdot\lim_{E\to E_g}\left[\frac{dn(E)}{dE}\right] \tag{13}$$

turns out as a finite value since there is no singularity in $\frac{dn(E)}{dE}$ at the energy of band gap in a realistic model[2].

To investigate the second term in Equation 12, the model of absorption coefficient $\alpha(E)$ [3] is taken again

$$\alpha=\frac{8}{3}\beta a_H^2\left(\frac{R_H}{E}\right)\frac{1}{\eta_r}\frac{p_{cv}^2}{2\mathrm{m}}\left(\frac{2m_r^{\prime}}{\hbar^2}\right)^{\frac{3}{2}}(E-E_g)^{\frac{1}{2}}=B^*\cdot E^{-1}\cdot\eta_r^{-1}(E)\cdot(E-E_g)^{\frac{1}{2}} \tag{14}$$

where $B^*=\frac{8}{3}\beta a_H^2 R_H\frac{p_{cv}^2}{2\mathrm{m}}\left(\frac{2m_r^*}{\hbar^2}\right)^{\frac{3}{2}}$ is a constant.

Then

$$\lim_{E\to E_g}\left\{\frac{32\cdot E^4\cdot A^{*2}\cdot n^2(E)\cdot\alpha(E)}{\left[(n(E)+1)^2\cdot E^2+A^{*2}\cdot\alpha^2(E)\right]^3}\cdot\frac{d\alpha(E)}{dE}\right\}$$
$$=\frac{32\cdot {E_g}^4\cdot A^{*2}\cdot n^2(E_g)\cdot B^*\cdot {E_g}^{-1}\cdot\eta_r^{-1}(E_g)}{\left[(n(E_g)+1)^2\cdot {E_g}^2+0\right]}\cdot(0+0+1) \tag{15}$$
$$=\frac{32\cdot {E_g}^4\cdot A^{*2}\cdot n^2(E_g)\cdot B^*\cdot {E_g}^{-1}\cdot\eta_r^{-1}(E_g)}{(n(E_g)+1)^2\cdot {E_g}^2}$$

which is a finite constant.

Similarly, for the third term of Equation 12,

$$\lim_{E\to E_g}\left\{\frac{32\cdot E^3\cdot A^{*2}\cdot n^2(E)\cdot\alpha^2(E)}{\left[\left(n(E)+1\right)^2\cdot E^2+A^{*2}\cdot\alpha^2(E)\right]^3}\right\}=0 \tag{16}$$

Therefore, the factor originated from the reflectance at the interfaces between different media is solved as

$$\begin{aligned}&\lim_{E\to E_g}\left[(R-1)\cdot\left(\frac{dR}{dE}\right)\right]\\&=\frac{-16\cdot {E_g}^4\cdot n(E_g)\cdot[{E_g}^2\cdot\left(n^2(E_g)-1\right)-A^{*2}\cdot\alpha^2(E_g)]}{\left[\left(n(E_g)+1\right)^2\cdot {E_g}^2+A^{*2}\cdot\alpha^2(E_g)\right]^3}\\&\cdot\lim_{E\to E_g}\left[\frac{dn(E)}{dE}\right]-\frac{32\cdot {E_g}^4\cdot A^{*2}\cdot n^2(E_g)\cdot B^*\cdot {E_g}^{-1}\cdot {\eta_r}^{-1}(E_g)}{\left(n(E_g)+1\right)^2\cdot {E_g}^2}\end{aligned} \tag{17}$$

which was proved to be a finite constant.

Consequently, for $\lim_{E\to E_g}\frac{dT}{dE}$, we conclude that the first part of Equation 5

$$\lim_{E\to E_g}\left[2(R-1)\left(\frac{dR}{dE}\right)\cdot e^{-\alpha(E)\cdot t}\right]=C^* \tag{18}$$

where C^* is a finite constant.

Now proceed to the second part of $\lim_{E\to E_g}\frac{dT}{dE}$ (see Equation 5),

$$\begin{aligned}
&\lim_{E\to E_g}\left[(1-R)^2\cdot e^{-\alpha(E)\cdot t}\cdot\left(\frac{-d\alpha(E)}{dE}\right)\right] \\
&=\lim_{E\to E_g}\left[(1-R)^2\cdot e^{-\alpha(E)\cdot t}\right]\cdot\left[-\lim_{E\to E_g}\left(\frac{d\alpha(E)}{dE}\right)\right] \\
&=\left[\frac{16n^2(E_g)\cdot {E_g}^2}{\left[{E_g}^2\cdot(n(E_g)+1)^2+A^{*2}\cdot\alpha^2(E_g)\right]^2}\right]\cdot\left[-\lim_{E\to E_g}\left(\frac{d\alpha(E)}{dE}\right)\right] \\
&=D^*\cdot\left[-\lim_{E\to E_g}\left(\frac{d\alpha(E)}{dE}\right)\right]
\end{aligned} \tag{19}$$

where $D^*=\left[\frac{16n^2(E_g)\cdot {E_g}^2}{\left[{E_g}^2\cdot(n(E_g)+1)^2+A^{*2}\cdot\alpha^2(E_g)\right]^2}\right]$ is a finite constant.

Finally, $\lim_{E\to E_g}\frac{dT}{dE}$ with the consideration of the factor of reflectance on interfaces between different media is solved as:

$$\begin{aligned}
\lim_{E\to E_g}\frac{dT}{dE}&=\lim_{E\to E_g}\left[2(R-1)\left(\frac{dR}{dE}\right)\cdot e^{-\alpha(E)\cdot t}\right]+\lim_{E\to E_g}\left[(1-R)^2\cdot e^{-\alpha(E)\cdot t}\cdot\left(\frac{-d\alpha(E)}{dE}\right)\right] \\
&=C^*+D^*\cdot\left[-\lim_{E\to E_g}\left(\frac{d\alpha(E)}{dE}\right)\right]
\end{aligned} \tag{20}$$

When the incident phonon energy is approaching the value of bandgap energy E_g, the term

$\lim_{E\to E_g}\left(\frac{d\alpha(E)}{dE}\right)\to+\infty$ as has been proved in the previous section. Therefore we can safely conclude that $\lim_{E\to E_g}\frac{dT}{dE}\to-\infty$.

This discussion suggests that the derivative procedure remains valid even when the multiple internal reflections within the sample are taken into consideration. And where

$E = E_g$ can be located by the obvious spike in a $\left(\frac{dT}{dE}\right)$ versus E plot.

References

1. Pankove, J. I. *Optical Processes in Semiconductors*. (Courier Dover Publications, 2012).

2. Stern, F. Dispersion of the Index of Refraction Near the Absorption Edge of Semiconductors. *Phys Rev Phys. Rev.* **133,** A1653–A1664 (1964).

3. Ridley, B. K. *Quantum Processes in Semiconductors*. (Oxford University Press, 2013).